

Copyright
by
Chieh Chen
2015

The Dissertation Committee for Chieh Chen
certifies that this is the approved version of the following dissertation:

Implicit Boundary Integral Methods

Committee:

Yen-Hsi Tsai, Supervisor

Todd Arbogast

George Biros

Björn Engquist

Kui Ren

Implicit Boundary Integral Methods

by

Chieh Chen, B.S., B.S., M.A.

DISSERTATION

Presented to the Faculty of the Graduate School of
The University of Texas at Austin
in Partial Fulfillment
of the Requirements
for the Degree of

DOCTOR OF PHILOSOPHY

THE UNIVERSITY OF TEXAS AT AUSTIN

December 2015

To my loving parents, Melissa and Mike.

Acknowledgments

First, I would like to thank my advisor, Richard Tsai. His deep knowledge across many fields and generosity in conveying the mathematical intuition behind have been a great resource to me. This thesis would not have been possible without his continuous support, guidance, and patience for the past three years. And most of all, his passion for computational mathematics has been contagious to move me forward. Words would fail me to express my gratitude to have him as my advisor, and to have such intriguing research topics in my dissertation.

I am truly indebted to Todd Arbogast, George Biros, Björn Engquist, and Kui Ren for serving as members of my dissertation committee, all of whom have kindly offered their time and given me great advice during my studies. My foundation in functional analysis and numerical analysis was built Prof. Arbogast's and Prof. Engquist's class. My understanding of inverse problems began in the topic course with Prof. Ren. Many thanks to Prof. Biros, for his time to communicate his expertise on Fast Multipole Methods. Special thanks to my collaborator, Catherine Kublik, for her suggestions and warm encouragement. Our fruitful discussions have helped me through plenty of computational hurdles in this thesis. I would also like to thank Prof. Žitković and Prof. Sîrbu for providing training during my early stages of graduate

school. Additionally, I gratefully acknowledge the generous support from UT Austin Mathematics Department, the National Science Foundation (DMS-1318975 and DMS-0914840), the ARO Grant (W911NF-12-1-0519), and the computational resources at Texas Advanced Computing Center (TACC).

My heart goes to my friends and colleagues, Will Carlson, Su Chen, Kai-yang Chiang, Nima Dabidian, Tian Ding, John Farley, Giovanni Franklin, Christina Frederick, Vivek George, Rene Hernandez, Yen-chun Lin, Yi-der Lin, Juan Martinez, Arthur Okura, Jamie Pool, Rodolfo Santana, Tony Sun, Sabrina Tsai, Yu-hao Tsai, Sarah Vallélian, Yi-hung Wei, Pierre Weil, and Yu-chen Yen. We have shared joyful memories and our friendship will go beyond our good time in Austin. I am extremely grateful for your support.

In the end, I would like to express my deepest thanks to my parents, Hsiu-yueh (Melissa) Wang and Yi-chen (Mike) Chen, and my sister Jung (Tina) Chen. My family have been my greatest support during this journey. Nothing and yet everything needs to be said. This thesis is dedicated to them.

Implicit Boundary Integral Methods

Publication No. _____

Chieh Chen, Ph.D.

The University of Texas at Austin, 2015

Supervisor: Yen-Hsi Tsai

Boundary integral methods (BIMs) solve constant coefficient, linear partial differential equations (PDEs) which have been formulated as integral equations. Implicit BIMs (IBIMs) transform these boundary integrals in a level set framework, where the boundaries are described implicitly as the zero level set of a Lipschitz function. The advantage of IBIMs is that they can work on a fixed Cartesian grid without having to parametrize the boundaries. This dissertation extends the IBIM model and develops algorithms for problems in two application areas.

The first part of this dissertation considers nonlinear interface dynamics driven by bulk diffusion, which involves solving Dirichlet Laplace Problems for multiply connected regions and propagating the interface according to the solutions of the PDE at each time instant. We develop an algorithm that inherits the advantages of both level set methods (LSMs) and BIMs to simulate the nonlocal front propagation problem with possible topological changes. Simu-

lation results in both 2D and 3D are provided to demonstrate the effectiveness of the algorithm.

The second part considers wave scattering problems in unbounded domains. To obtain solutions at eigenfrequencies, boundary integral formulations use a combination of double and single layer potentials to cover the null space of the single layer integral operator. However, the double layer potential leads to a hypersingular integral in Neumann problems. Traditional schemes involve an interpretation of the integral as its Hadamard's Finite Part or a complicated process of element kernel regularization. In this thesis, we introduce an extrapolatory implicit boundary integral method (EIBIM) that evaluates the natural definition of the BIM. It is able to solve the Helmholtz problems at eigenfrequencies and requires no extra complication in different dimensions. We illustrate numerical results in both 2D and 3D for various boundary shapes, which are implicitly described by level set functions.

Contents

Contents	ix
List of Tables	xiii
List of Figures	xvii
Nomenclature	xxi
Chapter 1 Introduction	1
Chapter 2 Overview of Boundary Integral Methods	7
2.1 Simply Connected Region	9
2.1.1 Interior Dirichlet Problem	9
2.1.2 Neumann Problem	14
2.2 Formulations on a Multiply-Connected Region	17
2.3 Helmholtz Problem	21
2.4 Numerical Methods	22
2.4.1 Discretization of Operator	22
2.4.2 Other Relevant Methods	24
Chapter 3 Level Set Methods	26
3.1 Introduction	26

3.2	Distance Re-initialization and Value Extension	28
3.2.1	Distance Re-initialization	28
3.2.2	Standard Redistancing	30
3.2.3	Value Extension	31
3.3	Implicit Boundary Integral Method (IBIM)	32
3.3.1	Integrand Embedding	33
3.3.2	Averaging Over Different Parametrizations	34
3.3.3	Kernel Regularization	36
3.3.4	Discretization on Cartesian Grids	38
3.4	IBIM on Adaptive Grids	42
3.4.1	Interior Laplace Problem	43
3.4.2	Exterior Helmholtz Problem	44
	Chapter 4 IBIM for Mullins-Sekerka Dynamics	46
4.1	Physical Background	46
4.2	Some Analytic Properties	49
4.3	Algorithm Details	51
4.3.1	Standard Level Set Redistancing	51
4.3.2	Connected Component Labeling	52
4.3.3	IBIM for the General Dirichlet Laplace Problem	56
4.3.3.1	Interior Component in 2D	57
4.3.3.2	Exterior Component in 2D	60
4.3.3.3	Components in 3D	62
4.3.4	Velocity Extension	65
4.3.5	Interface Propagation	66
4.4	Numerical Results in 2D	67
4.4.1	Equilibrium State	67

4.4.2	Irregular Shapes and Curve Coarsening	68
4.4.3	Non-conservation of Convexity	68
4.4.4	Shape Merging	70
4.5	Numerical Results in 3D	72
4.5.1	Solidification and Liquidation in Various Environments	72
4.5.2	Isotropic and Anisotropic Crystallization	72
Chapter 5 Extrapolatory Implicit Boundary Integral Method		74
5.1	Helmholtz Problem	74
5.2	Extrapolatory Implicit Boundary Integral Method	78
5.3	Application on Helmholtz Neumann Problem	81
5.4	Numerical Results in Two Dimensions	83
5.4.1	Unit Circle	86
5.4.1.1	Constant Tube Width	86
5.4.1.2	Tube Width $\mathcal{O}(\sqrt{H})$	86
5.4.1.3	Tube Width $\mathcal{O}(H)$	90
5.4.2	Kite Shape (Non-Convex)	92
5.4.3	Illustration of Scattering in Two Dimensions	95
5.5	Numerical Results in Three Dimensions	96
5.5.1	Unit Sphere	96
5.5.1.1	Constant Tube Width	96
5.5.1.2	Tube Width $\mathcal{O}(\sqrt{H})$	99
5.5.2	Bean Shape (Non-Convex)	100
5.5.3	Illustration of Wave Scattering in Three Dimensions	101
Chapter 6 Conclusion		104

Appendix A Regularization for Helmholtz Kernels	106
A.1 Regularization of $\frac{\partial\Phi}{\partial n_y}$ in Two Dimensions	106
A.2 Regularization of $\frac{\partial\Phi}{\partial n_y}$ in Three Dimensions	110
Appendix B Adaptive Redistancing and Integral Quadrature	114
B.1 Adaptive Redistancing	114
B.2 Integration on Adaptive Grid	118
Appendix C Numerical Results of CCL with IBIM on Dirichlet Laplace Problems	120
C.1 Two Dimensions	120
C.1.1 Multi-Hole Region	121
C.1.2 Multi-Piece Concentric Circles	121
C.1.3 Multi-Layered Annulus	121
C.2 Three Dimensions	125
Appendix D Optimal Linear Combination of Double and Single Layer Potential for Neumann Helmholtz Problem	128
References	130

List of Tables

- 3.1 Solution error of [Interior Laplace](#) problem on a circle using IBIM on an adaptive grid. The tubular neighborhood is taken to be $\varepsilon = |\nabla d_{\Gamma}|_1 * 2H$, where H is the cell width of the maximum resolution. 44
- 3.2 Solution error of [Interior Laplace](#) problem on a sphere using IBIM on adaptive grid. The tubular neighborhood is taken to be $\varepsilon = |\nabla d|_1 * 2H$, where H is the cell width of the maximum resolution. 44
- 3.3 Solution error for [exterior Helmholtz](#) problem with wave number $k = 10$ on a circle using IBIM on adaptive grid. The tubular neighborhood is taken to be $\varepsilon = |\nabla d|_1 * 2H$, where H is the cell width of the maximum resolution. 45
- 3.4 Solution error for [exterior Helmholtz](#) problem with wave number $k = 1$ on a sphere using IBIM on adaptive grid. The tubular neighborhood is taken to be $\varepsilon = |\nabla d|_1 * 2H$, where H is the cell width of the maximum resolution. 45
- 4.1 The convergence of merging time and area jump. 70
- 5.1 Condition number of the operators to be inverted in IBIM (5.8) and EIBIM (5.14). $k = 1$ is not an eigenvalue. $k = 2.4048\dots$ is the first eigenvalue of the unit disk. The tube width is a constant. 86

5.2	Solution and relative error to the Neumann Helmholtz Problem using IBIM (5.8) and EIBIM (5.14). Wave number $k = 1$ is not an eigenvalue. u_e denotes the exact solution. The tubular width for EIBIM is $\delta_0 = 0.005$, $\varepsilon_0 = 0.15$. The tubular width for IBIM method is $\varepsilon = \frac{\varepsilon_0 - \delta_0}{2}$	87
5.3	Solution and relative error using IBIM (5.8) and EIBIM (5.14). Wave number $k = 2.4048255577\dots$ is an eigenvalue. The tubular width for EIBIM is $\delta_0 = 0.005$, $\varepsilon_0 = 0.15$. The tubular width for IBIM is $\varepsilon = \frac{\varepsilon_0 - \delta_0}{2}$	87
5.4	Condition number of the operators to be inverted in IBIM (5.8) and EIBIM (5.14). $k = 1$ is not an eigenvalue. $k = 2.4048\dots$ is the first eigenvalue of the unit disk. The tube width is $\mathcal{O}(\sqrt{H})$	88
5.5	Solution and relative error to the Neumann Helmholtz Problem using IBIM (5.8) and EIBIM (5.14). Wave number $k = 1$ is not an eigenvalue. u_e denotes the exact solution. The tubular width for EIBIM is $\delta_0 = 0.5H$, $\varepsilon_0 = \sqrt{H}$. The tubular width for IBIM is $\varepsilon = \frac{\varepsilon_0 - \delta_0}{2}$	88
5.6	Solution and relative error to the Neumann Helmholtz Problem using IBIM (5.8) and EIBIM (5.14). Wave number $k = 2.4048255577\dots$ is an eigenvalue. The tubular width for EIBIM is $\delta_0 = 0.5H$, $\varepsilon_0 = \sqrt{H}$. The tubular width for IBIM is $\varepsilon = \frac{\varepsilon_0 - \delta_0}{2}$	89
5.7	The condition number of the operators to be inverted in IBIM (5.8) and EIBIM (5.14). $k = 1$ is not an eigenvalue. $k = 2.4048\dots$ is the first eigenvalue of the unit disk. The tube width is $\mathcal{O}(H)$	90
5.8	The solution and relative error using IBIM (5.8) and EIBIM (5.14). Wave number $k = 1$ is not an eigenvalue. u_e denotes the exact solution. The tubular width for EIBIM is $\delta_0 = 0.5H$, $\varepsilon_0 = 6.5H$. The tubular width for IBIM is $\varepsilon = \frac{\varepsilon_0 - \delta_0}{2}$	91

5.9	The solution and relative error using IBIM (5.8) and EIBIM (5.15). Wave number $k = 2.4048255577\dots$ is an eigenvalue. The tubular width for EIBIM is $\delta_0 = 0.5H$, $\varepsilon_0 = 6.5H$. The tubular width for IBIM is $\varepsilon = \frac{\varepsilon_0 - \delta_0}{2}$	91
5.10	Far-field solution error on 2D kite shape described in (5.18). Wave number $k = 1$	93
5.11	Far-field solution error on 2D kite shape described in (5.18). Wave number $k = 3$.	93
5.12	Far-field solution error on 2D kite shape described in (5.18). Wave number $k = 5$.	94
5.13	Number of points in the computation tubular neighborhood.	96
5.14	The solution and relative error using IBIM with only one potential (5.8) and the EIBIM with both potentials (5.14). Wave number $k = 1$ is not an eigenvalue. u_e denotes the exact solution. The tubular width for EIBIM is $\delta_0 = 0.005$, $\varepsilon_0 = 0.3$. The tubular width for IBIM is $\varepsilon = \sqrt{\varepsilon_0^2 - \delta_0^2}$	97
5.15	The solution and relative error using IBIM with only one potential (5.8) and EIBIM with both potentials (5.14). Wave number $k = \pi$ is an eigenvalue. The tubular width for EIBIM is $\delta_0 = 0.005$, $\varepsilon_0 = 0.3$. The tubular width for IBIM is $\varepsilon = \sqrt{\varepsilon_0^2 - \delta_0^2}$	98
5.16	The solution and relative error using IBIM (5.8) and EIBIM (5.14). Wave number $k = 1$ is not an eigenvalue. u_e denotes the exact solution. The tubular width for EIBIM is $\delta_0 = 0.1H$, $\varepsilon_0 = \sqrt{H}$. The tubular width for IBIM is $\varepsilon = \sqrt{\varepsilon_0^2 - \delta_0^2}$	99
5.17	The solution and relative error using IBIM (5.8) and EIBIM (5.14). Wave number $k = \pi$ is an eigenvalue. The tubular width for EIBIM is $\delta_0 = 0.1H$, $\varepsilon_0 = \sqrt{H}$. The tubular width for IBIM is $\varepsilon = \sqrt{\varepsilon_0^2 - \delta_0^2}$	100
5.18	Consecutive difference of the scatter wave solution and comparison with IBIM on bean shape. $k = 1$, $\varepsilon_0 = \sqrt{H}$. Evaluated at $(2, 2, 2)$	101

C.1	The convergence of solution to Laplace equation with interface illustrated in Figure C.1 on page 121. The boundary condition is taken to be the constant 1. The error is taken to be the absolute error. The convergence order is approximately approaching one.	122
C.2	The convergence of solution to Laplace equation with interface illustrated in Figure C.2 on page 123. The boundary condition is taken to be the constant 1. The convergence order is approximately approaching one.	122
C.3	The convergence of solution to Laplace equation with interface illustrated in Figure C.3 on page 124. The boundary condition is taken to be the signed curvature of the curve, with the inmost curve having the clockwise (negative) orientation. The absolute error is larger at point 2 and point 3 because the points are closer to the boundary. The convergence order is approximately approaching one.	125
C.4	The solution error for two multi-layered balls. The testing boundary condition is the constant 1. The first multi-layered ball is centered at $(-0.5, -0.5, -0.5)$ with radii 0.23, 0.47, 0.72, 0.95. The second multi-layered ball is centered at $(0.8, 0.8, 0.8)$ with radii 0.31, 0.61. The convergence order seems to approach 1.	126
C.5	The solution error for one multi-layered ball. The boundary condition is assigned the signed curvature. The multi-layered ball is centered at $(0.1, 0.2, -0.1)$ with radii 0.23, 0.47, 0.72, 0.95.	127

List of Figures

3.1	Parametrization from parallel interface.	33
3.2	Averaging with a regularized Dirac delta function over level sets.	36
3.3	Kernel singularity for close points.	37
3.4	Compute an analytic regularization quadrature by approximating the true interface S with a second order contacting curve.	38
3.5	Circle on adaptive grid with curvature splitting criterion.	43
4.1	The evolution of perimeter and mass (area) of an ellipse in Mullins-Sekerka model.	50
4.2	Procedure diagram for Mullins-Sekerka simulation.	51
4.3	The labeling of interior and exterior of two simply-connected components.	54
4.4	The labeling of interior and exterior of an annulus.	54
4.5	The labeling of interior and exterior of a multi-layer annulus.	54
4.6	Interface evolution for circle and ellipse. This is an illustration of the equilibrium state.	68
4.7	Simulation of an interface with sharp corners.	68
4.8	The coarsening dynamics of multiple components with irregular shapes.	69
4.9	Dynamics of long tube.	69
4.10	Ellipse merging in 2D Mullins-Sekerka flow simulation.	71

4.11	On the left, both spheres grow on low temperature. In the middle, both shrinks on high temperature. On the right, the temperature is deliberately set at phase transition point. We see that the larger sphere grows at the expense of the smaller sphere, just as we would observe in the $2D$ case.	72
4.12	Instability of dendritic growth while maintaining crystal symmetry.	73
4.13	Comparison of crystallization with anisotropy.	73
5.1	Weight function W_{EIBIM} (black) and W (blue). Both functions are in the weighting function space $\mathbb{W}_{0.1,1}^1$ as defined in (5.9). Additionally, W_{EIBIM} has two vanishing derivatives at δ_0 , whereas W is only continuous. The first two plots show the shape of the two weighting functions and their first derivatives. The third plot is the extrapolation error for the function $f(\eta) = \frac{1}{\sqrt{\eta+0.05}}$ on the interval $[0.1dx, \sqrt{dx}]$	84
5.2	Error results for integration over hypersingular kernel with W (blue) and W_{EIBIM} (black). Both are in the weighting functions space $\mathbb{W}_{\delta_0, \varepsilon_0}^1$, as defined in (5.9). Additionally, we have $W'_{EIBIM}(\delta_0) = W''_{EIBIM}(\delta_0) = 0$ while W is only continuous at δ_0	85
5.3	Solution error plots for non-eigenvalue $k = 1$ (left) and eigenvalue $k = 2.404825558\dots$ (right) using IBIM and EIBIM. The integration is performed on a constant width tubular region.	87
5.4	Solution error plots for non-eigenvalue $k = 1$ (left) and eigenvalue $k = 2.404825558\dots$ (right) using IBIM and EIBIM. The integration is performed on a tubular region with width of $\mathcal{O}(\sqrt{H})$	89
5.5	Solution error plots for non-eigenvalue $k = 1$ (left) and eigenvalue $k = 2.404825558\dots$ (right) using IBIM and EIBIM. The integration is performed on a tubular region of width $\mathcal{O}(H)$	92
5.6	Kite shape described by (5.18).	94

5.7	Scattering by a flower shape with Dirichlet boundary conditions. $k = 1, 5$. . .	95
5.8	Scattering by a moon shape with Dirichlet boundary conditions. $k = 1, 5$. We compare the results where the wave source is near and far.	95
5.9	Relative Error for Helmholtz Neumann Problem in 3D on constant tubular width.	97
5.10	Relative Error for Helmholtz Neumann Problem in 3D. Tubular width is $\mathcal{O}(\sqrt{H})$. 99	
5.11	The bean shape. The interface is the zero set of $0.9(1.6x + (\frac{y}{1.6})^2)^2 + (\frac{y}{1.5})^2 + (\frac{z}{1.5})^2 = 1$	101
5.12	3D scattering by a torus with Dirichlet boundary conditions using $k = 3, 12$. .	102
5.13	3D scattering by bowl shape with Dirichlet boundary conditions using $k = 12$. The wave is in a slanted direction.	103
B.1	Tree splitting based on distance (left) and both distance and curvature (right) on a flower shape.	116
B.2	Tree splitting based on distance (left) and both distance and curvature (right) on a star shape.	117
B.3	The cell on the left has finer resolution, and hence the point in the middle has no neighbor on its right in the coarser cell.	117
B.4	The closer upper left subcell in the right cell has the finest resolution. The case in 3D is more complicated in that one point may have up to two ghost neighbors. And depending on the situation, the interpolation may be a 2D interpolation.	117
B.5	Local trapezoidal rule illustration in 2D.	119

C.1 Illustration of the regions and the test points. The interior regions are surrounded by red boundary and exterior surrounded by blue. The green dots are representative points selected by CCL so that they are furthest from boundary in exterior regions, while black dots are for interior regions. The test points are labeled and colored brown. The boundary condition is taken to be the constant 1. 121

C.2 Illustration of the regions and the test points. As in Figure C.1, the interior regions are surrounded by red boundary and exterior surrounded by blue. The green dots are representative points selected by CCL so that they are furthest from boundary in exterior regions, while black dots are for interior regions. The test points are labeled and colored brown. The boundary condition is taken to be the constant 1. 123

C.3 Illustration of a multi-layered annulus and the test points. The boundary condition is the signed curvature on the interface, as one would encounter for Mullins-Sekerka simulations. The solution is a linear combination of a constant and a logarithm of the norm depending on the region. 124

Nomenclature

Roman Symbols

Γ Boundary of Domain

Ω Domain of Interest

k wave number

Chapter 1

Introduction

This thesis develops numerical algorithms for solving constant coefficient linear partial differential equations (PDEs) in the implicit boundary integral framework [Kublik *et al.* (2013)]. We focus on two tasks: the Mullins-Sekerka flow simulation and the exterior Neumann Helmholtz problem. The Mullins-Sekerka model is a Stefan-type free boundary problem, where the boundary evolution is dynamically controlled by the solution of the Laplace equation from both sides of the hypersurface. The exterior Neumann Helmholtz problem is to construct a time harmonic wave outside a bounded region with prescribed normal derivatives as boundary conditions. In both scenarios, one seeks the solution in the unbounded exterior of a bounded domain. This leads to computational challenges and motivates boundary integral methods (BIMs). We address motivations for using *implicit* boundary integral methods (IBIMs). We explain simulation strategies and illustrate the effectiveness of these strategies with numerical results. We also introduce an extension of IBIMs to tackle hypersingular-type integrals and provide numerical results to demonstrate the effectiveness of this extension.

The motivation for studying free boundary problems with interface dynamics driven by diffusion is a wide variety of applications, including dendritic growth in crystallization and solidification [W. Kurz (1986); Flemings (2006)], phase separation and coarsening for melting alloy [Cahn & Hilliard (1959); Fornaro *et al.* (2006)], bacterial colony growth [Matsushita

& Fujikawa (1990); Golding *et al.* (1998)], flame propagation [Caffarelli & Vázquez (1995); Buckmaster & Ludford (2008)], and drying water films [Samid-Merzel *et al.* (1998)]. The application we address is the Mullins-Sekerka flow [Mullins & Sekerka (1963)]. It was proposed originally as an isotropic model for solidification and liquidation of materials in an undercooling environment. The flow is a high order, nonlinear, nonlocal model, with boundary (interface) evolution depending on the solution of the Dirichlet Laplace problem

$$\begin{cases} \Delta u(\mathbf{x}) = 0, & \mathbf{x} \in \mathbb{R}^m \setminus \Gamma_t, \\ u(\mathbf{x}) = \kappa(\mathbf{x}), & \mathbf{x} \in \Gamma_t, \end{cases}$$

where we use Γ_t to denote the \mathcal{C}^2 boundary of an open bounded region Ω_t at time t and κ to denote its (mean) curvature.

The second problem we study is the exterior Neumann Helmholtz problem:

$$\begin{cases} (\Delta + k^2)u(\mathbf{x}) = 0, & \mathbf{x} \in \mathbb{R}^m \setminus \bar{\Omega}. \\ \frac{\partial u}{\partial n}(\mathbf{x}) = g(\mathbf{x}), & \mathbf{x} \in \partial\Omega. \end{cases}$$

The Helmholtz equation governs the steady state solution of wave equations in a homogeneous medium. Its applications include cloaking in aerospace engineering [Greenleaf *et al.* (2008); Kohn *et al.* (2008)], geophysics and seismology [Burridge (1976); Shearer (2003)], and medical imaging [Kuchment & Kunyansky (2008); Ammari *et al.* (2010)]. The exterior Helmholtz problem with Neumann boundary conditions models a sound-hard acoustic wave scattering or an electromagnetic wave scattering by a perfect conductor.

Many different methods have been proposed to solve a second order linear PDE in irregular domains, including finite difference methods (FDMs) [Johansen & Colella (1998); Gibou & Fedkiw (2004); Bedrossian *et al.* (2010)], finite element methods (FEMs) [Babuska (1970); Hansbo & Hansbo (2004); Dolbow & Harari (2009)], and immerse interface methods (IIMs)

[Leveque & Li (1994); Li & Ito (2006)]. For a PDE with constant coefficients, boundary integral methods (BIMs) [Atkinson & Chandler (1990); Helsing (2009)] become a viable option. This is due to the existence of free space Green's function (fundamental solution) [Malgrange (1956); Ehrenpreis (1960); Wagner (2009)]. That is, given a constant coefficient linear operator \mathcal{L} , $\mathcal{L}u = h$, we have the fundamental solution Φ that solves the inhomogeneous equation with the Dirac δ

$$\mathcal{L}\Phi = \delta(x).$$

A solution is then provided by the property of convolution and δ :

$$\mathcal{L}(\Phi * h) = \mathcal{L}\Phi * h = \delta(x) * h(x) = h(x).$$

Green's identity can further be used to transform the integral in the domain into an integral on the boundary. In the case of a PDE with Dirichlet boundary conditions, the strategy for solving the PDE is a two step process:

1. Solve for β satisfying the following boundary integral equation:

$$\int_{\Gamma} K(\mathbf{x}, \mathbf{y}(s))\beta(\mathbf{y}(s)) ds + \lambda\beta(\mathbf{x}) = f(\mathbf{x}), \mathbf{x} \in \Gamma (= \partial\Omega). \quad (1.1)$$

2. To evaluate the solution u at any point $\mathbf{x} \in \mathbb{R}^m \setminus \Gamma$, compute the boundary integral:

$$u(\mathbf{x}) = \int_{\Gamma} \tilde{K}(\mathbf{x}, \mathbf{y}(s))\beta(\mathbf{y}(s)) ds, \mathbf{x} \in \mathbb{R}^m \setminus \Gamma.$$

In the above equations, λ is a constant, K , \tilde{K} (the kernels) are related to the fundamental solution, and $\mathbf{y}(s)$ is a parametrization of the boundary Γ .

We refer interested readers to [Kress (2012)] for an extensive study on boundary integral

methods for various problems.

In the simulation of Mullins-Sekerka flow and the solution to the exterior Helmholtz problem, there are two main advantages that make BIMs attractive:

1. The computation domain is restricted to the boundary, regardless of the boundedness of the region where the solution is desired.
2. In many cases, the solution produced automatically satisfies the boundary condition at infinity (for example, the Sommerfeld radiation condition for the exterior Helmholtz problem).

These advantages do not come for free. One numerical complication is the discretization of computation domain, which typically requires an explicit parametrization of the boundary. For simulations of a front evolution problem, re-parametrization can be difficult and expensive when there are topological changes, especially in higher dimensions. Another challenge is the integrals involve singular kernels K and \tilde{K} , where the singularities come from the fundamental solution. The singularities are particularly severe for Neumann problems, where a normal derivative is taken and a hypersingular integral is introduced to cover the null space of the singular integral operator [Burton & Miller (1971)]. In this case, the boundary integral does not converge in the traditional Riemann sense. Even though the computation of Hadamard's finite part (HFP) has been introduced [Kutt (1975)], and numerical schemes have been researched [Paget (1981); Liu & Rizzo (1992); Hackbusch & Sauter (1993); Frangi (1998); Aimi & Diligenti (2002)], the regularization method to account for the quadrature at singularities is geometrically specific and usually inconsistent in different dimensions.

We summarize the challenges this thesis deals with and the proposed strategies:

1. For interface dynamics, it is difficult for FDMs and FEMs to solve exterior problems, whereas traditional BIMs have limitations on topological changes.
 - Our strategy is to develop a BIM for level set methods (LSMs). These algorithms

will inherit advantages from both methods; i.e. the capability to solve exterior domain problems (from BIMs) without artificial boundary conditions and the ease in handling irregular, evolving domains that change topology without the need of parametrization (from LSMs).

2. For the exterior Neumann Helmholtz Problem, FDMs and FEMs have the same difficulties solving exterior problems, and conventional BIMs have complicated inconsistent regularization methods for hypersingular integrals.
 - Our strategy is to use an extrapolatory, implicit BIM that evaluates the integral in its natural definition. This method is consistent in all dimensions.

The structure of this thesis is as follows. Chapter 2 introduces the typical boundary integral formulations, their theoretical background, and available numerical schemes. We restrict our attention to the Dirichlet Laplace problem and the exterior Neumann Helmholtz problem, the principal concerns of this thesis. Chapter 3 describes LSMs, the techniques in implementing interface evolution in that context, and introduces the implicit boundary integral methods (IBIMs) [Kublik *et al.* (2013)], which transforms a typical BIM (1.1) into a level set based integral

$$\int_{\mathbb{R}^m} K_{\Gamma}(\mathbf{x}, \mathbf{y}) \bar{\beta}(\mathbf{y}) \delta_{\epsilon}(\mathbf{y}) d\mathbf{y} + \lambda \bar{\beta}(\mathbf{x}) = \bar{f}(\mathbf{x}), \mathbf{x} \in \Gamma,$$

where Γ is a \mathcal{C}^2 boundary, the bar denotes a value extension from Γ (the zero level set) into \mathbb{R}^m , and the subscript K_{Γ} denotes a weighted restriction of the kernel K to be evaluated on Γ .

In Chapter 4, we develop an IBIM for the high order nonlinear Mullins-Sekerka flow. We describe implementation techniques including a connected component labeling (CCL) algorithm [Rosenfeld & Pfaltz (1966); Samet & Tamminen (1988); Dillencourt *et al.* (1992); Di Stefano & Bulgarelli (1999)] to identify components of a complicated topology. We demonstrate the effectiveness of this method in simulating topological changes. To the best of our knowledge, no BIM has been able to do this. The IBIM works for unbounded domains.

To our best knowledge, no LSM has this capability.

In Chapter 5 we derive an extrapolatory implicit boundary integral method (EIBIM) for Helmholtz problems, in particular for the exterior Neumann Helmholtz problem, which typically requires solving an integral equation with a hypersingular kernel K . Our method takes advantage of extending the kernel from Γ (the zero level set) to \mathbb{R}^m in each variable and takes the following form:

$$\int_{\mathbb{R}^m} K_{\Gamma(d_{\Gamma}(\mathbf{y})),\Gamma}(\mathbf{x},\mathbf{y})\bar{\beta}(\mathbf{y})W(\mathbf{y})d\mathbf{y} + \lambda\bar{\beta}(\mathbf{x}) = \bar{f}(\mathbf{x}), \mathbf{x} \in \Gamma.$$

EIBIM provides a way to evaluate the natural definition of the relevant class of hypersingular integrals. The algorithm is consistent in different dimensions for various geometries with fewer complications than conventional finite part based BIMs.

We conclude and describe future directions in Chapter 6. As both IBIM and EIBIM rely on closest points to a manifold, they have the potential to generalize to applications on manifolds with boundaries. This thesis provides some of the necessary foundation for such applications.

Chapter 2

Overview of Boundary Integral Methods

In this chapter, we summarize solving PDEs with boundary integral formulations and introduce some relevant numerical methods. Although the derivations can easily be generalized to a wide class of differential equations, we focus on Dirichlet Laplace Problems (for Mullins-Sekerka Dynamics) and the exterior Neumann Helmholtz Problem (for wave scattering). We go over the formulations for the interior Dirichlet Laplace Problem on simply connected regions in Section 2.1, multiply-connected regions in Section 2.2, and the Helmholtz problems in Section 2.3. Section 2.4 will be devoted to introduce numerical methods for BIMs.

Throughout this thesis we assume $\Omega \subset \mathbb{R}^m$, $m = 2, 3$ bounded, its boundary $\Gamma = \partial\Omega$ is a (disjoint) collection of closed compact \mathcal{C}^2 hyperinterfaces, the symbols $\mathbf{n}^+ (= \mathbf{n})$, \mathbf{n}^- denote the unit normal vectors directed into exterior and interior regions, and all boundaries are parametrized with the element measure. The exterior is defined to be the unbounded domain. The main problems of interest are:

Definition 1. Interior Dirichlet Laplace Problem

Find $u \in \mathcal{C}^2(\Omega) \cap \mathcal{C}(\bar{\Omega})$ which satisfies the following equations:

$$\begin{cases} \Delta u(\mathbf{x}) = 0, & \mathbf{x} \in \Omega. \\ u(\mathbf{x}) = f(\mathbf{x}), & \mathbf{x} \in \Gamma. \end{cases} \quad (2.1)$$

Definition 2. Exterior Dirichlet Laplace Problem

Find $u \in \mathcal{C}^2(\mathbb{R}^m \setminus \bar{\Omega}) \cap \mathcal{C}(\mathbb{R}^m \setminus \Omega)$ which satisfies the following equations:

$$\begin{cases} \Delta u(\mathbf{x}) = 0, & \mathbf{x} \in \mathbb{R}^m \setminus \bar{\Omega}. \\ u(\mathbf{x}) = f(\mathbf{x}), & \mathbf{x} \in \Gamma. \\ \lim_{|\mathbf{x}| \rightarrow \infty} |u(\mathbf{x})| < \infty, & m = 2. \\ \lim_{|\mathbf{x}| \rightarrow \infty} u(\mathbf{x}) = u_\infty, & m = 3. \end{cases} \quad (2.2)$$

The exterior Dirichlet problem has very different behavior in 2D and 3D. In 2D, we only require the far-field behavior to be bounded and the solution will be unique. In 3D, boundedness is not enough and prescribing a far-field value is necessary to guarantee the uniqueness of the solution.

We take the following sign convention for the fundamental solutions (free space Green's function) in \mathbb{R}^m :

$$\Delta_{\mathbf{y}} \Phi(\mathbf{x}, \mathbf{y}) = \delta(|\mathbf{x} - \mathbf{y}|).$$

The fundamental solutions relative to this convention in \mathbb{R}^2 and \mathbb{R}^3 are

$$\Phi(\mathbf{x}, \mathbf{y}) = \begin{cases} \frac{1}{2\pi} \ln(|\mathbf{x} - \mathbf{y}|), & \mathbf{x}, \mathbf{y} \in \mathbb{R}^2. \\ \frac{1}{4\pi} \frac{-1}{|\mathbf{x} - \mathbf{y}|}, & \mathbf{x}, \mathbf{y} \in \mathbb{R}^3. \end{cases}$$

With the fundamental solutions, we define the operators $\mathcal{S}, \mathcal{D}, \mathcal{D}^*, \mathcal{T} : C^\infty(\Gamma) \rightarrow C(\mathbb{R}^2)$ as follows:

$$\begin{aligned}
(\mathcal{S}\alpha)(x) &:= \int_{\Gamma} \Phi(x, y) \alpha(y) dy(s). \\
(\mathcal{D}\alpha)(x) &:= \int_{\Gamma} \frac{\partial \Phi}{\partial n_y}(x, y) \alpha(y) dy(s). \\
(\mathcal{D}^*\alpha)(x) &:= \int_{\Gamma} \frac{\partial \Phi}{\partial n_x}(x, y) \alpha(y) dy(s). \\
(\mathcal{T}\alpha)(x) &:= \int_{\Gamma} \frac{\partial^2 \Phi}{\partial n_x \partial n_y}(x, y) \alpha(y) dy(s).
\end{aligned} \tag{2.3}$$

2.1 Simply Connected Region

2.1.1 Interior Dirichlet Problem

From the harmonicity of u and the property of Φ we have

$$\chi_{\Omega}(\mathbf{x})u(\mathbf{x}) = \int_{\Omega} u(\mathbf{y})\Delta_{\mathbf{y}}\Phi(\mathbf{x}, \mathbf{y}) - \Delta_{\mathbf{y}}u(\mathbf{y})\Phi(\mathbf{x}, \mathbf{y}) dy,$$

where χ_{Ω} is the indicator function of Ω . Using Green's second identity,

$$\begin{aligned}
\chi_{\Omega}(\mathbf{x})u(\mathbf{x}) &= \int_{\Omega} u(\mathbf{y})\Delta_{\mathbf{y}}\Phi(\mathbf{x}, \mathbf{y}) - \Delta_{\mathbf{y}}u(\mathbf{y})\Phi(\mathbf{x}, \mathbf{y}) dy \\
&= \left(\int_{\Gamma} \left(u(\mathbf{y}) \frac{\partial \Phi(\mathbf{x}, \mathbf{y})}{\partial n_y^+} - \frac{\partial u(\mathbf{y})}{\partial n_y^+} \Phi(\mathbf{x}, \mathbf{y}) \right) dS(\mathbf{y}) \right) \\
&= \int_{\Gamma} \left(-u(\mathbf{y}) \frac{\partial \Phi(\mathbf{x}, \mathbf{y})}{\partial n_y^-} + \frac{\partial u(\mathbf{y})}{\partial n_y^-} \Phi(\mathbf{x}, \mathbf{y}) \right) dS(\mathbf{y}).
\end{aligned} \tag{2.4}$$

In order to obtain a formulation using only the values of u on the boundary (Dirichlet conditions), we seek a function $v \in \mathcal{C}^2(\mathbb{R}^m \setminus \bar{\Omega}) \cap \mathcal{C}(\mathbb{R}^m \setminus \Omega)$, satisfying

$$\begin{cases} \Delta v(\mathbf{x}) = 0, & \mathbf{x} \in \mathbb{R}^m \setminus \bar{\Omega}. \\ \frac{\partial v}{\partial n^+}(\mathbf{x}) = \frac{\partial u}{\partial n^+}(\mathbf{x}), & \mathbf{x} \in \Gamma. \\ \lim_{|\mathbf{x}| \rightarrow \infty} v(\mathbf{x}) = 0. \end{cases} \quad (2.5)$$

The solution to this exterior Neumann problem is unique. Pick R sufficiently large such that $\Omega \subset B_R(\mathbf{x})$, where $B_R(\mathbf{x})$ is a ball of radius R centered at \mathbf{x} . Similar derivation gives

$$\begin{aligned} \chi_{B_R(\mathbf{x}) \setminus \bar{\Omega}}(\mathbf{x})v(\mathbf{x}) &= \int_{\mathbb{R}^m \setminus \bar{\Omega}} v(\mathbf{y}) \Delta_{\mathbf{y}} \Phi(\mathbf{x}, \mathbf{y}) - \Delta_{\mathbf{y}} v(\mathbf{y}) \Phi(\mathbf{x}, \mathbf{y}) d\mathbf{y} \\ &= \left(\int_{\Gamma} (v(\mathbf{y}) \frac{\partial \Phi(\mathbf{x}, \mathbf{y})}{\partial n_{\mathbf{y}}^-} - \frac{\partial v(\mathbf{y})}{\partial n_{\mathbf{y}}^-} \Phi(\mathbf{x}, \mathbf{y})) dS(\mathbf{y}) \right) \\ &\quad + \int_{\partial B_R(\mathbf{x})} (v(\mathbf{y}) \frac{\partial \Phi(\mathbf{x}, \mathbf{y})}{\partial n_{\mathbf{y}}^+} - \frac{\partial v(\mathbf{y})}{\partial n_{\mathbf{y}}^+} \Phi(\mathbf{x}, \mathbf{y})) dS(\mathbf{y}). \end{aligned} \quad (2.6)$$

We consider the behavior of the last term on the right hand side when $R \rightarrow \infty$. In three dimensions, we have the following estimate:

$$\begin{aligned} & \left| \int_{\partial B_R(\mathbf{x})} (v(\mathbf{y}) \frac{\partial \Phi(\mathbf{x}, \mathbf{y})}{\partial n_{\mathbf{y}}^+} - \frac{\partial v(\mathbf{y})}{\partial n_{\mathbf{y}}^+} \Phi(\mathbf{x}, \mathbf{y})) dS(\mathbf{y}) \right| \\ & < \frac{1}{4\pi R^2} \int_{\partial B_R(\mathbf{x})} \max |v(\mathbf{y})| dS(\mathbf{y}) + \frac{1}{4\pi R} \int_{\Gamma} \left| \frac{\partial v}{\partial n^+} \right| dS(\mathbf{y}) \\ & < \frac{4\pi R^2 \varepsilon}{4\pi R^2} + \frac{C}{4\pi R} \rightarrow 0 \text{ as } R \rightarrow \infty, \end{aligned}$$

where we use the fact that $\int_{\Gamma} \frac{\partial v}{\partial n} + \int_{B_R(\mathbf{x})} \frac{\partial v}{\partial n} = 0$ because v is harmonic in $\Omega^+ \cap B_R(\mathbf{x})$ and that $|\Gamma|$ is finite. In two dimensions, we have a similar estimate:

$$\begin{aligned} & \left| \int_{\partial B_R(\mathbf{x})} (v(\mathbf{y}) \frac{\partial \Phi(\mathbf{x}, \mathbf{y})}{\partial n_{\mathbf{y}}^+} - \frac{\partial v(\mathbf{y})}{\partial n_{\mathbf{y}}^+} \Phi(\mathbf{x}, \mathbf{y})) dS(\mathbf{y}) \right| \\ & < \frac{1}{2\pi R} \int_{\partial B_R(\mathbf{x})} |\max v(\mathbf{y})| dS(\mathbf{y}) + \frac{1}{2\pi} \ln R \int_{\Gamma} \left| \frac{\partial v}{\partial n^+} \right| dS(\mathbf{y}). \end{aligned}$$

The first term goes to zero as in 3D. For the second term, although $\ln R \rightarrow \infty$ as $R \rightarrow \infty$, we have the following lemma that is only valid in 2D:

Lemma 1. *Let Ω be a bounded region in \mathbb{R}^2 ,*

$$\begin{cases} \Delta v(\mathbf{x}) & = 0, \mathbf{x} \in \mathbb{R}^2 \setminus \bar{\Omega}, \\ \sup_{\mathbf{x} \in \mathbb{R}^2 \setminus \Omega} |v(\mathbf{x})| & < \infty, \end{cases}$$

then we have the compatibility condition

$$\int_{\partial\Omega} \frac{\partial v}{\partial n} = 0.$$

Proof. Without loss of generality, $0 \in \Omega$. Pick r, R sufficiently large such that $\Omega^- \subset B_r(0) \subset B_R(0)$. Since $v, \Phi(0, \mathbf{y})$ are both harmonic in the annulus, we have from Green's identity of v and $\Phi(0, \mathbf{y})$ on the annulus $r < |\mathbf{y}| < R$, we have

$$\frac{1}{r} \int_{\partial B_r(0)} v ds - \ln r \int_{\partial B_r(0)} \frac{\partial v}{\partial n^-} ds = \frac{1}{R} \int_{\partial B_R(0)} v ds - \ln R \int_{\partial B_R(0)} \frac{\partial v}{\partial n^+} ds.$$

But v is harmonic in $(\mathbb{R}^m \setminus \bar{\Omega}) \cap B_R(0)$, or $(\mathbb{R}^m \setminus \bar{\Omega}) \cap B_r(0)$ respectively, we can then change the above to

$$\frac{1}{r} \int_{\partial B_r(0)} v ds - \ln r \int_{\Gamma} \frac{\partial v}{\partial n^+} ds = \frac{1}{R} \int_{\partial B_R(0)} v ds - \ln R \int_{\Gamma} \frac{\partial v}{\partial n^-} ds. \quad (2.7)$$

Now the left hand side and the first term on the right hand side is bounded, since $\ln R \rightarrow \infty$, we must have $\int_{\Gamma} \frac{\partial v}{\partial n} ds = 0$. □

Remark 1. In 3D, the fundamental solution $\frac{1}{4\pi R} \rightarrow 0$ as $R \rightarrow \infty$ hence the above argument does not work. The integral $\int_{\Gamma} \frac{\partial v}{\partial n} dS(\mathbf{y})$ is not necessarily 0.

Also notice that the second term is then zero in (2.7) as well, since the lemma is valid for

any far-field condition (though for the double layer formulation with respect to the interior Dirichlet problem $v \rightarrow 0$ as $|\mathbf{x}| \rightarrow \infty$), we have the mean value property for the far field that is only true for 2D:

$$v_\infty = \frac{1}{2\pi r} \int_{\partial B_r(0)} v ds \text{ for } \Omega^- \subset B_r(0).$$

From the above lemma, we have that in both 2D and 3D, the last integral in (2.6) will go to zero as $R \rightarrow \infty$. Summing up (2.4) and (2.6), we have the boundary integral formulation for 2D and 3D:

$$\int_{\Gamma} (u(\mathbf{y}) - v(\mathbf{y})) \frac{\partial \Phi(\mathbf{x}, \mathbf{y})}{\partial n_{\mathbf{y}}^+} dS(\mathbf{y}) = \begin{cases} u(\mathbf{x}) & , x \in \Omega. \\ v(\mathbf{x}) & , x \in \mathbb{R}^m \setminus \bar{\Omega}. \end{cases} \quad (2.8)$$

This integral is usually termed **double layer potential** in the potential theory. The normal derivative of the fundamental solution is referred to as the **kernel**, whereas the jump between the interior solution and its adjoint solution across the boundary $u - v$ is called the **double layer density function**. The integral is not yet defined for $x \in \Gamma$ because of the singularity in Φ . We need the next lemma for $x \in \Gamma$:

Lemma 2. *Let $\beta \in \mathcal{C}(\mathbb{R}^m) \cap \mathcal{C}^2(\mathbb{R}^m \setminus \Gamma)$. For $\mathbf{x} \in \Gamma$, we have*

$$\lim_{h \rightarrow 0} \int_{\Gamma} \beta(\mathbf{y}) \frac{\partial \Phi(\mathbf{x} \pm hn_{\mathbf{x}}^+, \mathbf{y})}{\partial n_{\mathbf{y}}^+} dS(\mathbf{y}) = \int_{\Gamma} \beta(\mathbf{x}) \frac{\partial \Phi(\mathbf{x}, \mathbf{y})}{\partial n_{\mathbf{y}}^+} dS(\mathbf{y}) \mp \frac{1}{2} \beta(\mathbf{x}). \quad (2.9)$$

Use the Dirichlet data u on the boundary, we have the double layer boundary integral formulation for interior Dirichlet problems.

Double Layer Formulation for the Interior Dirichlet (Laplace) Problem:

1. Solve the density β ($= u - v$) from the integral equation

$$\int_{\Gamma} \frac{\partial \Phi(\mathbf{x}, \mathbf{y})}{\partial n_{\mathbf{y}}^+} \beta(\mathbf{y}) dS(\mathbf{y}) + \frac{1}{2} \beta(\mathbf{x}) = f(\mathbf{x}), \quad x \in \Gamma. \quad (2.10)$$

2. The solution u at any $\mathbf{x} \in \Omega$ is expressed in integral form:

$$u(\mathbf{x}) = \int_{\Gamma} \frac{\partial \Phi(\mathbf{x}, \mathbf{y})}{\partial n_{\mathbf{y}}^+} \beta(\mathbf{y}) dS(\mathbf{y}), \quad x \in \Omega. \quad (2.11)$$

The double layer potential is not the only boundary integral formulation we can obtain from the Green's identities. Instead of matching the normal derivative of the interior solution as in (2.5), we can choose to match the solution itself on the boundary to obtain a different adjoint exterior problem:

$$\begin{cases} \Delta v(\mathbf{x}) = 0, & \mathbf{x} \in \mathbb{R}^m \setminus \bar{\Omega}. \\ v(\mathbf{x}) = u(\mathbf{x}), & \mathbf{x} \in \Gamma. \\ \lim_{|\mathbf{x}| \rightarrow \infty} v(\mathbf{x}) = 0. \end{cases} \quad (2.12)$$

We follow the same procedures as in the derivation of double layer potential and get

$$\int_{\Gamma} \left(\frac{\partial v}{\partial n_{\mathbf{y}}^+}(\mathbf{y}) - \frac{\partial u}{\partial n_{\mathbf{y}}^+}(\mathbf{y}) \right) \Phi(\mathbf{x}, \mathbf{y}) dS(\mathbf{y}) = \begin{cases} u(\mathbf{x}) & , x \in \Omega. \\ v(\mathbf{x}) & , x \in \mathbb{R}^m \setminus \bar{\Omega}. \end{cases} \quad (2.13)$$

The integral and the jump $\beta(\mathbf{y}) = \frac{\partial v}{\partial n_{\mathbf{y}}^+}(\mathbf{y}) - \frac{\partial u}{\partial n_{\mathbf{y}}^+}(\mathbf{y})$ are called the **single layer potential** and the **single layer potential density**. In this case, kernel singularity is weak and the integral is well defined in the Riemann sense. We summarize the single layer formulation for the interior Dirichlet Laplace problem.

Single Layer Formulation for the Interior Dirichlet (Laplace) Problem:

1. Solve the density $\beta (= \frac{\partial v}{\partial n_{\mathbf{y}}^+} - \frac{\partial u}{\partial n_{\mathbf{y}}^+})$ from

$$\int_{\Gamma} \Phi(\mathbf{x}, \mathbf{y}) \beta(\mathbf{y}) dS(\mathbf{y}) = f(\mathbf{x}), \quad x \in \Gamma. \quad (2.14)$$

2. The solution u at $\mathbf{x} \in \Omega$ can be obtained using the integral

$$u(\mathbf{x}) = \int_{\Gamma} \Phi(\mathbf{x}, \mathbf{y}) \beta(\mathbf{y}) dS(\mathbf{y}), \quad x \in \Omega. \quad (2.15)$$

Remark 2. Although the single layer formulation (2.14) for Dirichlet problems has only a weak singularity in the boundary integral, it is hard to invert this integral operator numerically because the condition number of the discretized operator is large. The double layer formulation controls the condition number with its dominant diagonal $\frac{1}{2}$. Therefore, it is more popular to use a more singular double layer formulation (2.10) to solve Dirichlet problems. Creating a good numerical quadrature near this singularity is the main theme in this research direction.

2.1.2 Neumann Problem

For Neumann problems, we are given the normal derivatives on the boundary. For the scope of this thesis, we focus on the exterior Neumann problem, which has a unique solution once the prescribed Neumann data satisfy the compatibility condition $\int_{\Gamma} \frac{\partial u}{\partial n} = 0$. Intuitively, we

take the normal derivative of the previous formulations (for Dirichlet problems) to obtain the formulations for Neumann problems. We need the following lemma:

Lemma 3. *Let $\beta \in \mathcal{C}(\mathbb{R}^m) \cap \mathcal{C}^2(\mathbb{R}^m \setminus \Gamma)$. For $\mathbf{x} \in \Gamma$, we have*

$$\lim_{h \rightarrow 0} \int_{\Gamma} \beta(\mathbf{y}) \frac{\partial \Phi(\mathbf{x} \pm h \mathbf{n}_x^+, \mathbf{y})}{\partial n_x^+} dS(\mathbf{y}) = \int_{\Gamma} \beta(\mathbf{x}) \frac{\partial \Phi(\mathbf{x}, \mathbf{y})}{\partial n_x^+} dS(\mathbf{y}) \pm \frac{1}{2} \beta(\mathbf{x}). \quad (2.16)$$

With Lemma 3 and the single layer formulation (2.14)(2.15), exterior Neumann problems with $\frac{\partial u}{\partial n}(x) = g(x)$ on the boundary can be solved.

Single Layer Formulation for the Exterior Neumann (Laplace) Problem:

1. Solve the density β ($= \frac{\partial v}{\partial n_y^+} - \frac{\partial u}{\partial n_y^+}$) from

$$\int_{\Gamma} \frac{\partial \Phi(\mathbf{x}, \mathbf{y})}{\partial n_x^+} \beta(\mathbf{y}) dS(\mathbf{y}) + \frac{1}{2} \beta(\mathbf{x}) = g(\mathbf{x}), \quad \mathbf{x} \in \Gamma. \quad (2.17)$$

2. The solution u at any $\mathbf{x} \in \mathbb{R}^m \setminus \bar{\Omega}$ can be obtained using the integral

$$u(\mathbf{x}) = \int_{\Gamma} \Phi(\mathbf{x}, \mathbf{y}) \beta(\mathbf{y}) dS(\mathbf{y}), \quad \mathbf{x} \in \mathbb{R}^m \setminus \bar{\Omega}. \quad (2.18)$$

Analogously, we take the normal derivative of (2.8) on \mathbf{x} and obtain the double layer formulation for the exterior Neumann Laplace problem.

Double Layer Formulation for the Exterior Neumann (Laplace) Problem:

1. Solve the density β ($= u - v$) from

$$\frac{\partial}{\partial n_x^+} \int_{\Gamma} \frac{\partial \Phi(\mathbf{x}, \mathbf{y})}{\partial n_y^+} \beta(\mathbf{y}) dS(\mathbf{y}) = g(\mathbf{x}), \quad x \in \Gamma. \quad (2.19)$$

2. The solution u at any $\mathbf{x} \in \Omega$ can be obtained using the integral

$$u(\mathbf{x}) = \int_{\Gamma} \frac{\partial \Phi(\mathbf{x}, \mathbf{y})}{\partial n_y^+} \beta(\mathbf{y}) dS(\mathbf{y}), \quad \mathbf{x} \in \mathbb{R}^m \setminus \bar{\Omega}. \quad (2.20)$$

For the exterior Laplace Neumann problem, the single layer formulation is a more popular choice. The double layer inversion (2.19) for the Neumann Problem contains a second derivative of the fundamental solution. The integral (2.19) is hypersingular and does not converge in the Riemann sense. We discuss more in depth why we are interested in this integral for wave scattering problems in Chapter 5.

2.2 Formulations on a Multiply-Connected Region

In this section, we focus on the more popular double layer formulation for the Dirichlet Laplace problem. For the exterior problem of one component, the derivation is similar to the previous section with two complications:

1. The far-field value u_∞ (for \mathbb{R}^m , $m \geq 3$).
2. Unlike $\mathcal{D} + \frac{1}{2}\mathcal{S}$, the operator $\mathcal{D} - \frac{1}{2}\mathcal{S}$ has nontrivial null space. The null space is one dimensional generated by ψ_0 , where $\int \frac{\partial \psi_0}{\partial n} = 0$.

It can be shown that $\left\langle \frac{1}{|r|^{m-2}}, \psi_0 \right\rangle \neq 0$ for \mathbb{R}^m . With a modified kernel to cover the null space, the double layer formulation for the exterior (of one component) Dirichlet Laplace problem takes a similar form as (2.10)(2.11).

Double Layer Formulation for the Exterior Dirichlet (Laplace) Problem:

1. Solve the density β from

$$\int_{\Gamma} \beta(\mathbf{y}) \left(\frac{\partial \Phi(\mathbf{x}, \mathbf{y})}{\partial n_{\mathbf{y}}^+} - \frac{1}{|\mathbf{x} - \mathbf{y}|^{m-2}} \right) dS(\mathbf{y}) - \frac{1}{2} \beta(\mathbf{x}) = f(\mathbf{x}) - u_\infty, \quad x \in \Gamma. \quad (2.21)$$

2. The solution u at any $\mathbf{x} \in \Omega^+$ can be obtained using the integral

$$u(\mathbf{x}) = \int_{\Gamma} \beta(\mathbf{y}) \left(\frac{\partial \Phi(\mathbf{x}, \mathbf{y})}{\partial n_{\mathbf{y}}^+} - \frac{1}{|\mathbf{x} - \mathbf{y}|^{m-2}} \right) dS(\mathbf{y}) + u_\infty, \quad x \in \mathbb{R}^m \setminus \bar{\Omega}, \quad (2.22)$$

where $u_\infty = 0$ for $m = 2$.

For a multiply-connected region with L holes $\{\Omega_i\}_{i=1}^L$, the null space of the operator becomes more complicated and functions perpendicular to the image (or inside the null space) of

the integral operator need to be added to the layer formulations. In short, one can use the span of $\{\Phi(\mathbf{x} - \mathbf{z}_i)\}$ ($i = 1 \dots L$) to cover the null space of the integral operator, where \mathbf{z}_i is inside each hole Ω_i . For an extensive justification of the formulation, we refer interested readers to [Mikhlin *et al.* (1964); Greenbaum *et al.* (1993)]. We list the three categories for a general multiply connected region and summarize the double layer formulations for each respective Dirichlet Laplace problem.

General Double Layer Formulation for the exterior Dirichlet (Laplace) Problem in 2D:

Let $\mathbb{R}^2 \setminus \bar{\Omega}$ be a region with boundary $\Gamma = \cup_{i=1}^L \Gamma_i$, where each Γ_i is \mathcal{C}^2 . Namely, $\mathbb{R}^2 \setminus \bar{\Omega}$ has L holes, each denoted Ω_i . Then the Dirichlet Laplace problem can be solved with the following procedure

1. Solve β, A_i ($i = 1 \dots L$) for $\mathbf{x} \in \Gamma$ from the following system:

$$\begin{cases} \int_{\Gamma} \left(\frac{\partial \Phi(\mathbf{x}, \mathbf{y})}{\partial \mathbf{n}_{\mathbf{y}}} - 1 \right) \beta(\mathbf{y}) dS(\mathbf{y}) - \frac{1}{2} \beta(\mathbf{x}) + \sum_{i=1}^L A_i \Phi(\mathbf{x} - \mathbf{z}_i) = f(\mathbf{x}), \\ \sum_{i=1}^L A_i = 0. \\ \int_{\Gamma_i} \beta(\mathbf{y}) dS(\mathbf{y}) = 0, \quad i = 1 \dots L - 1. \end{cases} \quad (2.23)$$

2. The solution for $x \in \mathbb{R}^2 \setminus \bar{\Omega}$ is represented by

$$u(\mathbf{x}) = \int_{\Gamma} \beta(\mathbf{y}) \frac{\partial \Phi(\mathbf{x}, \mathbf{y})}{\partial \mathbf{n}_{\mathbf{y}}} dS(\mathbf{y}) + \sum_{i=1}^L A_i \Phi(\mathbf{x} - \mathbf{z}_i), \quad (2.24)$$

where $\mathbf{z}_i \in \Omega_i$ are arbitrary points in the holes.

For an interior (bounded) region with L holes, we do not need the sum of coefficients to guarantee the boundedness of the solution as in the exterior case. But we need compatibility conditions for all the holes $1 \dots L$, since we have $L + 1$ boundary pieces for L holes. The result is summarized as follows.

General Double Layer Formulation for the interior Dirichlet (Laplace) Problem in 2D:

Let $\Omega \subset \mathbb{R}^2$ be a region with boundary $\Gamma = \cup_{i=0}^L \Gamma_i$, where each Γ_i is \mathcal{C}^2 and Γ_0 denote the boundary adjacent to the unbounded region. Namely Ω has L holes, each denoted Ω_i . Then the Dirichlet Laplace problem can be solved with the following procedure

1. Solve β, A_i ($i = 1 \dots L$) for $\mathbf{x} \in \Gamma$ from the following system:

$$\begin{cases} \int_{\Gamma} \frac{\partial \Phi(\mathbf{x}, \mathbf{y})}{\partial \mathbf{n}_{\mathbf{y}}} \beta(\mathbf{y}) dS(\mathbf{y}) + \frac{1}{2} \beta(\mathbf{x}) + \sum_{i=1}^L A_i \Phi(\mathbf{x} - \mathbf{z}_i) = f(\mathbf{x}). \\ \int_{\Gamma_i} \beta(\mathbf{y}) dS(\mathbf{y}) = 0, \quad i = 1 \dots L. \end{cases}$$

2. The solution for $x \in \Omega$ is represented by

$$u(\mathbf{x}) = \int_{\Gamma} \beta(\mathbf{y}) \frac{\partial \Phi(\mathbf{x}, \mathbf{y})}{\partial \mathbf{n}_{\mathbf{y}}} dS(\mathbf{y}) + \sum_{i=1}^L A_i \Phi(\mathbf{x} - \mathbf{z}_i),$$

where $\mathbf{z}_i \in \Omega_i$ are arbitrary points within the holes.

The fundamental solution in 3D guarantees the boundedness of the extra terms $\sum_{i=1}^L A_i \Phi(\mathbf{x} - \mathbf{z}_i)$. Therefore the formulation for an interior or an exterior region in 3D is almost identical.

General Double Layer Formulation for the Dirichlet (Laplace) Problem in 3D:

Let Ω be a region with boundary $\Gamma = \cup_{i=0}^L \Gamma_i$, where each Γ_i is connected and Γ_0 is the boundary adjacent to the unbounded region, if such boundary exists. Namely, Ω has L holes, each denoted Ω_i . Then the Dirichlet Laplace problem can be solved with the following procedure

1. Solve β, A_i ($i = 1 \dots L$) for $\mathbf{x} \in \Gamma$ from the following system:

$$\begin{cases} \int_{\Gamma} \left(\frac{\partial \Phi(\mathbf{x}, \mathbf{y})}{\partial \mathbf{n}_{\mathbf{y}}} - \frac{1}{|\mathbf{x} - \mathbf{y}|} \right) \beta(\mathbf{y}) dS(\mathbf{y}) - \frac{1}{2} \beta(\mathbf{x}) + \sum_{i=1}^L A_i \Phi(\mathbf{x} - \mathbf{z}_i) = f(\mathbf{x}) - u_{\infty}. \\ \int_{\Gamma_i} \beta(\mathbf{y}) dS(\mathbf{y}) = 0, \quad i = 1 \dots L. \end{cases} \quad (2.25)$$

2. The solution for $x \in \Omega$ is represented by

$$u(\mathbf{x}) = \int_{\Gamma} \beta(\mathbf{y}) \frac{\partial \Phi(\mathbf{x}, \mathbf{y})}{\partial \mathbf{n}_{\mathbf{y}}} dS(\mathbf{y}) + \sum_{i=1}^L A_i \Phi(\mathbf{x} - \mathbf{z}_i) + u_{\infty}, \quad (2.26)$$

where $\mathbf{z}_i \in \Omega_i$ are arbitrary points within the holes. If Ω is an interior region, then $u_{\infty} = 0$.

To show these linear integral systems are uniquely solvable, we cite some of the results from potential theory and boundary integral equations in [Kress (2012)]. We begin with properties of a compact linear operator.

Lemma 4. *Let $K : X \rightarrow X$ be a compact linear operator on a normed linear space X , then $I - K$ is injective iff it is surjective.*

Therefore, we only need to show the operators we deal with is linear, compact, and is either injective or surjective. Furthermore, we have the characteristic of the spectrum of compact

linear operators.

Lemma 5. *Let $K : X \rightarrow X$ be a compact linear operator. The spectrum $\sigma(K)$ consists of only point spectrum, $0 \in \sigma(K)$ and $\sigma(K)$ is at most countable.*

This tells us that once we can confirm the linear integral equation consist of a compact linear integral operator, we only need to make sure the eigenspace is $\{0\}$ for the system to be uniquely solvable. Since linearity is readily established, we only need to worry about compactness. However, from the usual derivations in Fredholm Theory, one has the following result:

Theorem 1. *Integral operator with continuous or weakly singular kernel is a compact operator on $\mathcal{C}(\Gamma)$ if Γ is of class \mathcal{C}^1 .*

Using this theorem, one can show compactness for \mathcal{S} , \mathcal{D} , \mathcal{D}^* and the modified kernels for exterior and multiply connected regions since all the kernels are at most weakly singular. Because linear combination of compact operators are again a compact operator, one can verify that the previous formulations consist of compact operators on $\mathcal{C}(\Gamma)$. We only need to worry about covering the eigenspaces. We refer the details of how the eigenspaces are covered by modified Laplace kernels for exterior problems to [Kress (2012)], and for multiply connected regions to [Mikhlin *et al.* (1964)]. We will use the formulations (2.23)(2.24)(2.25)(2.26) as part of the simulations of the Mullins-Sekerka flow in Chapter 4.

2.3 Helmholtz Problem

The Helmholtz operator differs the Laplace operator by a constant:

$$\Delta u + k^2 u = 0. \tag{2.27}$$

Its fundamental solution Φ takes a very different form

$$\Phi(x, y) = \begin{cases} -\frac{i}{4}H_0^{(1)}(k|x-y|), & \text{if } n = 2. \\ -\frac{e^{ik|x-y|}}{4\pi|x-y|}, & \text{if } n = 3. \end{cases} \quad (2.28)$$

However, the derivation is identical formally to that of Laplace equation since the terms with constant coefficients cancel out:

$$\begin{aligned} & \int_{\Omega} (u(y)(k^2 + \Delta_y)\Phi(x, y) - \Phi(x, y)(\Delta_y + k^2)u(y)) dy \\ &= \int_{\Omega} (u(y)\Delta_y\Phi(x, y) - \Phi(x, y)\Delta_y u(y)) dy \\ &= \int_{\Gamma} \left(u(y(s)) \frac{\partial \Phi(x, y(s))}{\partial n_y^-} - \Phi(x, y(s)) \frac{\partial u(y(s))}{\partial n_y^-} \right) ds. \end{aligned}$$

Therefore formally we obtain the same formulations as the Laplace problems and we shall not repeat the derivations. The null space of the integral operators, however, are very different. While the integral operator in the single layer formulation for the exterior Neumann Laplace problem has trivial null space, the integral operator in the single layer formulation for exterior Neumann Helmholtz problem is nonempty. Furthermore, its null space is generally infinite dimensional and the basis is domain specific. Hence, there is no easy way to modify the kernel as in the case of the exterior Dirichlet Laplace problem. We leave the discussion of the solution to this problem and its numerical challenges in Chapter 5.

2.4 Numerical Methods

2.4.1 Discretization of Operator

With the derived analytic boundary integral formulations, it is natural to ask for a numerical solution. The validity of most numerical methods are based on having a discretized operator

that approximates the analytic operator, as the following theorem in [Kress (2012)]:

Theorem 2. *Let X, Y be Banach spaces and $K : X \rightarrow Y$ a bounded linear operator with bounded inverse $K^{-1} : Y \rightarrow X$. Assume the sequence of bounded linear operators $K_n : X \rightarrow Y$ converges to K in operator norm, $\|K_n - K\| \rightarrow 0$ as $n \rightarrow \infty$. Then for sufficiently large n , the inverse operators $K_n^{-1} : Y \rightarrow X$ exist and for the solutions of the equations*

$$K\beta = f, \quad K_n\beta_n = f_n,$$

we have

$$\|\beta_n - \beta\| \leq \frac{\|K^{-1}\|}{1 - \|K^{-1}(K_n - K)\|} \left(\|K_n - K\| \|\beta\| + \|f_n - f\| \right).$$

Proof. Take n so that $\|K^{-1}(K_n - K)\| < 1$, the inverse of $I - K^{-1}(K - K_n) = K^{-1}K_n$ exists and we have $K_n^{-1} = \left(I - K^{-1}(K - K_n) \right)^{-1} K^{-1}$ from the results of Neumann series. The operator norm of K_n^{-1} can also be bounded by taking this series expansion. The error result then follows from the usual splitting argument $\beta_n - \beta = K_n^{-1} \left((f_n - f) + (K - K_n)\beta \right)$. \square

The constraints on the operator can be relaxed to a compact, injective linear operator with compactness of the set $\{K_n\}$. Since we already established the compactness of the integral operators of interest in Theorem 1, the numerical solution is justified provided the integral operator is well approximated.

Many numerical methods have been proposed to discretize the operators. Some of the most common methods are

1. Nyström Methods;
2. Collocation Methods;
3. Boundary Element Methods.

The Nystöm methods assumes the knowledge of an explicit parametrization of the boundary. Once the parametrization is available, we can discretize the parametric space as we discretize

the iterated rectangular integral in $m - 1$ dimensions (for example, a trapezoidal rule or a Gaussian quadrature method). The advantage of the Nyström method is that the inversion and evaluation of the discretized integral can be computed with high order accuracy. However, it is usually very difficult to obtain the explicit parametrization of the boundary in high dimensions and complicated geometry.

The collocation methods pick a collection of points (collocation points) on the boundary and assumes the solution (in this case the density) lies a finite dimensional space with undetermined coefficients. The space can be chosen to be polynomials or truncated trigonometric functions among other candidates, and the collocation points are also at the discretion of the solver. Common choices include equidistant points and the Gauss-Legendre methods. Once the model solution and the quadrature points are chosen, the collocation method then solves the parameters to fit the solution.

Boundary element methods (BEM) partition the boundary into meshes. The interaction between each boundary element is then computed numerically to fit the given boundary data. It is usually necessary to devise a mechanism to deal with singularities of fundamental solutions for close elements. For polygonal mesh, analytic computations are available. But it is usually quite costly to do a numerical computation for more general meshes.

2.4.2 Other Relevant Methods

Two main challenges arise in boundary integral methods. One is that the discretized integral operator is usually a dense matrix and can be costly to compute and store. The other difficulty is the singularity of the kernel from the Green's function.

A number of fast summation methods are developed for computational efficiency. Among the popular choices are evaluation using tree structures [[Barnes & Hut \(1986\)](#)] and the fast multipole methods (FMMs) [[Greengard & Rokhlin \(1987\)](#)], where one takes advantage of the weaker interaction of the far elements and the accumulation of each layered interaction. The

method is widely used in BEM and the computation cost at each evaluation point can be as fast as $\mathcal{O}(N)$, where N is the number of elements. FMMs have been widely researched to generalize to a wider class of elliptic kernels [Ying *et al.* (2004)] and oscillatory kernels with high frequencies [Engquist & Ying (2007)].

For the second problem, popular methods include the cancellation of singularities, the regularization of the kernels, and taming the singularity of the kernel with density functions using integration by part. With the assumption of a smooth expansion of the potential on either side of the boundary, a quadrature by expansion (QBX) method [Klockner *et al.* (2013)] is developed recently to evaluate the singular integrals.

Finally, we note that there is a BIM in the level set framework simulating front propagation problems [Beale & Strain (2008)]. However, it should be considered as an explicit interface method, since the algorithm operates on line segments extracted from the level set functions.

Chapter 3

Level Set Methods

3.1 Introduction

Given an interface Γ of codimension one in \mathbb{R}^m bounding an open region Ω , the level set method [Osher & Sethian (1988)] represents Γ by the zero level set of a real-valued Lipschitz continuous function ϕ . We ask that the level set function ϕ satisfy the following properties:

$$\begin{cases} \phi(\mathbf{x}) > 0 & , \mathbf{x} \in \Omega. \\ \phi(\mathbf{x}) = 0 & , \mathbf{x} \in \Gamma = \partial\Omega. \\ \phi(\mathbf{x}) < 0 & , \mathbf{x} \in \mathbb{R}^m \setminus \bar{\Omega}. \end{cases}$$

Then ϕ embeds the interface as its zero level set $\Gamma = \{\mathbf{x} \in \mathbb{R}^m | \phi(\mathbf{x}) = 0\}$. Geometric information, such as interface normal \mathbf{n} or curvatures κ_i , can be obtained from the derivatives of this function. Furthermore, by including a time dependency $\phi = \phi(\mathbf{x}, t)$, dynamics of an interface can be modeled with the natural extended embedding $\Gamma_t = \Gamma(t) = \{\mathbf{x} \in \mathbb{R}^m | \phi(\mathbf{x}, t) = 0\}$.

In the level set framework, the motion of an interface is analyzed by convecting the level set values with the velocity field $v = \frac{\partial \mathbf{x}}{\partial t}$ or a normal velocity (scalar) field on the interface

$V_n = \mathbf{v} \cdot (-\mathbf{n}) = \mathbf{v} \cdot \frac{\nabla\phi}{|\nabla\phi|}$. Take the full derivative of the level set, this advection equation is

$$\phi_t + \nabla\phi \cdot \mathbf{v} = 0.$$

or

$$\phi_t + V_n |\nabla\phi| = 0. \quad (3.1)$$

Theoretical justification for the robustness of (3.1), where the velocity field is related to the geometry of the interface, follows the theory of viscosity solutions for scalar, time-dependent PDEs [Chen *et al.* (1991); Evans & Spruck (1991)]. With the theory of viscosity solutions [Crandall *et al.* (1992); Barles & Da Lio (2004)], which applies to a more general array of equations, researchers of level set methods are able to design numerical algorithms converging to the unique analytic solutions. The motion of the interface is then modeled by evolving the function ϕ and tracking the zero level set of ϕ at any given time t .

There are three main advantages of using level set methods on front propagation problems. First, the formulation is independent of the dimensions of the modeled problem. Second, evolving the function ϕ in one higher dimension naturally permits cusps, corners, and topological changes in its zero level set describing the interface Γ . Third, the common flows with normal speed V_n related to geometric properties such as unit normal vector and mean curvature can be conveniently computed from level set values. For example, the unit normal vector is

$$\mathbf{n} = -\frac{\nabla\phi}{|\nabla\phi|},$$

and the mean curvature κ has level value representation

$$\kappa = \nabla \cdot \frac{\nabla\phi}{|\nabla\phi|}.$$

These advantages make the level set method a competitive and popular choice for analyzing

interface dynamics in various physical and mathematical models [Chen *et al.* (1991); Osher & Fedkiw (2000)].

3.2 Distance Re-initialization and Value Extension

3.2.1 Distance Re-initialization

The level set function ϕ is not unique: Any product with a positive function (for example, $e^{c|\mathbf{x}|}$ for any $c \in \mathbb{R}$) gives another nontrivial way of describing the same zero set. It is possible that solution to a level set equation (for example, (3.1)) is not suitable for subsequent numerical computations. Therefore, it is a legitimate question to ask for a “best” level set function for numerical algorithms.

We should seek a level set function that produces the smallest error during numerical computations. When we simulate interface dynamics, errors can come from numerically solving the time dependent PDE and extracting the interface location at each time t . On the one hand, solving a PDE usually prefers a smaller $\nabla\phi$ (in each direction) because of its presence in the Taylor’s expansion errors when we discretize functions on a grid. On the other hand, locating the interface usually implies a small value of $\frac{1}{(\nabla\phi)_j}$ (in each direction) is more desirable because it is related to the error terms when we try to find the roots of ϕ in a cell using interpolation algorithms. Following these discussions, it is intuitive to see that the signed distance function to the zero level set d_Γ is a good representation because $|\nabla d_\Gamma| = 1$ almost everywhere. We give a formal definition of the signed distance function to an interface Γ :

Definition 3. The signed distance function of an interface Γ which encloses bounded region Ω takes the following values:

$$d_\Gamma(\mathbf{x}) = \begin{cases} \min_{\mathbf{y} \in \Gamma} \|\mathbf{x} - \mathbf{y}\|, & \mathbf{x} \in \Omega. \\ -\min_{\mathbf{y} \in \Gamma} \|\mathbf{x} - \mathbf{y}\|, & \mathbf{x} \in \mathbb{R}^m \setminus \bar{\Omega}. \end{cases}$$

The analytic formula of a signed distance function does not exist except in very special cases. Given a level set function, the process of reshaping the level set function into a signed distance function is called *distance re-initialization* or *redistancing*. Studies for redistancing level set functions began with the works of [Dervieux & Thomasset (1980, 1981); Sussman *et al.* (1994); Adalsteinsson & Sethian (1995)]. There are two main categories of redistancing algorithms: one directly works on the static boundary value problem characterizing the distance function, whereas the other designs a flow to obtain the distance function in its steady state. Examples of the former group include fast marching [Tsitsiklis (1995); Helmsen *et al.* (1996); Sethian (1996)] and fast sweeping [Tsai *et al.* (2003); Zhao (2004)] methods.

The advantages of direct methods include are their near optimal time complexity and their stability in maintaining the location of the interface, while the main drawback is the difficulty to achieve high order accuracy. Flow based methods are flexible in implementing different orders of accuracy and can be conveniently parallelizable. However, the location of the interface can be excessively perturbed without a sacrifice of convergence speed to steady state. Examples of flow based methods include the works of [Sussman *et al.* (1994); Peng *et al.* (1999)].

Various approaches [Russo & Smereka (2000); Chopp (2001); Cheng & Tsai (2008)] attempt to achieve high order accuracy of the interface location while controlling the sacrifice of speed. The topic of redistancing remains an active research field.

3.2.2 Standard Redistancing

A standard flow based redistancing method as in the original work of [Sussman *et al.* (1994)] is as follows:

Given a level set function ϕ_0 , propagate the following flow to steady state:

$$\begin{cases} \psi_t(\mathbf{x}, t) + \text{sgn}_\varepsilon(\mathbf{x})(|\nabla\psi(\cdot, t)| - 1) = 0, \\ \psi(\mathbf{x}, 0) = \phi_0(\mathbf{x}), \end{cases} \quad (3.2)$$

where $\text{sgn}_\varepsilon(\mathbf{x}) = \frac{\phi_0(\mathbf{x})}{\sqrt{\phi_0^2(\mathbf{x}) + \varepsilon^2}}$ is a regularized signum function of the initial data ϕ_0 .

We note that if we use a usual discretization for the Hamiltonian, the method will not converge, as discussed in [Osher & Fedkiw (2000)]. Instead, we need to use the upwinding Godunov Hamiltonian as in [S. Osher (1991); Tsai & Osher (2003, 2005)]. In 2D,

$$H_G(p_-, p_+, q_-, q_+) = \sqrt{\max\{p_-^+, p_+^-\}^2 + \max\{q_-^+, q_+^-\}^2},$$

where $p_\pm = D_\pm^x \phi_{i,j}$, $q_\pm = D_\pm^y \phi_{i,j}$, and $x^+ = \max(x, 0)$, $x^- = -\min(x, 0)$. In 3D, the Godunov scheme follows analogously:

$$\hat{H}_G(p_-, p_+, q_-, q_+, r_-, r_+) = \sqrt{\max\{p_-^+, p_+^-\}^2 + \max\{q_-^+, q_+^-\}^2 + \max\{r_-^+, r_+^-\}^2},$$

where $r_\pm = D_\pm^z \phi_{i,j}$. In the simulations of this thesis, we take a WENO-3 [Jiang & Peng (1997)] approach on the spatial finite difference operation D_\pm . Equation (4.5) is then propagated with a TVD-RK3 scheme [Gottlieb & Shu (1998)]. Namely, for each time step n , we sequentially

compute

$$\begin{aligned}
\tilde{\psi}^{(1)} &= \psi^n + \Delta t \mathcal{L}(\psi^n), \\
\tilde{\psi}^{(2)} &= \frac{3}{4}\psi^n + \frac{1}{4}\tilde{\psi}^{(1)} + \frac{1}{4}\Delta t \mathcal{L}(\tilde{\psi}^{(1)}), \\
\psi^{n+1} &= \frac{1}{3}\psi^n + \frac{2}{3}\tilde{\psi}^{(2)} + \frac{2}{3}\Delta t \mathcal{L}(\tilde{\psi}^{(2)}),
\end{aligned} \tag{3.3}$$

where Δt is the mesh size of the time dimension and \mathcal{L} in the standard redistancing case is as in (4.5), $\mathcal{L}(\psi) := \frac{\psi_0}{\sqrt{\psi_0^2 + \varepsilon^2}}(1 - |\nabla \psi|)$.

The regularization parameter ε for the signum function affects the convergence speed and the stability of the interface location. If we take ε to be zero (unregularized case), the coefficient of the PDE is discontinuous and numerical approximations will move the zero level set from the original interface. If we take ε to be large, however, the coefficient will be smooth for numerical approximation but the characteristics traveling at speed $\text{sgn}_\varepsilon(\mathbf{x})$ will make the convergence slow. In practice, ε is often taken to be a multiple of the mesh size. Common choices include cH [Sussman *et al.* (1994)] and $c|\nabla \phi_0|H$ [Peng *et al.* (1999)], where $H = \Delta x$ is the mesh size. However, convergence results of the flow PDE using these choices are unknown. [Cheng & Tsai (2008)] circumvents the dilemma of regularization by propagating the standard time dependent eikonal equation $\psi_t + |\nabla \psi| = 0$ while keeping record of the time traveled. This method can also be used for value extension, as briefed in the following section.

3.2.3 Value Extension

When we simulate front propagation problems using level set methods, the embedding of the interface requires the definition of velocity values on not only the interface, but at least also on the grid points in a tubular neighborhood of the interface in order to apply a full Eulerian approach as in (3.1). For consistency, we should require the velocity defined off interface to smoothly approach the velocity on interface as one approaches the zero level set. That is, for

a smooth normal velocity field on the boundary Γ and a point $\mathbf{x}^* \in \Gamma$, we should require

$$\lim_{\mathbf{x} \rightarrow \mathbf{x}^*} V_n(\mathbf{x}) = V_n(\mathbf{x}^*).$$

The work of [Malladi *et al.* (1995)] introduced the idea of defining an extension velocity at each point as the velocity value at its closest point on the interface. When the level sets and the velocity field are both smooth, it can be shown [Zhao *et al.* (1996)] that the signed distance function is maintained after propagation in (3.1). This constructed velocity field satisfies

$$\nabla V_n \cdot \nabla \phi = 0.$$

Similar to the redistancing algorithm, one way to construct the extended velocity field is to propagate velocity information outward from the boundary with the above characteristics:

$$\frac{\partial V_n}{\partial t} + \text{sgn}_\varepsilon(\phi) \frac{\nabla \phi}{|\nabla \phi|} \cdot \nabla V_n = 0.$$

This flow inherits the advantages and drawbacks of the standard redistancing. The time dependent flow based method [Cheng & Tsai (2008)] on each side of the interface is proposed to avoid the dilemma of picking a proper regularization parameter ε .

We note that front propagation problems using level set methods usually do not require redistancing or velocity extension in the whole space. Since the zero level set is where the interface lies, the computation domain is often confined to a thin tubular neighborhood of the interface for efficiency.

3.3 Implicit Boundary Integral Method (IBIM)

The implicit boundary integral method (IBIM) [Kublik *et al.* (2013)] solves PDEs with boundary integral formulations (as discussed in Chapter 2) using a level set approach. Assuming the

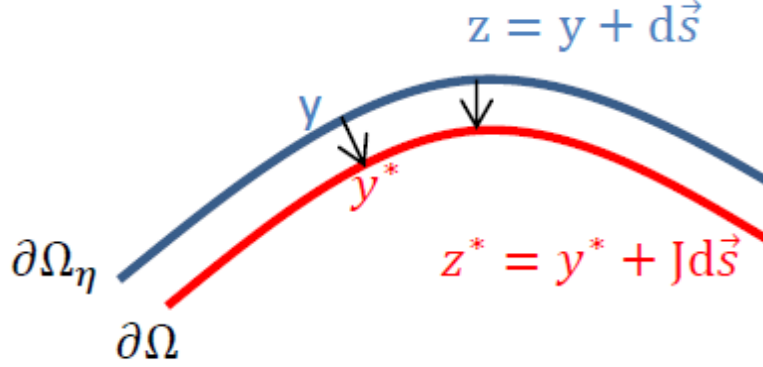


Figure 3.1: Parametrization from parallel interface.

boundary $\partial\Omega = \Gamma$ is \mathcal{C}^2 , the main task is to compute a boundary integral with only a level set description (instead of an explicit parametrization) of the boundary Γ . We briefly describe this method below, as it plays a crucial role in the simulations and subsequent derived formulations in this thesis. Without the loss of generality, we discuss the case where the level set function is readily redistanced as in Section 3.2 to focus on the gist of this method.

The IBIM contains three main ingredients. First, we need a quadrature to embed the integrand function into the neighborhood of the boundary. Second, once we can assign integrand values to each level set within the neighborhood, we need an effective way to average across all level sets within the computation domain in the normal direction to approximate original boundary integral. Third, for a singular kernel, which is usually the case for BIMs, we need a regularization scheme.

3.3.1 Integrand Embedding

Given a boundary integral $\int_\Gamma U(y(s)) dS(y)$, we can apply the idea of velocity extension seen in level set methods and embed the integrand into the neighborhood of Γ . Denote the ε tubular neighborhood $T_{[-\varepsilon, \varepsilon]}$. For a \mathcal{C}^2 boundary Γ , ε can be as large as $\min_{i=1}^m \frac{1}{\kappa_i}$, where κ_i denotes each principal curvature of the interface Γ . For $\mathbf{y} \notin \Gamma$, the function $F(\mathbf{y})$ takes the value of its

closest point on the boundary $F(\mathbf{y}^*)$, where the star operation denotes the projection onto the boundary Γ :

$$\mathbf{y}^* = \mathbf{y} - d_\Gamma(\mathbf{y})\nabla d_\Gamma(\mathbf{y}). \quad (3.4)$$

As [Kublik *et al.* (2013)] shows, the value extension can be understood as a parametrization from a parallel interface $\Gamma_\eta = \partial\Omega_\eta$ for level set η as illustrated in Figure 3.1. That is,

$$\int_\Gamma U(y(s)) ds = \int_{\Gamma_\eta} U(y^*(s_\eta)) J_\eta ds_\eta. \quad (3.5)$$

The Jacobian J_η for using this parametrization from a parallel boundary $\Gamma_\eta \in \mathbb{R}^m$ is computed to be

$$J_\eta = J(s_\eta) = \begin{cases} 1 + \eta \kappa_\eta, & \text{if } m = 2, \\ 1 + 2\eta H_\eta + \eta^2 G_\eta, & \text{if } m = 3, \end{cases}$$

where κ_η denotes the curvature at $\mathbf{y}(s_\eta)$ on the level set η , and H_η , G_η denote the mean curvature and Gaussian curvature respectively. Using a level set representation, we can define the Jacobian as a function in the space

$$J(y) := \begin{cases} 1 - d_\Gamma(y)\Delta d_\Gamma(y), & \text{if } m = 2. \\ 1 - d_\Gamma(y)\Delta d_\Gamma(y) + d_\Gamma^2(y) \langle \nabla d_\Gamma(y), \text{adj}(\text{Hess}(d_\Gamma))\nabla d_\Gamma(y) \rangle, & \text{if } m = 3. \end{cases} \quad (3.6)$$

3.3.2 Averaging Over Different Parametrizations

For a boundary integral $\int_\Gamma U(y(s)) dS(y)$, one can analytically write down

$$\int_\Gamma U(y(s)) ds = \int_{\mathbb{R}^m} U(\mathbf{y}) \delta(d_\Gamma(\mathbf{y})) d\mathbf{y}, \quad (3.7)$$

where δ is the Dirac delta distribution. The traditional approach is to approximate (3.7) by replacing the Dirac δ with a smeared out bump function. As [Tornberg & Engquist (2004)] points out, it is a non-trivial task to regularize the δ function on a thin tubular neighborhood of size ε without producing $\mathcal{O}(1)$ error. Various approaches [Engquist *et al.* (2005); Smereka (2006); Towers (2007); Zahedi & Tornberg (2010)] have been proposed to numerically approximate this delta function in a consistent manner. However, even with these attempts, they can introduce an analytical error of $\mathcal{O}(\varepsilon)$.

The IBIM introduced by [Kublik *et al.* (2013)] is an analytically exact formulation. Once the value extension is available for different level sets, the boundary integral can be transformed into an exact tubular integral by averaging over all the level sets with a regularized Dirac δ and the correct weight for each value extension, as shown in Figure 3.2. We define $U_\Gamma := U(\mathbf{y}^*)J(\mathbf{y})$ to be the weighted restriction to its zero level set (the boundary Γ). The transformation of BIM into the IBIM takes the following form:

$$\begin{aligned}
& \int_\Gamma U(y(s)) ds \\
&= \int_{-\varepsilon}^{\varepsilon} \delta_\varepsilon(\eta) \int_{\Gamma_\eta} U_\Gamma(\mathbf{y}(s_\eta)) ds_\eta d\eta \\
&= \int_{\mathbb{R}^m} U_\Gamma(\mathbf{y}) \delta_\varepsilon(d_\Gamma(\mathbf{y})) dy \\
&= \int_{T_{[-\varepsilon, \varepsilon]}} U_\Gamma(\mathbf{y}) \delta_\varepsilon(d_\Gamma(\mathbf{y})) dy, \tag{3.8}
\end{aligned}$$

where we use $T_{[-\varepsilon, \varepsilon]}$ to denote the tube of width ε centered at the interface Γ . This integral can be viewed as a weighted average of the value extensions on all neighboring level sets. We summarize the theorem from [Kublik *et al.* (2013)]:

Theorem 3. *Consider a \mathcal{C}^2 compact hyper-surface $\Gamma \subset \mathbb{R}^m$ with principal curvatures denoted κ_i . Let d_Γ be the signed distance function of Γ , $\delta_\varepsilon : \mathbb{R} \rightarrow \mathbb{R}$ be a regularized Dirac δ , compactly supported on $[-\varepsilon, \varepsilon]$. If U is a continuous function defined on Γ , $U_\Gamma := U(\mathbf{y}^*)J(\mathbf{y})$ where J*

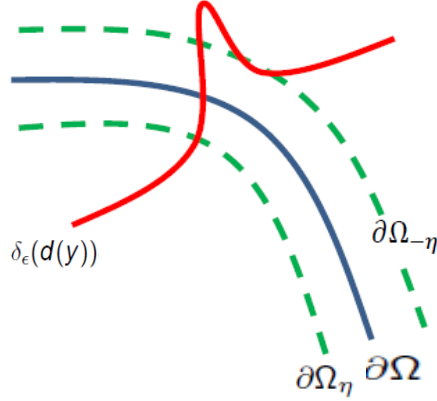


Figure 3.2: Averaging with a regularized Dirac delta function over level sets.

defined as in (3.6), then for all ϵ , $\min_{1 \leq i \leq m-1} |\frac{1}{\kappa_i}| > \epsilon > 0$, we have

$$\int_{\Gamma} U(\mathbf{y}(s)) ds = \int_{\mathbb{R}^m} U_{\Gamma}(\mathbf{y}) \delta_{\epsilon}(d_{\Gamma}(\mathbf{y})) dy.$$

The higher order derivatives of the distance function in this formulation can cause numerical inaccuracy. We note that a cleaner and more accurate formulation for computing the Jacobian using singular value decomposition has been developed [Kublik & Tsai (2015)].

3.3.3 Kernel Regularization

As illustrated in Figure 3.3, the fundamental solution $\Phi(\mathbf{x}, \mathbf{y})$ usually has singularity at $\mathbf{x} = \mathbf{y}$. Even though the boundary integral exists, regularization schemes must be applied for accurate numerical approximations. In the paper of [Kublik *et al.* (2013)], the method used is to pick an interface with second order contact and compute the near field quadrature analytically, as shown in Figure 3.4. For singular kernels, the method computes the regularized integral analytically and take the average value on the element as its quadrature. Therefore, this method can be applied to both weakly singular kernels, where the integrand limit exists, and singular kernels where the integral values exist. For hypersingular kernels, where the integral does not exist in the Riemann sense, we discuss our regularization scheme in 5.

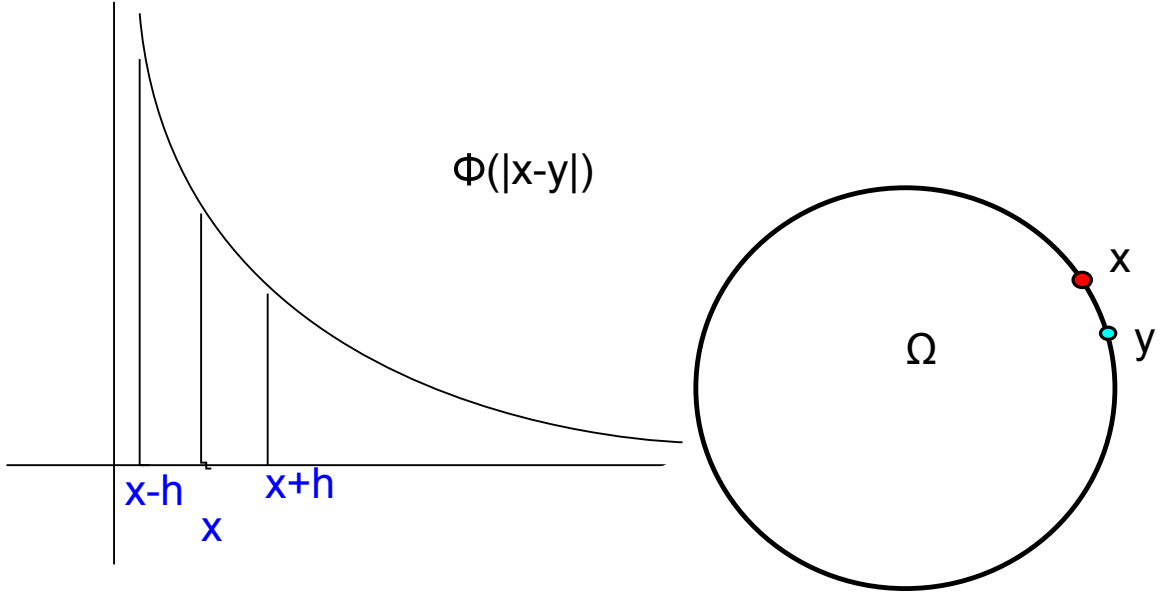


Figure 3.3: Kernel singularity for close points.

The regularization quadrature in [Kublik *et al.* (2013)] for the normal derivative of the fundamental solution of the Laplace equation is

$$\left(\frac{\partial\Phi}{\partial n_y}(x^*,y^*)\right)_{reg} = \begin{cases} \frac{\kappa(y^*)}{4\pi}, & m = 2, \\ \frac{1}{4\pi\tau}H(y^*) - \frac{\tau}{\pi}\left(\frac{5}{256}H(y^*)(4H^2(y^*) - G(y^*)) + \frac{25}{768}H(y^*)G(y^*)\right), & m = 3, \end{cases} \quad (3.9)$$

where τ is the radius of the regularization patch. κ , H , G denote the curvature, mean curvature, and Gaussian curvature respectively. With this regularization scheme, implicit boundary integrals in the formulation of the interior Dirichlet Laplace problem can achieve at least second order accuracy in both two and three dimensions. For the Neumann Helmholtz problem in (5), the regularization quadrature of the singular kernel can be calculated following similar approximation process. See Appendix A for the derivation details.

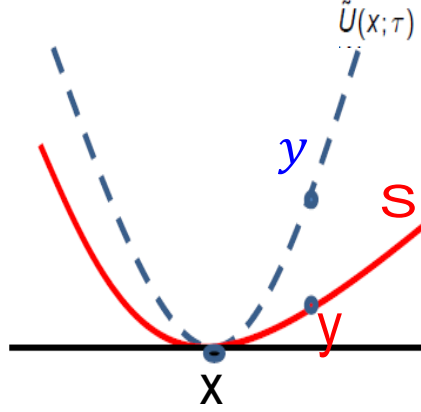


Figure 3.4: Compute an analytic regularization quadrature by approximating the true interface S with a second order contacting curve.

3.3.4 Discretization on Cartesian Grids

We illustrate the numerical procedures for solving a differential equation under IBIM. Take the double layer formulation (2.10)(2.11) for example. By plugging the kernel into (3.8), $U(\mathbf{y}) := \frac{\partial \Phi}{\partial n_{\mathbf{y}}}(\mathbf{x}, \mathbf{y})\beta(\mathbf{y})$, we obtain the analytic form of the double layer formulation (for interior Dirichlet Laplace Problem) under IBIM:

Double Layer Formulation for the Interior Dirichlet (Laplace) Problem using IBIM

1. Obtain the density β with the Dirichlet boundary condition

$$\int_{T_{[-\varepsilon, \varepsilon]}} \frac{\partial \Phi}{\partial n_{\mathbf{y}}}(\mathbf{x}^*, \mathbf{y}^*)\beta(\mathbf{y}^*)J(\mathbf{y})\delta_{\varepsilon}(d_{\Gamma}(\mathbf{y}))dy + \frac{1}{2}\beta(\mathbf{x}^*) = u(\mathbf{x}^*) = f(\mathbf{x}^*) \quad x^* \in \Gamma. \quad (3.10)$$

2. For any point $\mathbf{x} \in \Omega$, the solution can be evaluated with the boundary integral

$$u(\mathbf{x}) = \int_{T_{[-\varepsilon, \varepsilon]}} \frac{\partial \Phi}{\partial n_{\mathbf{y}}}(x, \mathbf{y}^*)\beta(\mathbf{y}^*)J(\mathbf{y})\delta_{\varepsilon}(d_{\Gamma}(\mathbf{y}))dy \quad x \in \Omega. \quad (3.11)$$

Now we describe how we discretize (3.10) to invert the integral operator and obtain β . Recall that the star operation (3.4) is a projection onto the interface Γ . For each grid point

\mathbf{x}_i on a standard uniform Cartesian grid discretizing $[a, b]^m \subset \mathbb{R}^m$ with mesh size $\Delta x = H$, we define

$$\mathbf{x}_i^* = \mathbf{x}_i - d_i \nabla_H d_i,$$

where $d_i := d_\Gamma(\mathbf{x}_i)$ denotes the signed distance of \mathbf{x}_i ,

$$\nabla_H d_i := (D_{1,H}^c d_i, \dots, D_{m,H}^c d_i)$$

is the discrete gradient operator, which uses central finite differencing

$$D_{j,H}^c d_i := \frac{d_{i+e_j} - d_{i-e_j}}{2H} = \frac{d_{i_1, \dots, i_{j+1}, \dots, i_m} - d_{i_1, \dots, i_{j-1}, \dots, i_m}}{2H} \quad (3.12)$$

in each coordinate direction, $1 \leq j \leq m$. For computing the Jacobian J , we use the standard discrete Laplacian operator

$$\Delta_H d_i := \sum_{j=1}^m D_{j,H}^+ D_{j,H}^- d_i,$$

where

$$D_{j,H}^+ d_i := \frac{d_{i+e_j} - d_i}{H} = \frac{d_{i_1, \dots, i_{j+1}, \dots, i_m} - d_{i_1, \dots, i_m}}{H}, \quad (3.13)$$

$$D_{j,H}^- d_i := \frac{d_i - d_{i-e_j}}{H} = \frac{d_{i_1, \dots, i_m} - d_{i_1, \dots, i_{j-1}, \dots, i_m}}{H}, \quad (3.14)$$

denote the first order forward and backward finite difference on the j th coordinate respectively.

We address each component in (3.10)(3.11) after discretization. For the kernel, since $\frac{\partial \Phi}{\partial n_y} = \nabla \Phi \cdot n_y = -\nabla \Phi \cdot \nabla d_\Gamma$ and the gradient of the fundamental solution $\nabla \Phi$ can be precomputed **analytically** for accuracy and efficiency. We use the notation

$$\nabla \Phi_{x,j} = \nabla \Phi(\mathbf{x}, \mathbf{x}_j^*),$$

$$\nabla \Phi_{i,j}^* = \nabla \Phi(\mathbf{x}_i^*, \mathbf{x}_j^*),$$

for the exact gradient values of the fundamental solutions ($\mathbf{x} \in \Omega$). The kernel then takes the notation

$$\begin{aligned} \left(\frac{\partial \Phi}{\partial n_y}\right)_{x,j} &:= -\nabla \Phi_{x,j} \cdot \nabla_H d_j, \\ \left(\frac{\partial \Phi}{\partial n_y}\right)_{i,j}^* &:= \begin{cases} -\nabla \Phi_{i,j}^* \cdot \nabla_H d_j, & \text{if } |\mathbf{x}_i^* - \mathbf{x}_j^*| \geq \tau. \\ \left(\frac{\partial \Phi}{\partial n_y}(\mathbf{x}_i^*, \mathbf{x}_j^*)\right)_{reg}, & \text{if } |\mathbf{x}_i^* - \mathbf{x}_j^*| < \tau. \end{cases} \end{aligned}$$

The regularization term is precomputed in (3.9). The change of variable Jacobian term is numerically computed as

$$J_i := \begin{cases} 1 - d_i \Delta_H d_i, & \text{if } m = 2. \\ 1 - d_i \Delta_H d_i + d_i^2 \langle \nabla_H d_i, \text{adj}(\text{Hess}(d_i)) \nabla_H d_i \rangle, & \text{if } m = 3. \end{cases}$$

Finally, we denote

$$\begin{aligned} f_i^* &= f(\mathbf{x}_i^*), \\ \beta_i^* &= \beta(\mathbf{x}_i^*), \\ \delta_i &= \delta_\varepsilon(d_i). \end{aligned}$$

Then the boundary integral equation (3.10) is discretized as

$$\sum_j H^m \left(\frac{\partial \Phi}{\partial n_y}\right)_{i,j}^* \beta_j^* \delta_j J_j + \frac{1}{2} \beta_i^* = f_i^*,$$

and the solution evaluation (3.11) is

$$u(x) = \sum_j H^m \left(\frac{\partial \Phi}{\partial n_y}\right)_{x,j} \beta_j^* \delta_j J_j.$$

We summarize the algorithm for solving a *Dirichlet Problem (on a simply connected interior region) using the IBIM formulation*:

For a given boundary integral formulation on a \mathcal{C}^2 compact boundary Γ , the algorithm for solving an interior Dirichlet Problem

$$\begin{cases} \mathcal{L}u = 0, & \mathbf{x} \in \Omega, \\ u = f, & \mathbf{x} \in \Gamma = \partial\Omega, \end{cases}$$

using implicit boundary integral formulation (IBIM) takes the following steps:

For each \mathbf{x}_i within the ε tubular neighborhood of Γ ($|d_\Gamma(\mathbf{x}_i)| < \varepsilon$), compute $\mathbf{x}_i^* = \mathbf{x}_i - d_i \nabla_H d_i$.

1. Form the matrix $D + \frac{1}{2}I$ and the vector f^* , where

$$\begin{aligned} D_{i,j} &= H^m \delta_j J_j \left(\frac{\partial \Phi}{\partial n_y} \right)_{i,j}^*, \\ f_i^* &= f(\mathbf{x}_i^*). \end{aligned}$$

2. Solve the vector β^* from the linear equation $(D + \frac{1}{2}I)\beta^* = f^*$.
3. For any $\mathbf{x} \in \Omega$, the solution is evaluated by computing

$$u(x) = \sum_j H^m \delta_j J_j \left(\frac{\partial \Phi}{\partial n_y} \right)_{x,j} \beta_j^*.$$

For the matrix inversion in 3, this thesis implements the bi-conjugate gradient stabilized method (BiCGSTAB) for both real (Laplace) or complex (Helmholtz) versions. The formulation is free to use stationary iterative methods or other Krylov space iterative solvers (for

example, the GMRES [Saad & Schultz (1986)]. For large matrices from high resolutions, a matrix-vector multiplication is implemented for memory efficiency. This avoids the need to store the dense matrix in the iterative solver. Furthermore, Fast Multipole Methods, originally introduced by [Greengard & Rokhlin (1987)], have been further developed for Laplace-type kernels [Ying *et al.* (2004)] and Helmholtz kernels [Rokhlin (1993)] with high frequencies [Engquist & Ying (2007)] for efficient matrix multiplication calculations. We expect the existing fast multipole methods can be adapted to invert these linear systems, but so far no such work has been developed to the best of our knowledge.

3.4 IBIM on Adaptive Grids

IBIM formulations such as (3.10)(3.11) have the flexibility to be implemented on adaptive grids. We see that almost all the values within the formulation remain unchanged. The only task is to obtain a signed distance function on adaptive grids and the integration quadrature on adaptive grids. [Strain (1999); Min & Gibou (2007)] proposed fast redistancing methods on adaptive grids. We will adopt the redistancing method in [Min & Gibou (2007)] and test the solution accuracy using IBIM formulations on adaptive grids. The details of the adaptive redistancing are included in Appendix B.

The experiments are done on unit circles and spheres for Dirichlet boundary conditions. For the purpose of this thesis, we shall test on Interior Laplace Problems (See 3.1 and 3.2) and Exterior Helmholtz Problem (See 3.3 and 3.4). An illustration of the tree structure of the adaptive grid is shown in Figure 3.5.

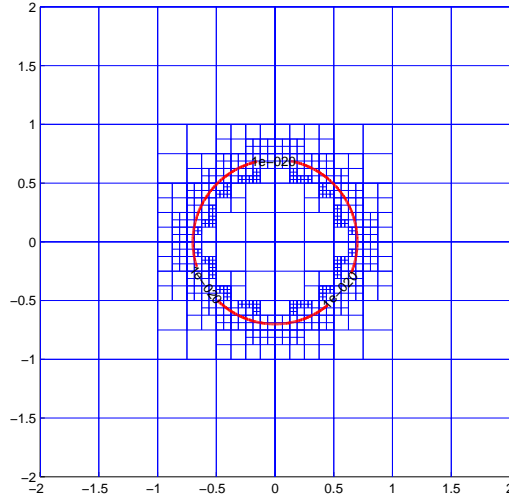


Figure 3.5: Circle on adaptive grid with curvature splitting criterion.

3.4.1 Interior Laplace Problem

The error For Laplace equation in $2D$, the exact solution u_e we test on can be expressed as

$$u_e(r, \theta) = a_0 + \sum_{n=1}^{\infty} r^n (a_n \cos(n\theta) + b_n \sin(n\theta)), \quad a_n, b_n \in \mathbb{R}.$$

Similarly for $3D$ Laplace equation, the exact solution can be expressed as

$$u_e(r, \theta, \phi) = \sum_{l=0}^{\infty} \sum_{m=0}^l (a_{lm} \cos(m\phi) + b_{lm} \sin(m\phi)) f_l^m(\cos(\theta)),$$

where

$$f_l^m(x) = (-1)^m (1-x^2)^{\frac{m}{2}} \frac{d^m}{dx^m} P_l(x), \quad P_l(x) \text{ are the Legendre polynomials.}$$

Table 3.1: Solution error of [Interior Laplace](#) problem on a circle using IBIM on an adaptive grid. The tubular neighborhood is taken to be $\varepsilon = |\nabla d_\Gamma|_1 * 2H$, where H is the cell width of the maximum resolution.

Min. resol.	Max. resol.	Int. error	Order
64^2	128^2	1.227E-01	-
128^2	256^2	5.706E-02	1.105
256^2	512^2	2.850E-02	1.002
512^2	1024^2	1.368E-02	1.059
1024^2	2048^2	6.510E-03	1.072

Table 3.2: Solution error of [Interior Laplace](#) problem on a sphere using IBIM on adaptive grid. The tubular neighborhood is taken to be $\varepsilon = |\nabla d|_1 * 2H$, where H is the cell width of the maximum resolution.

Min. resol.	Max. resol.	Int. error	Order
16^3	32^3	1.685E-02	-
32^3	64^3	5.084E-03	1.729
64^3	128^3	2.009E-04	4.662

3.4.2 Exterior Helmholtz Problem

For exterior Helmholtz problems in $2D$, the exact solution u_e we test on are in the form of

$$u_e(r, \theta) = J_0(k^2 r),$$

where J is the Bessel function of the first type. And in $3D$

$$u_e(r, \theta) = \frac{e^{ik^2 r}}{k^2 r}.$$

Table 3.3: Solution error for [exterior Helmholtz](#) problem with wave number $k = 10$ on a circle using IBIM on adaptive grid. The tubular neighborhood is taken to be $\varepsilon = |\nabla d|_1 * 2H$, where H is the cell width of the maximum resolution.

Min. resol.	Max. resol.	Ext. error	Order
64^2	128^2	6.151E-02	-
128^2	256^2	2.463E-02	1.321
256^2	512^2	1.076E-02	1.194
512^2	1024^2	4.983E-03	1.111
1024^2	2048^2	2.405E-03	1.051

Table 3.4: Solution error for [exterior Helmholtz](#) problem with wave number $k = 1$ on a sphere using IBIM on adaptive grid. The tubular neighborhood is taken to be $\varepsilon = |\nabla d|_1 * 2H$, where H is the cell width of the maximum resolution.

Min. resol.	Max. resol.	Ext. error	Order
16^3	32^3	3.755E-02	-
32^3	64^3	2.370E-02	0.664
64^3	128^3	1.490E-02	0.669

Chapter 4

IBIM for Mullins-Sekerka Dynamics

4.1 Physical Background

Mullins-Sekerka dynamics [[Mullins & Sekerka \(1963\)](#)] model the solidification process as a diffusion driven free boundary problem. Let $\Omega_t = \Omega \subseteq \mathbb{R}^m$ ($m = 2, 3$) be a fixed region that we consider our two phase problem on, $\Omega^- = \cup_{t \geq 0} \Omega_t^-$ be a family of bounded domain denoting the solid phase of the material, $\Omega_t^+ = \Omega \setminus \Omega_t^-$ the liquid phase, we are looking for a free boundary $\Gamma = \cup_{t \geq 0} \Gamma_t$ (respectively, $\Gamma_t = \partial \Omega_t^-$) and a function $u(\mathbf{x}, t) \in \mathcal{C}^2(\Omega^- \cup \Omega_t^+) \cap \mathcal{C}(\bar{\Omega}) \times \mathcal{C}^1([0, \infty))$ such that

$$\left\{ \begin{array}{ll} u_t = \alpha^2 \Delta u, & x \in \Omega_t^- \cup \Omega_t^+, t \geq 0, \\ u = f, & x \in \Gamma_t, t \geq 0, \\ \sup_{\mathbf{x} \in \Omega} |u(\mathbf{x}, t)| < \infty, & t \geq 0, \\ V_n = \frac{-1}{L_v} \left(k_S \left(\frac{\partial u}{\partial n} \right)_S + k_L \left(\frac{\partial u}{\partial n} \right)_K \right), & x \in \Gamma_t, t \geq 0, \\ \Gamma_0 = \partial \Omega_0^-, & \end{array} \right. \quad (4.1)$$

where f is a Dirichlet condition on the interface Γ_t , L_v is the latent heat required per unit volume for the phase change, k_S and $(\frac{\partial u}{\partial n})_S$ are the thermal conductivity and temperature derivative at the interface with the normal pointing toward the solid, and similarly for k_L and $(\frac{\partial u}{\partial n})_L$. We assume the boundaries Γ_t are compact and \mathcal{C}^2 .

Theoretically, the above system (4.1) for u and Γ_t needs to be solved simultaneously. For a tractable problem, we consider the slowest time scale, where phase equilibrium holds everywhere at leading order. Under the condition

$$S_T := \left| \frac{C_v(u_M - u_\infty)}{L_v} \right| \ll 1, \quad (4.2)$$

where u_M is the melting point, u_∞ is the initial temperature in Ω^+ , C_v is the heat per unit volume of the liquid. It can be shown that the solution can be found separately. That is, we can maintain a fixed interface, solve for the Laplace equation, and propagate the surface to the next instant. Inequality (4.2) usually holds in practice since $|u_M - u_\infty|$ usually must be several hundred degrees centigrade to make $S_T = 1$. Under the usual temperature of interest, we also consider the model with Gibbs-Thompson condition, which gives the Dirichlet boundary condition to be $f = -\kappa(\mathbf{x})$, the (mean) curvature of the interface at \mathbf{x} . This condition is used to describe the local equilibrium at the interface. For a more in depth model analysis, see [Langer (1980); Gurtin (1986); Pego (1989)].

With the above assumptions, the model equation (4.1) becomes the following free boundary problem: find $\Gamma = \cup_{t \geq 0} \Gamma_t$ and a function $u(\mathbf{x}, t) \in \mathcal{C}^2(\Omega^- \cup \Omega^+) \cap \mathcal{C}(\bar{\Omega}) \times \mathcal{C}^1([0, \infty))$

such that

$$\left\{ \begin{array}{ll} \Delta u(\cdot, t) = 0, & x \in \Omega_t^- \cup \Omega^+, t \geq 0. \\ u = -\kappa, & x \in \Gamma_t, t \geq 0. \\ \sup_{\mathbf{x} \in \Omega} |u(\mathbf{x}, t)| < \infty, & t \geq 0. \\ V_n = -[\partial_n u]_{\Gamma_t}, & x \in \Gamma_t, t \geq 0. \\ \Gamma_0 = \partial \Omega_0^-. \\ \left(\int_{\Gamma} \frac{\partial u}{\partial n} dS(y) = 0, \right. & \left. t \geq 0, \mathbf{x} \in \mathbb{R}^2. \right) \end{array} \right. \quad (4.3)$$

It can be shown that there exists a classical global solution [Escher & Simonett (1998)]. At any given time instant t , the first three equations in (4.3) guarantees uniqueness for the exterior Dirichlet Laplace problem in 2D. However, this is not the case in 3D. Consider Γ to be a sphere centered at the origin. Then any linear combination of 1 and $\frac{1}{r}$ is a solution to the exterior Dirichlet problem even if we impose $\sup_{\mathbf{x} \in \Omega} |u(\mathbf{x}, t)| < \infty$. The intrinsic difference in two dimensions is that its log-type fundamental solution explodes at infinity, whereas the fundamental solution in other dimension goes to zero.

The solution is unique in \mathbb{R}^3 once we specify the constant $u_\infty = \lim_{|x| \rightarrow \infty} u(x) = C$ to complete the generalized Dirichlet condition, which is the original model in the paper of Mullins and Sekerka [Mullins & Sekerka (1963)]. This represents an undercooling or an overheating environment that enacts the solidification or liquidation. Under this condition, they show that there is no equilibrium state other than one value of u_∞ if we choose $\Omega = \mathbb{R}^3$ as discussed in [Pego (1989)]. This can be understood as the crystal can only either grow and keep growing if the environment has temperature below melting point, or can only melt and completely liquidate if the environment has temperature above melting point. Moreover, their paper proves that, if a sphere is slightly perturbed in the angle $\Gamma = R + \delta Y_{ml}(\theta, \phi)$, then the solidification of the shape is unstable ($\frac{d\delta}{dt} > 0$) after a threshold of the crystal size $R > R_{thr}$. This instability is

present for any $\Omega \subset \mathbb{R}^3$

The last condition is not in the model. It is implied in 2D from the boundedness of u (the compatibility condition). This is the result of the log-type fundamental solution, as we summarized in Lemma 1. Note that the above argument will not work for higher dimensions because the fundamental solutions are not unbounded at infinity. This compatibility condition is the reason why Mullins-Sekerka flows in 2D are automatically mass preserving, while their dynamics in three dimensions are dependent on the environment u_∞ , as shown in the next section.

There have been existing work on MS-flows in 2D [Zhu *et al.* (1996)] and 3D [Karali & Kevrekidis (2009)] using explicit boundary integral methods and using level set framework with a finite difference scheme [Chen *et al.* (1997)]. In this chapter, we will give an implicit boundary integral method that can deal with far components with topological changes.

4.2 Some Analytic Properties

We can deduce some geometric properties of the dynamics with a direct computation. Let A denote the mass (volume), and L denote the perimeter, we first have the interface dynamics being curve shortening, as also evidenced by our numerical experiment in Figure 4.1:

$$\begin{aligned} \frac{d}{dt}L(t) &= - \int_{\Gamma_t} \kappa V = - \int_{\Gamma_t} u \left[\frac{\partial u}{\partial n} \right] \\ &= - \int_{\mathbb{R}^m \setminus \bar{\Omega}_t} |\nabla u|^2 \leq 0. \end{aligned} \tag{4.4}$$

As for the mass (volume), we have (also numerically illustrated in Figure 4.1)

$$\begin{aligned} \frac{d}{dt}A(t) &= - \int_{\Gamma_t} V = - \int_{\Gamma_t} [\partial_n u] \\ &= \lim_{r \rightarrow \infty} \int_{\partial C_r} [\partial_n u] - \lim_{r \rightarrow \infty} \int_{C_r \setminus \bar{\Omega}_t} \Delta u \\ &= \lim_{r \rightarrow \infty} \int_{\partial C_r} [\partial_n u]. \end{aligned}$$

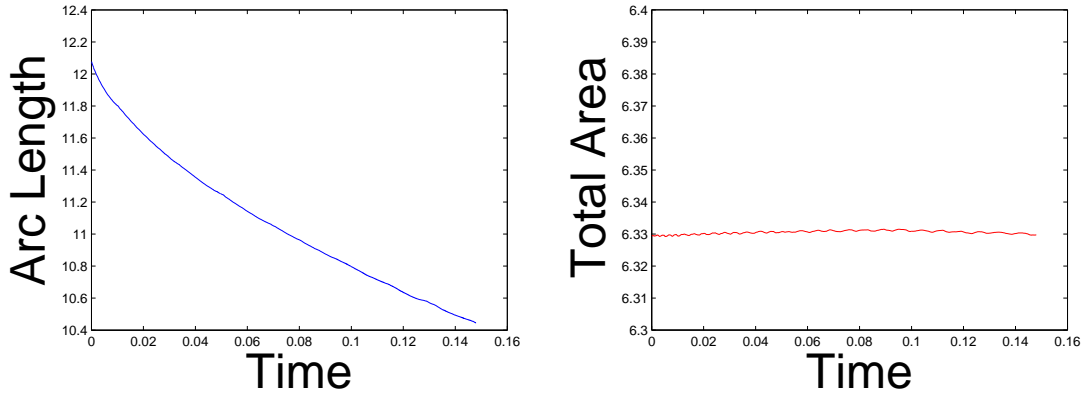


Figure 4.1: The evolution of perimeter and mass (area) of an ellipse in Mullins-Sekerka model.

For two dimensions, the compatibility condition implies the flux is zero. Therefore, the dynamics is mass preserving in $2D$. Furthermore by the curve shortening property, the only equilibria are one circle (stable) and multiple same size circles (unstable). For three dimensions, if the environment has zero heat flux, for example, an adiabatic process in a container with boundary ∂C , then $\int_{\partial C} [\partial_n u] = 0$ implies that the dynamics is mass preserving. However, if we only specify the temperature u_∞ in the environment, then in general this isothermal process is not mass preserving. Depending on whether the environment's temperature is higher than the phase point, one of the phase will have volume gain. The only isothermal process that is also mass preserving is when the environment temperature is exactly at the phase point. We note that this equilibrium is unstable.

It is worth noting that although the motion is curve shortening and its equilibria consists of collections of equal sized circles in $2D$, the process does not necessarily preserve convexity at all times as shown in [Mayer (1993)]. In the following simulation of we will also illustrate this phenomenon when the shape is a long tube. This also shows that there exists a continuous, curve shortening (and even mass preserving) transformation between two convex shapes that passes through non-convex shapes.

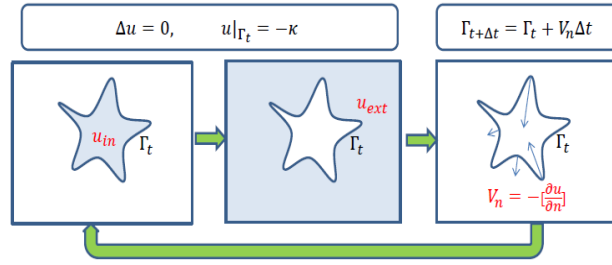


Figure 4.2: Procedure diagram for Mullins-Sekerka simulation.

4.3 Algorithm Details

To simulate the dynamics described in (4.3), the problem can be summarized into five steps

1. Re-initialize level set function $\phi_t(x)$ to the signed distance function $d_{\Gamma_t}(x)$.
2. Extract information for step 3 with connected component labeling (CCL).
3. Solve u on Ω_t and $\mathbb{R}^m \setminus \bar{\Omega}_t$ from the first three equations in (4.3).
4. Obtain and extend the normal velocity $[\partial_n u]$.
5. Move Γ_t with the normal velocity V as in (4.3). We then have a new interface $\Gamma_{t+\delta t}$

We begin with the level set describing Γ_0 , and follow the above steps iteratively. Below is how we simulate with a full Eulerian approach in detail. The procedure diagram is illustrated as in Figure 4.2

4.3.1 Standard Level Set Redistancing

As discussed in Subsection 3.2.2, we begin with a \mathcal{C}^2 , compact hypersurface in \mathbb{R}^m with a chosen orientation and non-zero reach. Then \mathbb{R}^m can be partitioned into the disjoint union $\Omega^- \cup \Gamma \cup \Omega^+$, where $\partial\Omega^- = \partial\Omega^+ = \Gamma$

Let $\phi_0(x)$ be a level set function with $\phi_0(x) < 0$ for $x \in \Omega^+$ and $\phi_0(x) > 0$ for $x \in \Omega^-$. Standard distance re-initialization propagates the PDE

$$\psi_t + \frac{\psi_0}{\sqrt{\psi_0^2 + \varepsilon^2}} (|\nabla \psi| - 1) = 0, \quad (4.5)$$

to a steady state with initial condition $\psi(x, 0) = \phi_0(x)$. The steady state of this eikonal equation preserves the level set $\Gamma := x : \phi_0(x) = 0$ and has gradient of unit norm, which yields the signed distance function, and can be used in IBIM for solving Dirichlet Laplace problem in the following steps.

4.3.2 Connected Component Labeling

Connected component labeling (CCL) [[Rosenfeld & Pfaltz \(1966\)](#); [Samet & Tamminen \(1988\)](#); [Dillencourt *et al.* \(1992\)](#); [Di Stefano & Bulgarelli \(1999\)](#)] is an algorithm in computer graphics to extract and label the connected regions given a binary graph. This algorithm provides separation and labeling of each connected component (See Appendix C). Since we deal with closed interfaces, every grid point belongs to a unique component and has a well defined component label. For each connected component C_i (C_i may be part of Ω or $\mathbb{R}^m \setminus \bar{\Omega}$), however, a boundary integral formulation solving interior Dirichlet Laplace problems in multiply connected region (in 2D, for instance)

$$\begin{cases} \int_{\Gamma^i} \left(\frac{\partial \Phi(\mathbf{x}, \mathbf{y})}{\partial \mathbf{n}_y} - 1 \right) \beta(\mathbf{y}) dS(\mathbf{y}) - \frac{1}{2} \beta(\mathbf{x}) + \sum_{j=1}^L A_j \Phi(\mathbf{x} - \mathbf{z}_j) = f(\mathbf{x}), \\ \sum_{j=1}^L A_j = 0, \\ \int_{\Gamma_j^i} \beta(\mathbf{y}) dS(\mathbf{y}) = 0, \quad j = 1 \dots L-1, \end{cases} \quad (4.6)$$

or other formulations on exterior regions as described in (2.23)(2.24)(2.25)(2.26) require a customization of the CCL algorithm to obtain some key information. Take (4.6) for example,

additional desired information for each component includes:

1. The boundedness of the component region C_i . This decides which formulation (interior or exterior) to use.
2. The orientation of region C_i . This determines the normal direction \mathbf{n}_y . Notice that this is not the same as its boundedness, as the topology of the region can be very convolved.
3. The total number of connected **boundary** components of the boundary Γ^i , which gives L .
4. The separation of Γ^i into boundary components Γ_j^i , each bounding a *hole* in the region except for the most exterior one. We denote this boundary Γ_0^i . The identification of this boundary is important, as it will not be part of the third equation in (4.6) as the other boundary pieces.
5. For each hole (circled by Γ_j^i , $j \neq 0$), find a point \mathbf{z}_i inside the hole ($\mathbf{z}_i \notin \Omega_i$) that gives the least singular value of $\Phi(\mathbf{x}) - \mathbf{z}_i$. This means that \mathbf{z}_i should be as far from the interface as possible.

Our labeling guidelines are described below.

1. For the environment (unbounded) component, we label it as C_0 . This is the only “true exterior” component regarded in terms of the BIM formulation.
2. Each interior component ($d_\Gamma > 0$) will have positive label C_i . Each exterior component ($d_\Gamma < 0$) takes negative label C_{-i} (except for the unbounded component).
3. Each boundary piece of each component will have label Γ_j^i . In the program, we will assign the label j as the component label it is adjacent to, meaning that it can take negative values. Naturally, $\Gamma_j^i = \Gamma_i^j$. In the figures, however, we will take a direct numbering of the boundary pieces.

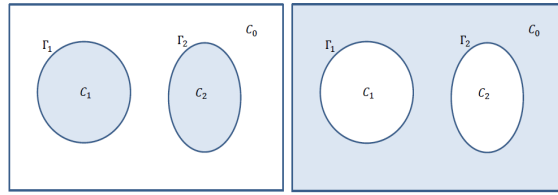


Figure 4.3: The labeling of interior and exterior of two simply-connected components.

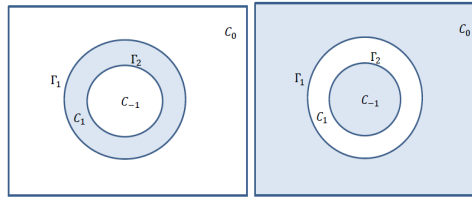


Figure 4.4: The labeling of interior and exterior of an annulus.

4. With the signed distance available, we will record \mathbf{z}_i in C_i as the point with furthest absolute distance to the boundary.

We show configurations of two simply connected regions (Figure 4.3), annulus (Figure 4.4), and multi-layered annulus (Figure 4.5) to illustrate our labeling schemes.

We adopt the two-pass CCL algorithm with $2m$ -connectivity in \mathbb{R}^m . That is, we do not consider diagonal points with the same level set signage to be connected. For simplicity, we will refer to the signage of the signed distance function at the point as “*the sign of the point*”. We keep track of *equivalent classes* for components that are connected but are not assigned the same label at its first pass. The *root* of the equivalent class denote the smallest label (in absolute value) in the equivalent class. The scanning process works as follows.

1. On the first pass:

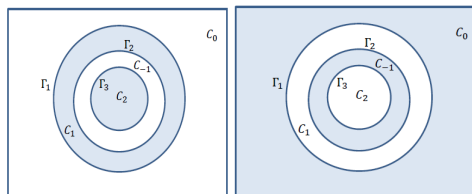


Figure 4.5: The labeling of interior and exterior of a multi-layer annulus.

- (a) We begin with label 0, denoting the environment component C_0 . This is the only unbounded component.
- (b) For each point being scanned, we look at the signed distance of the points already traveled (to the left and to the top, and to the near in $3D$).
 - i. If there is no points with the same sign, we assign a new label (positive or negative) based on its sign and create a new equivalent class. We increment the respective signed label counter by one.
 - ii. If there exists only one neighbor point with the same sign, we assign the label to be the root of that neighboring point's equivalence class. Points within the same equivalence class are connected but not yet assigned the correct label due to a no look-back scanning.
 - iii. If there exists more than one neighbor point with the same sign, we assign the label to be the smallest root of all the neighbors' equivalence classes. Furthermore, we combine the equivalence classes of the neighboring points, because they're connected exactly through this current point. This can be done just by updating the root of the merged equivalent classes.
- (c) The largest root (in each sign, as interior and exterior) of all equivalence classes is the total number of connected (interior/exterior) components. The sum is hence the total number of connected components.

2. On the second pass:

- (a) For each point, we assign its (correct) label to be the root of its equivalent class.
- (b) We update and store the points with largest absolute distance within each equivalence class. These are the points furthest away from interface and will be the \mathbf{z}_i s.

- (c) For each point within the ε tubular neighborhood of the boundary ($|d_\Gamma| < \varepsilon$), we observe the root of its equivalence class (say, i) and the root of its projection point's equivalent class (j) that takes the opposite sign. The projection point is easy to find as we have $\mathbf{x}^* = \mathbf{x} - d_\Gamma(\mathbf{x})\nabla d_\Gamma(\mathbf{x})$. We can then look for the vertices of the cell the mirror point falls in and scan for the label with opposite sign. This step identifies the boundary piece Γ_j^i and collects points within the ε neighborhood of the boundary Γ_j^i . The information will be used for implicit integral formulation.
- (d) As in part (c), we keep a counter for each equivalence class and store the total number of connected boundary pieces. This is L in (4.6).

After the processes above, we obtain all the information needed for our IBIM formulation at each time t , which will be described in the next section. To concentrate on the simulation of the MS-flow dynamics, we put numerical results solving a static Dirichlet Laplace problem in Appendix C. This demonstrates the effectiveness of our customized algorithm combining CCL with IBIM in a complicated topological setting. We make some concluding remarks for the benefits of CCL:

1. The method can deal with general domains with only the knowledge of level set values.
2. Using BIM on each component piece by piece lowers computation cost with smaller matrices, as $N^3 \geq \sum_i N_i^3$, for $N = \sum_i N_i$.
3. With similar reasoning in 2, the boundary separation saves memory storage because we only need to invert the matrix from one component at a time.
4. The method is easily parallizable since each component can be solved separately.

4.3.3 IBIM for the General Dirichlet Laplace Problem

As discussed in Section 3.3, from the derivations of [Kublik *et al.* (2013)] we can use a change of variable and averaging theorem to transform the traditional BIM into a level-set based BIM.

We will use the same implicit framework in a more general setting for multiply connected regions as illustrated in (2.23)(2.24)(2.25)(2.26). To form the correct set of equations, we need to use the topological and geometric information obtained from the CCL algorithm described in Subsection 4.3.2. Let $T_\varepsilon = \{x \in \mathbb{R}^m \mid |d_\Gamma(x)| < \varepsilon\}$ be the tubular neighborhood of the interface Γ , we adopt the discretization notations in Section 3.3 and describe the formulations in detail.

4.3.3.1 Interior Component in 2D

For each interior component ($C_n, n \neq 0$), the implicit formulation is

IBIM for the General Interior Dirichlet Laplace Problem in 2D

Let Ω be a region with boundary $\Gamma = \cup_{l=0}^L \Gamma_l$, where each Γ_l is connected and Γ_0 denote the boundary adjacent to the unbounded region. Namely, Ω has L holes, each denoted $\tilde{\Omega}_l$. Denote also T_ε for the ε tubular neighborhood of Γ ($|d_\Gamma| < \varepsilon$) and T_ε^l the ε tubular neighborhood of Γ_l ($= \{|d_{\Gamma_l}| < \varepsilon\}$). Then the Dirichlet Laplace problem can be solved with the following procedure

1. Solve β, A_l ($l = 1 \dots L$) for $\mathbf{x}^* \in \Gamma$ from the following system:

$$\begin{cases} \int_{T_\varepsilon} \frac{\partial \Phi(\mathbf{x}^*, \mathbf{y}^*)}{\partial \mathbf{n}_y} \beta(\mathbf{y}^*) \delta_\varepsilon(d_\Gamma(\mathbf{y})) J(\mathbf{y}) dy + \frac{1}{2} \beta(\mathbf{x}^*) + \sum_{l=1}^L A_l \Phi(\mathbf{x}^* - \mathbf{z}_l) = f(\mathbf{x}^*). \\ \int_{T_\varepsilon^l} \beta(\mathbf{y}^*) \delta_\varepsilon(d_{\Gamma_l}(\mathbf{y})) J(\mathbf{y}) dy = 0, \quad l = 1 \dots L. \end{cases} \quad (4.7)$$

2. The solution for $\mathbf{x} \in \Omega$ is represented by

$$u(\mathbf{x}) = \int_\Gamma \frac{\partial \Phi(\mathbf{x}, \mathbf{y}^*)}{\partial \mathbf{n}_y} \beta(\mathbf{y}^*) \delta_\varepsilon(d_\Gamma(\mathbf{y})) J(\mathbf{y}) dS(\mathbf{y}) + \sum_{l=1}^L A_l \Phi(\mathbf{x} - \mathbf{z}_l), \quad (4.8)$$

where $\mathbf{z}_l \in \tilde{\Omega}_l$ are points within the holes.

Taking the discretization notations as in Subsection 3.3.4, we summarize the algorithm as follows:

IBIM Algorithm for the General Interior Dirichlet Laplace Problem in 2D

For a given boundary integral formulation on a bounded region Ω with \mathcal{C}^2 boundary $\Gamma = \cup_{l=0}^L \Gamma_l$, where each Γ_l is connected and adjacent to the hole $\tilde{\Omega}_l$ and Γ_0 denote the boundary adjacent to the unbounded region. Denote also T_ε for the ε tubular neighborhood of Γ ($|d_\Gamma| < \varepsilon$) and T_ε^l the ε tubular neighborhood of Γ_l ($\{|d_{\Gamma_l}| < \varepsilon\}$).

The algorithm for solving the multiply connected Dirichlet Laplace Problem

$$\begin{cases} \Delta u(\mathbf{x}) = 0 & \mathbf{x} \in \Omega, \\ u(\mathbf{x}) = f(\mathbf{x}), & \mathbf{x} \in \Gamma = \partial\Omega, \end{cases}$$

with implicit boundary integral formulation (IBIM) takes the following steps:

1. Use CCL in Subsection 4.3.2 to obtain L , $\mathbf{x}_i \in T_\varepsilon^l$, $\mathbf{z}_l \in \tilde{\Omega}_l$, and N , the total the number of points in $T_\varepsilon = \cup_{l=1}^L T_\varepsilon^l$.
2. For each $\mathbf{x}_i \in T_\varepsilon$, compute $\mathbf{x}_i^* = \mathbf{x}_i - d_i \nabla_H d_i$.
3. Form the matrix $K = \begin{pmatrix} D + \frac{1}{2}I & E \\ F & G \end{pmatrix}$ of dimension $(N + L) \times (N + L)$ and the vector

$$\tilde{f} = \begin{pmatrix} f^* \\ 0 \end{pmatrix} (N+L) \times 1, \text{ where}$$

$$D_{i,j} = H^2 \delta_j J_j \left(\frac{\partial \Phi}{\partial n_y} \right)_{i,j}^*, \quad 1 \leq i, j \leq N.$$

$$E_{i,j} = \Phi(\mathbf{x}_i^* - \mathbf{z}_j), \quad 1 \leq i \leq N, N+1 \leq j \leq N+L.$$

$$F_{i,j} = \chi_{T_\varepsilon^i}(\mathbf{x}_j^*), \quad 1 \leq j \leq N, N+1 \leq i \leq N+L.$$

$$G_{i,j} = 0, \quad N+1 \leq i, j \leq N+L.$$

$$f_i^* = f(\mathbf{x}_i^*), \quad 1 \leq i \leq N.$$

Here $\chi_{T_\varepsilon^i}$ denotes the indicator function of the tubular neighborhood T_ε^i .

4. Solve the $(N+L) \times 1$ vector $\tilde{\beta}$ from the linear equation $K\tilde{\beta} = \tilde{f}$, where $\tilde{\beta} = \begin{pmatrix} \beta^* \\ A \end{pmatrix}$.

$$\beta^* = \beta(\mathbf{x}^*) \text{ is } N \times 1, A = \begin{pmatrix} A_1 \\ \vdots \\ A_L \end{pmatrix}$$

5. For any $\mathbf{x} \in \Omega$, the solution is evaluated by computing

$$u(x) = \sum_j H^2 \delta_j J_j \left(\frac{\partial \Phi}{\partial n_y} \right)_{x,j} \beta_j^* + \sum_{l=1}^L A_l \Phi(\mathbf{x} - \mathbf{z}_l)$$

4.3.3.2 Exterior Component in 2D

For the unbounded component C_0 , the implicit formulation is

IBIM for the General Exterior Dirichlet Laplace Problem in 2D

Let $C_0 = \mathbb{R}^2 \setminus \bar{\Omega}$ be a region with boundary $\Gamma = \cup_{l=1}^L \Gamma_l$, where each Γ_l is connected and adjacent to the hole denoted $\tilde{\Omega}_l$. Denote also T_ε for the ε tubular neighborhood of Γ ($\{|d_\Gamma| < \varepsilon\}$) and T_ε^l the ε tubular neighborhood of Γ_l ($|d_{\Gamma_l}| < \varepsilon$). Then the exterior Dirichlet Laplace Problem can be solved with the following procedure

1. Solve β, A_l for $\mathbf{x}^* \in \Gamma$ from the following system:

$$\begin{cases} \int_{T_\varepsilon} \left(\frac{\partial \Phi(\mathbf{x}^*, \mathbf{y}^*)}{\partial n_{\mathbf{y}}} - 1 \right) \beta(\mathbf{y}^*) \delta_\varepsilon(d_\Gamma(\mathbf{y})) J(\mathbf{y}) d\mathbf{y} - \frac{1}{2} \beta(\mathbf{x}^*) + \sum_{l=1}^L A_l \ln |\mathbf{x}^* - \mathbf{z}_l| = f(\mathbf{x}^*). \\ \sum_{l=1}^L A_l = 0. \\ \int_{T_\varepsilon^l} \beta(\mathbf{y}^*) \delta_\varepsilon(d_\Gamma(\mathbf{y})) J(\mathbf{y}) d\mathbf{y} = 0 \text{ for } l = 1, \dots, L-1. \end{cases} \quad (4.9)$$

2. The solution u for $\mathbf{x} \in \mathbb{R}^2 \setminus \bar{\Omega}$ can then be computed as

$$u(\mathbf{x}) = \int_{T_\varepsilon} \left(\frac{\partial \Phi(\mathbf{x}, \mathbf{y}^*)}{\partial n_{\mathbf{y}}} - 1 \right) \beta(\mathbf{y}^*) \delta_\varepsilon(d_\Gamma(\mathbf{y})) J(\mathbf{y}) d\mathbf{y} + \sum_{l=1}^L A_l \ln |\mathbf{x} - \mathbf{z}_l|, \quad \mathbf{x} \in \mathbb{R}^2 \setminus \bar{\Omega}, \quad (4.10)$$

where $\mathbf{z}_j \in \Omega_j$ are arbitrary points within the holes.

With the corresponding algorithm:

IBIM Algorithm for the General Exterior Dirichlet Laplace Problem in 2D

For a given boundary integral formulation on an unbounded region $C_0 = \mathbb{R}^2 \setminus \bar{\Omega}$ with \mathcal{C}^2

boundary $\Gamma = \cup_{l=1}^L \Gamma_l$, where each Γ_l is connected and adjacent to the hole $\tilde{\Omega}_l$. Denote also T_ε for the ε tubular neighborhood of Γ ($|d_\Gamma| < \varepsilon$) and T_ε^l the ε tubular neighborhood of Γ_l ($\{|d_{\Gamma_l}| < \varepsilon\}$).

The algorithm for solving the multiply connected Dirichlet Laplace Problem

$$\begin{cases} \Delta u(\mathbf{x}) = 0, & \mathbf{x} \in \mathbb{R}^2 \setminus \tilde{\Omega} \\ u(\mathbf{x}) = f(\mathbf{x}), & \mathbf{x} \in \Gamma = \partial\Omega \end{cases}$$

with implicit boundary integral formulation (IBIM) takes the following steps:

1. Use CCL in Subsection 4.3.2 to obtain L , $\mathbf{x}_i \in T_\varepsilon^l$, $\mathbf{z}_l \in \tilde{\Omega}_l$, and N , the total the number of points in $T_\varepsilon = \cup_{l=1}^L T_\varepsilon^l$.

2. For each $\mathbf{x}_i \in T_\varepsilon$, compute $\mathbf{x}_i^* = \mathbf{x}_i - d_i \nabla_H d_i$.

3. Form the matrix $K = \begin{pmatrix} D - \frac{1}{2}I & E \\ F & G \\ 0 & 1, 1, \dots, 1 \end{pmatrix}$ of dimension $(N+L) \times (N+L)$ and the

vector $\tilde{f} = \begin{pmatrix} f^* \\ 0 \end{pmatrix}$ $(N+L) \times 1$, where

$$D_{i,j} = H^2 \delta_j J_j \left(\left(\frac{\partial \Phi}{\partial n_y} \right)_{i,j}^* - 1 \right), \quad 1 \leq i, j \leq N.$$

$$E_{i,j} = \Phi(\mathbf{x}_i^* - \mathbf{z}_j), \quad 1 \leq i \leq N, N+1 \leq j \leq N+L.$$

$$F_{i,j} = \chi_{T_\varepsilon^i}(\mathbf{x}_j^*), \quad 1 \leq j \leq N, N+1 \leq i \leq N+L-1.$$

$$G_{i,j} = 0, \quad N+1 \leq i \leq N+L-1, N+1 \leq j \leq N+L.$$

$$f_i^* = f(\mathbf{x}_i^*), \quad 1 \leq i \leq N.$$

Here $\chi_{T_\varepsilon^i}$ denotes the indicator function of the tubular neighborhood T_ε^i .

4. Solve the $(N + L) \times 1$ vector $\tilde{\beta}$ from the linear equation $K\tilde{\beta} = \tilde{f}$, where $\tilde{\beta} = \begin{pmatrix} \beta^* \\ A \end{pmatrix}$.

$$\beta^* = \beta(\mathbf{x}^*) \text{ is } N \times 1, A = \begin{pmatrix} A_1 \\ \vdots \\ A_L \end{pmatrix}.$$

5. For any $\mathbf{x} \in \Omega$, the solution is evaluated by computing

$$u(x) = \sum_j H^2 \delta_j J_j \left(\frac{\partial \Phi}{\partial n_y} \right)_{x,j} \beta_j^* + \sum_{l=1}^L A_l \Phi(\mathbf{x} - \mathbf{z}_l).$$

4.3.3.3 Components in 3D

For three dimensions, the interior and exterior formulations only differ in the presence of the far field term u_∞ . We can collect the formulations together:

IBIM for the General Dirichlet Laplace Problem in 3D

Let $\Omega \subset \mathbb{R}^3$ be a region with boundary $\Gamma = \cup_{l=0}^L \Gamma_l$ ($\Gamma = \cup_{l=1}^L \Gamma_l$ if Ω is unbounded), where each Γ_l is connected and Γ_0 denote the boundary adjacent to the unbounded region. Namely, Ω has L holes, each denoted $\tilde{\Omega}_l$. Denote also T_ε for the ε tubular neighborhood of Γ ($\{|d_\Gamma| < \varepsilon\}$) and T_ε^l the ε tubular neighborhood of Γ_l ($\{|d_{\Gamma_l}| < \varepsilon\}$). Then the Dirichlet Laplace Problem can be solved with the following procedure:

1. Solve β, A_l ($l = 1 \dots L$) for $\mathbf{x}^* \in \Gamma$ from the following system:

$$\begin{cases} \int_{T_\varepsilon} \left(\frac{\partial \Phi(\mathbf{x}^*, \mathbf{y}^*)}{\partial \mathbf{n}_\mathbf{y}} - \frac{1}{|\mathbf{x}^* - \mathbf{y}^*|} \right) \beta(\mathbf{y}^*) \delta_\varepsilon(d_\Gamma(\mathbf{y})) J(\mathbf{y}) d\mathbf{y} \pm \frac{1}{2} \beta(\mathbf{x}^*) + \sum_{l=1}^L A_l \Phi(\mathbf{x}^* - \mathbf{z}_l). \\ = f(\mathbf{x}^*) (-u_\infty). \\ \int_{\Gamma_l} \beta(\mathbf{y}^*) \delta_\varepsilon(d_\Gamma(\mathbf{y})) J(\mathbf{y}) dS(\mathbf{y}) = 0, \quad l = 1 \dots L. \end{cases} \quad (4.11)$$

2. The solution for $x \in \Omega$ is represented by

$$u(\mathbf{x}) = \int_\Gamma \left(\frac{\partial \Phi(\mathbf{x}, \mathbf{y}^*)}{\partial \mathbf{n}_\mathbf{y}} - \frac{1}{|\mathbf{x} - \mathbf{y}^*|} \right) \beta(\mathbf{y}^*) d\mathbf{y} + \sum_{l=1}^L A_l \Phi(\mathbf{x} - \mathbf{z}_l) (+u_\infty), \quad (4.12)$$

where $\mathbf{z}_l \in \Omega_l$ are arbitrary points within the holes. If Ω is an interior region, then $u_\infty = 0$.

The respective discretization and algorithm for 3D Laplace equation is:

IBIM Algorithm for the General Dirichlet Laplace Problem in 3D:

For a given boundary integral formulation on a bounded region Ω with \mathcal{C}^2 boundary $\Gamma = \cup_{l=0}^L \Gamma_l$ ($\Gamma = \cup_{l=1}^L \Gamma_l$ if Ω is unbounded), where each Γ_l is connected and adjacent to the hole $\tilde{\Omega}_l$ and Γ_0 denote the boundary adjacent to the unbounded region. Denote also T_ε for the ε tubular neighborhood of Γ ($\{|d_\Gamma| < \varepsilon\}$) and T_ε^l the ε tubular neighborhood of Γ_l ($\{|d_{\Gamma_l}| < \varepsilon\}$).

The algorithm for solving the 3D multiply connected Dirichlet Laplace Problem

$$\begin{cases} \Delta u(\mathbf{x}) = 0, & \mathbf{x} \in \Omega, \\ u(\mathbf{x}) = f(\mathbf{x}), & \mathbf{x} \in \Gamma = \partial\Omega, \\ \left(\lim_{|\mathbf{x}| \rightarrow \infty} u(\mathbf{x}) = u_\infty, \quad \text{if } \mu(\Omega) = \infty, \right) \end{cases}$$

with implicit boundary integral formulation (IBIM) takes the following steps:

1. Use CCL in Subsection 4.3.2 to obtain L , $\mathbf{x}_i \in T_\varepsilon^l$, $\mathbf{z}_l \in \tilde{\Omega}_l$, and N , the total the number of points in $T_\varepsilon = \cup_{l=1}^L T_\varepsilon^l$.

2. For each $\mathbf{x}_i \in T_\varepsilon$, compute $\mathbf{x}_i^* = \mathbf{x}_i - d_i \nabla_H d_i$.

3. Form the matrix $K = \begin{pmatrix} D \pm \frac{1}{2}I & E \\ F & G \end{pmatrix}$ of dimension $(N+L) \times (N+L)$ and the vector

$$\tilde{f} = \begin{pmatrix} f^* \\ 0 \end{pmatrix} (N+L) \times 1, \text{ where}$$

$$D_{i,j} = H^2 \delta_{ij} J_j \left(\left(\frac{\partial \Phi}{\partial n_y} \right)_{i,j}^* - \frac{1}{|\mathbf{x}_i^* - \mathbf{x}_j^*|} \right), \quad 1 \leq i, j \leq N.$$

$$E_{i,j} = \Phi(\mathbf{x}_i^* - \mathbf{z}_j), \quad 1 \leq i \leq N, N+1 \leq j \leq N+L.$$

$$F_{i,j} = \chi_{T_\varepsilon^i}(\mathbf{x}_j^*), \quad 1 \leq j \leq N, N+1 \leq i \leq N+L.$$

$$G_{i,j} = 0, \quad N+1 \leq i, j \leq N+L.$$

$$f_i^* = f(\mathbf{x}_i^*) (-u_\infty), \quad 1 \leq i \leq N.$$

Here $\chi_{T_\varepsilon^i}$ denotes the indicator function of the tubular neighborhood T_ε^i . $u_\infty = 0$ for interior region.

4. Solve the $(N+L) \times 1$ vector $\tilde{\beta}$ from the linear equation $K\tilde{\beta} = \tilde{f}$, where $\tilde{\beta} = \begin{pmatrix} \beta^* \\ A \end{pmatrix}$.

$$\beta^* = \beta(\mathbf{x}^*) \text{ is } N \times 1, A = \begin{pmatrix} A_1 \\ \vdots \\ A_L \end{pmatrix}.$$

5. For any $\mathbf{x} \in \Omega$, the solution is evaluated by computing

$$u(x) = \sum_j H^2 \delta_j J_j \left(\frac{\partial \Phi}{\partial n_y} \right)_{x,j} \beta_j^* + \sum_{l=1}^L A_l \Phi(\mathbf{x} - \mathbf{z}_l) \left(+ u_\infty \right).$$

4.3.4 Velocity Extension

Given $V_n = [\frac{\partial u}{\partial n}]_{\Gamma_t}$ from the solution of the PDE, the next stage of the simulation is to extend the normal velocity to neighboring grid points to prepare for a stable interface propagation. Following the discussions in Section 3.2, the idea is to define the velocity field in the space such that it converges continuously to the prescribed velocity on the interface

$$\lim_{\mathbf{x} \rightarrow \mathbf{x}^*} V_n(\mathbf{x}) = V_n(\mathbf{x}^*), \quad \mathbf{x}^* \in \Gamma. \quad (4.13)$$

We propagate the following hyperbolic equation, whose characteristics point outward from the interface to the whole domain, and thus floods the velocity profile satisfying $\nabla \phi \cdot \nabla V_n = 0$ from the interface and out:

$$\frac{\partial V_n}{\partial t} + \text{sgn}(\phi) \frac{\nabla \phi}{|\nabla \phi|} \cdot \nabla V_n = 0 \quad (4.14)$$

In some front propagation problems such as the mean curvature flows, the normal velocity V_n is readily known and conveniently computed for each point $\mathbf{x}^* \in \Gamma$ (for example, $\kappa(\mathbf{x}^*) = \nabla \cdot \frac{\nabla \phi}{|\nabla \phi|}$). Therefore, constant velocity extension is commonly used. However, in the case of Mullins-Sekerka flows, the velocity on the boundary requires an evaluation of

$$\frac{\partial u}{\partial n_{\mathbf{x}}}(\mathbf{x}^*) = \int_{\Gamma} \frac{\partial^2 \Phi}{\partial n_x \partial n_y}(\mathbf{x}^*, \mathbf{y}) \beta(\mathbf{y}) dS(\mathbf{y}).$$

The extra normal derivative on the kernel makes the solution evaluation a hypersingular boundary integral. To circumvent this challenge, we note that the velocity extension flow only requires a continuous extension and not a constant extension. For a locally \mathcal{C}^2 boundary, define the general velocity field within the tubular neighborhood T_ε as the difference of the Neumann data of itself and its mirror point from the interface:

$$V_n(\mathbf{x}) := \text{sgn}(d_\Gamma(\mathbf{x})) \left(\frac{\partial u}{\partial n}(\mathbf{x}) - \frac{\partial u}{\partial n}(\mathbf{x} - 2d_\Gamma(\mathbf{x})\nabla d_\Gamma(\mathbf{x})) \right), \quad \mathbf{x} \notin \Gamma, \mathbf{x} \in T_\varepsilon. \quad (4.15)$$

The signum function is applied to be consistent with the sign of Mullins-Sekerka model. The point $\mathbf{x} - 2d_\Gamma(\mathbf{x})\nabla d_\Gamma(\mathbf{x})$ is the mirror point of \mathbf{x} . It is easily seen that the definition (4.15) satisfies the continuity criterion (4.13). The kernels are now non-singular since the evaluation points are off boundary.

For points that are further away from the boundary (e.g. not inside the tubular neighborhood T_ε), the mirror point may not be a good choice as it may be projected over the interface again into an unwanted region or across the kinks of the level set function. Therefore, we need to apply the standard velocity extension algorithm (4.14) for points outside the tubular neighborhood. In this case, an upwind Godunov scheme is used. The spatial derivative uses a WENO-3 scheme. For time propagation, we use an implicit third order TVD-RK3 method as in (3.3) with a CFL coefficient $c = 1$. We propagate a number of steps to ensure the velocity information is transmitted throughout a ε neighborhood band of $\Gamma_t = \partial\Omega_t$.

4.3.5 Interface Propagation

Once we have the normal velocity profile, we propagate the interface by with the standard level set method [Osher & Fedkiw (2000)]. Consider the motion of some level set $\phi(\mathbf{x}, t) = C$. By the chain rule we have

$$\phi_t + \nabla\phi \cdot \frac{\partial \mathbf{x}}{\partial t} = 0. \quad (4.16)$$

Since we also have $\mathbf{n} = \frac{\nabla\phi}{|\nabla\phi|}$ for the exterior normal vector \mathbf{n} , replacing $\nabla\phi$ in (4.16),

$$\phi_t + |\nabla\phi| \frac{\partial \mathbf{x}}{\partial t} \cdot \mathbf{n} = 0.$$

But $\frac{\partial \mathbf{x}}{\partial t} \cdot \mathbf{n}$ is precisely the normal velocity V_n if we take the positive velocity to simulate shrinking motion. Hence we finally arrive at the interface propagation hyperbolic advection equation:

$$\begin{cases} \phi_t + V_n |\nabla\phi| = 0. \\ \phi(\mathbf{x}, s) = d(\mathbf{x}, \Gamma_s). \end{cases} \quad (4.17)$$

We then use upwind finite difference scheme with WENO-3 spatial derivatives and implicit TVD-RK3 method (3.3) with CFL condition $\Delta t < \frac{1}{\max_{\mathbf{x} \in T_{s,\varepsilon}} |V_n|} \Delta x$ to obtain $\phi_{s+\Delta t}$ (and consequently, $\Gamma_{s+\Delta t}$ as its zero level set). We use $T_{s,\varepsilon}$ again to denote the tubular neighborhood of the interface Γ_s (at time s) within distance ε .

4.4 Numerical Results in 2D

We begin with two simple simulations of a circle and an ellipse with their shape evolution (Figure 4.6) to illustrate the dynamics to equilibrium state. Next we illustrate the propagation is successful with interfaces with sharp corners (e.g. Figure 4.7). We then test on long tubes (See Figure 4.9) and observe the motion does not necessarily preserve convexity, as illustrated in [Mayer (1993)]. The last few plots show that the simulation is able to deal with topological changes with arbitrary shapes (Figure 4.8), including shape merging (Figure 4.10).

4.4.1 Equilibrium State

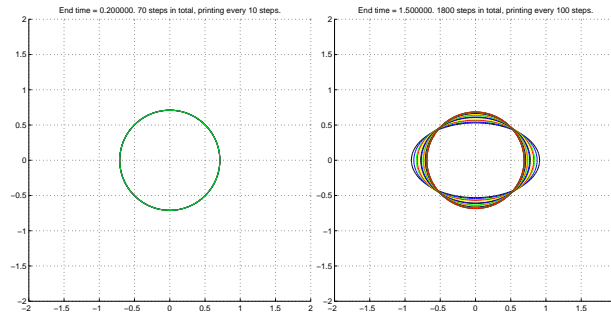


Figure 4.6: Interface evolution for circle and ellipse. This is an illustration of the equilibrium state.

4.4.2 Irregular Shapes and Curve Coarsening

We illustrate dynamics of a shape with sharp corners in Figure 4.7. The coarsening process with irregular shapes is demonstrated in Figure 4.8. We see that the shapes converge to a circle, with the largest component absorbing the mass of the other components.

4.4.3 Non-conservation of Convexity

As discussed in [Mayer (1993)], the convexity is not necessarily preserved during the whole process of Mullins-Sekerka flow. We demonstrate our simulation in Figure 4.9.

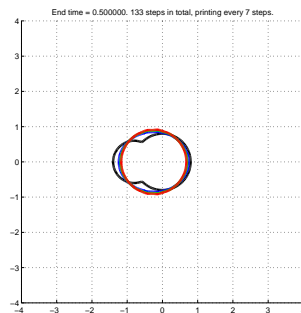


Figure 4.7: Simulation of an interface with sharp corners.

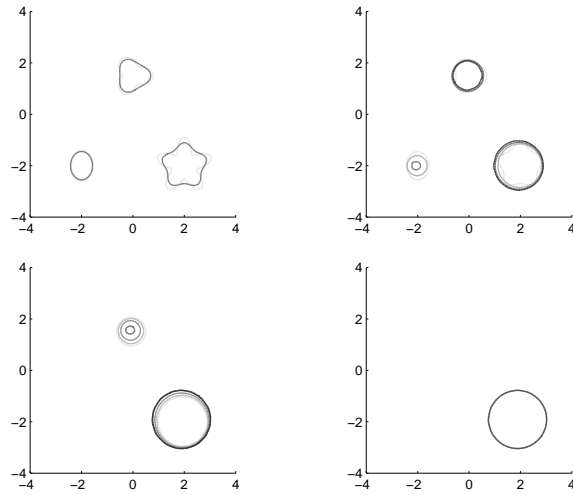


Figure 4.8: The coarsening dynamics of multiple components with irregular shapes.

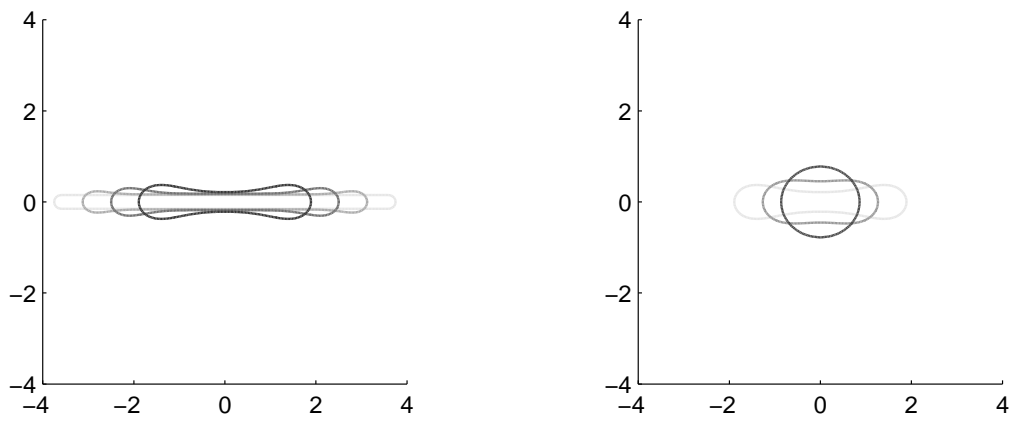


Figure 4.9: Dynamics of long tube.

4.4.4 Shape Merging

The capability of dealing with topological changes is a main advantage of level set methods. Below we illustrate a shape merging simulation in Mullins-Sekerka flow (Figure 4.10). By testing on different grid resolutions (See Table 4.1), we see that the algorithm has convergent error results in terms of area change and time jump. When merging happens, the boundary begins to have corners and one must be careful about the implicit boundary integral since the ε neighborhood now can overlap regardless of the size of ε . In this case, quadrature points within the tubular neighborhood of both boundaries should be counted twice instead of once. Under the IBIM framework, one can use a mirror point to test if a quadrature point needs to be compensated. The results of this strategy will be reported in a future publication.

Table 4.1: The convergence of merging time and area jump.

H	4/128	4/256	4/512
Start Merge Time Stamp	0.009357	0.014789	0.02179
End Merge Time Stamp	0.032062	0.025939	0.026632
Time Jump	0.022762	0.01115	0.004842
Start Merge Area	2.696655	2.691792	2.686751
End Merge Area	2.804205	2.724255	2.694007
Area Jump	0.107550	0.032463	0.007256
Relative Area error	0.03988	0.01206	0.00270
Initial Area	2.6965	2.69611	2.695495

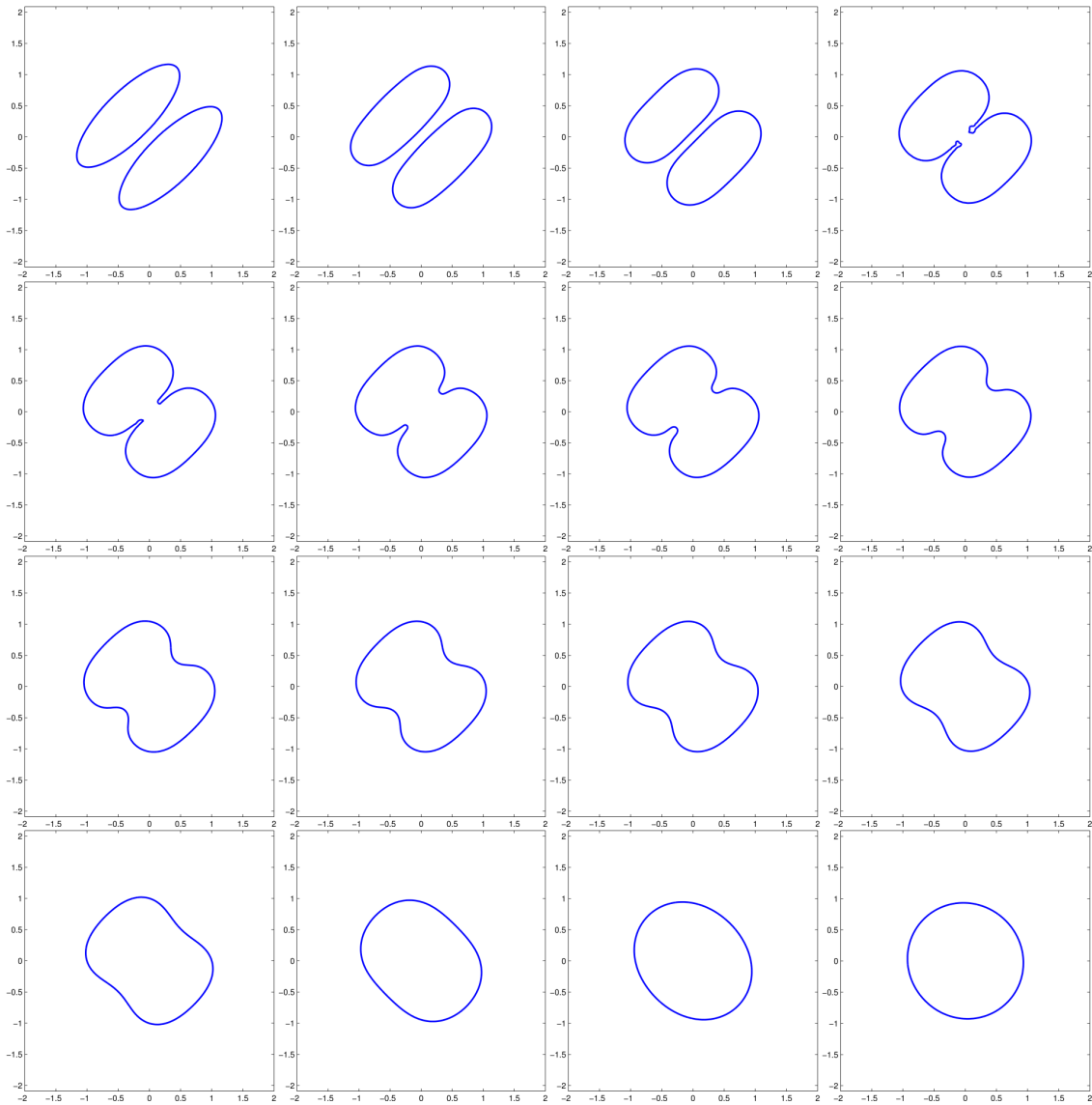


Figure 4.10: Ellipse merging in 2D Mullins-Sekerka flow simulation.

4.5 Numerical Results in 3D

For 3D dynamics, we illustrate two things.

1. The isothermal process depend on the far field environment value (Figure ??).
2. The instability of the general Mullins-Sekerka process.

For the instability, we see that the dendritic growth is isotropic given an radially symmetric initial interface (Figure 4.12). If the crystal has an initial anisotropy, the dendritic growth will magnify the anisotropy. This agrees with the theoretical results and the numerical simulations by [Chen *et al.* (1997)].

4.5.1 Solidification and Liquidation in Various Environments

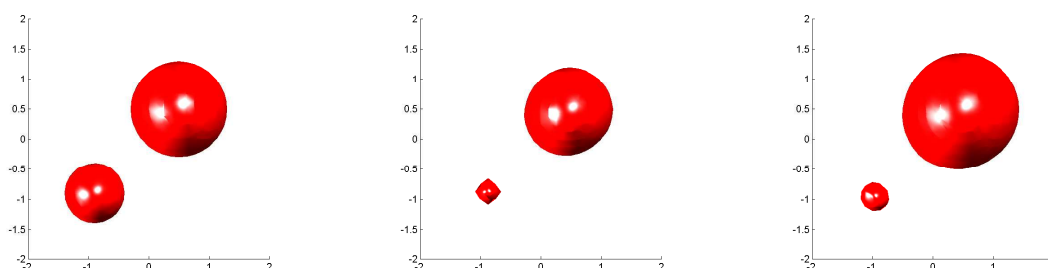


Figure 4.11: On the left, both spheres grow on low temperature. In the middle, both shrinks on high temperature. On the right, the temperature is deliberately set at phase transition point. We see that the larger sphere grows at the expense of the smaller sphere, just as we would observe in the 2D case.

4.5.2 Isotropic and Anisotropic Crystallization

Figure 4.12 shows the instability of dendritic growth. In the last plot (Figure 4.13), we compare crystallization of sphere and a shape with initial anisotropy in coordinate directions. For illustration purpose, we take the xy-slice of the 3D surface. We see that anisotropy will be magnified and muffle the instability.

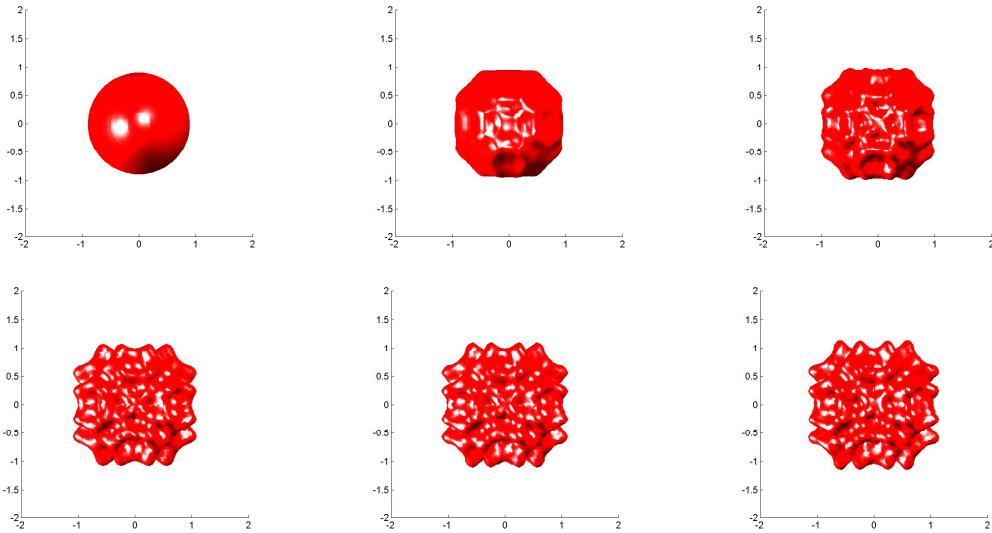


Figure 4.12: Instability of dendritic growth while maintaining crystal symmetry.

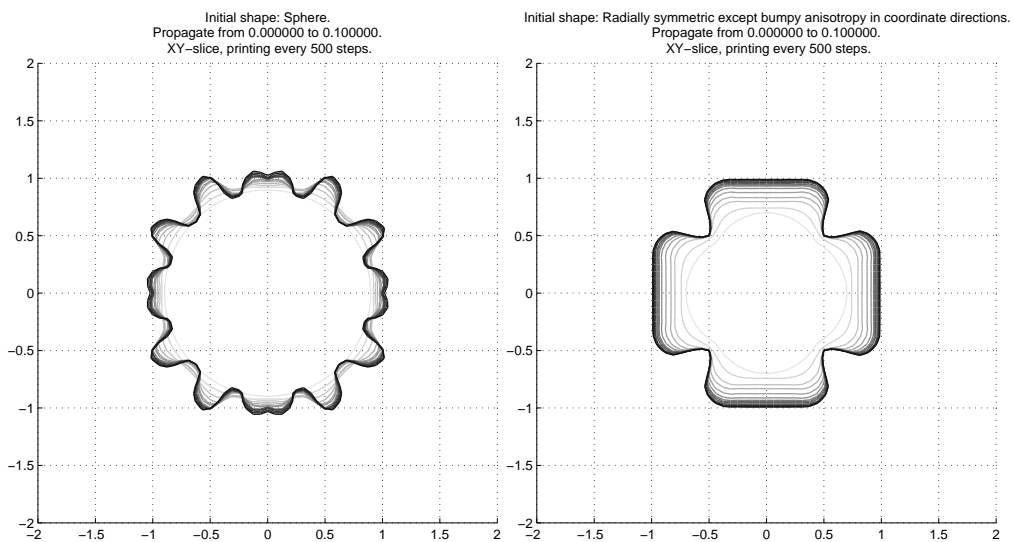


Figure 4.13: Comparison of crystallization with anisotropy.

Chapter 5

Extrapolatory Implicit Boundary Integral Method

5.1 Helmholtz Problem

Wave propagation and scattering has been an active research field with plenty applications including aerospace engineering [[Greenleaf *et al.* \(2008\)](#); [Kohn *et al.* \(2008\)](#)], seismology [[Burrige \(1976\)](#); [Shearer \(2003\)](#)] and medical imaging [[Ammari *et al.* \(2010\)](#)]. When we consider a wave equation in its frequency domain, the time harmonic wave satisfies the Helmholtz equation. In this chapter, we concern ourselves with the exterior Helmholtz problem with Neumann conditions, which represents acoustic wave scattering with a sound-hard obstacle or electromagnetic wave scattering by a perfect conductor. The target problem is described in the following:

Definition 4. Exterior Neumann Helmholtz Problem

Given a closed, compact, \mathcal{C}^2 hyperinterface $\Gamma \in \mathbb{R}^m$, the space is separated into a open, bounded region Ω and its complement $\bar{\Omega}^c = \mathbb{R}^m \setminus \bar{\Omega}$. We seek for a function u satisfying

$$\begin{cases} \Delta u(x) + k^2 u(x) = 0, & x \in \mathbb{R}^m \setminus \bar{\Omega}. \\ \frac{\partial u}{\partial n}(x) = g(x), & x \in \partial\Omega. \\ \lim_{|x| \rightarrow \infty} |x|^{\frac{m-1}{2}} \left(\frac{\partial}{\partial |x|} - ik \right) u(x) = 0. \end{cases} \quad (5.1)$$

$\Omega \in \mathbb{R}^m$ represents the obstacles for scattering. For convenience, we will denote the boundary of the domain $\partial\Omega$ as Γ and use them interchangeably. A detailed discussion on the existence and uniqueness of the solution to (5.1) can be found in [Colton & Kress (2013)].

Numerical studies of the Helmholtz equation include Finite Difference Methods (FDMs) [Singer & Turkel (1998)], Finite Element Methods (FEMs) [Harari & Hughes (1991)], and the boundary integral methods (BIMs) (also called the methods of boundary integral equations [Colton & Kress (2013)]). For a wave scattering problem such as (5.1), FDMs and FEMs can be inconvenient for two main reasons. First, the computation domain is the same as the domain of interest, which is potentially unbounded. Second, artificial boundary conditions need to be imposed to accommodate the Sommerfeld radiation condition at infinity. Boundary integral methods (BIMs) deals with these two challenges naturally. The computation domain is restricted to the boundary, and the integral formulations produce solutions that satisfy the boundary condition at infinity automatically. These advantages keep numerical algorithms based on BIMs [Kress (1991); Canino *et al.* (1998); Schneider (2003)] an active research field for wave scattering.

The BIMs make use of fundamental solutions as discussed in Chapter 2. The fundamental solution Φ for the Helmholtz operator satisfies

$$(\Delta_y + k^2)\Phi(x, y) = \delta(x - y).$$

One can obtain the analytic form of Φ with the Fourier transform. In particular,

$$\Phi(x, y) = \begin{cases} -\frac{i}{4}H_0^{(1)}(k|x-y|) & , \mathbf{x}, \mathbf{y} \in \mathbb{R}^2. \\ \frac{e^{ik|x-y|}}{|x-y|} & , \mathbf{x}, \mathbf{y} \in \mathbb{R}^3. \end{cases}$$

Following similar arguments as in Chapter 2, the traditional boundary integral formulation expresses the solution as an integral:

$$u(x) = \int_{\Gamma} \Phi(x, y) \alpha(y) dy(s) \quad x \in \bar{\Omega}^c. \quad (5.2)$$

Using the jump relation Lemma 3, the potential density α is obtained by solving the following Fredholm's integral equation of the second kind with Neumann boundary conditions.

$$g(x) = \frac{\partial u}{\partial n}(x) = \int_{\Gamma} \frac{\partial \Phi}{\partial n_x}(x, y) \alpha(y) dy(s) - \frac{1}{2} \alpha(x) \quad x \in \partial\Omega. \quad (5.3)$$

However, it is well known [Smirnov (1964)] and established [Kleinman & Roach (1974)] that (5.3) is not uniquely solvable for some wave number k because the integral operator has nontrivial null space. More importantly, the spectrum of the integral operator depends on the domain Ω and is generally infinite dimensional. This means one cannot simply include a finite linear combination of functions to rectify the kernel and cover the whole null space, as in the Laplace problems in Section 2.2¹. Although the spectrum has no accumulation point, the integral equation (5.3) is difficult to solve numerically when k is only close to the eigenvalues [Brundrit (1965); Copley (1968)]. The eigenvalues greatly limits the generality of the traditional boundary integral formulation, particularly for some inverse problems. This problem of operator eigenfrequency exists for both Dirichlet and Neumann boundary conditions.

[Brakhage & Werner (1965); Panich (1965)] showed that a formulation combining both

¹Note however, that the PDE itself is uniquely solvable, just the integral formulation is not sufficient to yield the unique solution.

single and double layer potentials can cover the null space of each other and solve the problem for Dirichlet boundary conditions. The analogous formulation for the Neumann problem is proved effective by [Burton & Miller (1971)], which we summarized as follows:

$$u(x) = \int_{\Gamma} \frac{\partial \phi}{\partial n_y}(x, y) \beta(y) dy(s) - i\xi \int_{\Gamma} \phi(x, y) \beta(y) dy(s) \quad x \in \bar{\Omega}^c, \quad (5.4)$$

and the density β is obtained by solving the resulting Fredholm's equation of the second kind:

$$g(x) = \frac{\partial u}{\partial n}(x) = \frac{\partial}{\partial n_x} \int_{\Gamma} \frac{\partial \phi}{\partial n_y}(x, y) \beta(y) dy(s) - i\xi \left(\int_{\Gamma} \frac{\partial \phi}{\partial n_x}(x, y) \beta(y) dy(s) - \frac{1}{2} \beta(x) \right) \quad x \in \partial\Omega. \quad (5.5)$$

This is also called the Burton-Miller boundary integral formulation. For numerical schemes to invert the integral equation, the order of integration and differentiation is switched in (5.5) to give

$$g(x) = \int_{\Gamma} \frac{\partial^2 \phi}{\partial n_x \partial n_y}(x, y) \beta(y) dy(s) - i\xi \left(\int_{\Gamma} \frac{\partial \phi}{\partial n_x}(x, y) \beta(y) dy(s) - \frac{1}{2} \beta(x) \right) \quad x \in \partial\Omega. \quad (5.6)$$

The hypersingular integral for $x \in \partial\Omega$ is to be interpreted in the Hadamard's sense. This approach is introduced by [Kutt (1975)]. Notice that since the normal derivative on the boundary is one-sided, which is the reason an integral value in the traditional Riemann sense does not exist in (5.6) and requires a special interpretation. But for $x \notin \partial\Omega$, the derivative in the normal direction exists and the commute of differentiation and integration is justified. We have

$$\frac{\partial u}{\partial n}(x) = \int_{\Gamma} \frac{\partial^2 \phi}{\partial n_x \partial n_y}(x, y) \beta(y) dy(s) - i\xi \int_{\Gamma} \frac{\partial \phi}{\partial n_x}(x, y) \beta(y) dy(s), \quad \mathbf{x} \notin \partial\Omega$$

which can be naturally interpreted in the Riemann sense.

As we can see, the difficulty with solving (5.6) is that the double layer potential has become a hypersingular integral. This problem is unique for the Neumann problems (and not for

Dirichlet problems) because of the extra derivative we need to take on the boundary. Regularization methods have been studied for Nyström methods, which require explicit parametrization of the boundary [Paget (1981); Kress (1995)], or a regularization on boundary element methods [Hackbusch & Sauter (1993); Aimi & Diligenti (2002)], which can be quite complicated for nonlinear elements and the approaches are dimensionally dependent. Some other methods include making use of the regularity of the density function to lower the order of singularity [Frangi (1998); Bruno *et al.* (2012)]. In this chapter, we are going to study the formulation using an implicit boundary integral method, which deal with its natural integral formulation (5.5). The method is intuitive to implement on uniform or adaptive Cartesian grids, requires no extra complications in different dimensions, and can deal with different irregular shapes with the boundary described only by its signed distance function.

5.2 Extrapolatory Implicit Boundary Integral Method

We review [Kublik *et al.* (2013)] as in (3.3) that for a parallel interface Γ_η that is η away from Γ and a function $f : \mathbb{R}^2 \times \mathbb{R}^2 \rightarrow \mathbb{C}$

$$\int_{\Gamma} f(x, y(s)) ds = \int_{\Gamma_\eta} f(x, y^*(s_\eta)) J_\eta ds_\eta, \quad (5.7)$$

where $y^* = y - d_\Gamma(y) \nabla d_\Gamma(y)$ is the projection point of $y \in \Gamma_\eta$ onto the interface Γ and d_Γ denote the signed distance function to the interface and J_η is the Jacobian for the change of variable to the parallel interface. The integral on the right hand side is not a function of η . Thus for any weight function supported on $[-\varepsilon, \varepsilon]$ with unit mass, we have

$$\begin{aligned} \int_{\Gamma} f(x, y(s)) ds &= \int_{-\varepsilon}^{\varepsilon} W(\eta) \int_{\Gamma_\eta} f(x, y^*(s_\eta)) J_\eta ds_\eta d\eta \\ &= \int_{\mathbb{R}^2} f(x, y^*) J(y) W(d_\Gamma(y)) dy. \end{aligned}$$

Note that the transform is an exact equality because the integral is not a function of η . Consequently the boundary integrals (5.2) (5.3) of the single layer formulation for the Neumann Problem can be analytically transformed into the following implicit forms:

$$\begin{aligned} u(x) &= \int_{T_{[-\varepsilon, \varepsilon]}} \phi(x, y^*) \alpha(y^*) J(y) W(d_\Gamma(y)) dy \quad x \in \bar{\Omega}^c. \\ g(x) = \frac{\partial u}{\partial n}(x) &= \int_{T_{[-\varepsilon, \varepsilon]}} \frac{\partial \phi}{\partial n_x}(x, y^*) \alpha(y^*) J_\eta(y) W(d_\Gamma(y)) dy - \frac{1}{2} \alpha(x) \quad x \in \Gamma. \end{aligned} \quad (5.8)$$

Here $T_{[a, b]}$ denote the tubular region that is $[a, b]$ (signed) away from the interface Γ .

To regularize the hypersingular integral with implicit boundary integral formulation, we need to extrapolate the kernel function values for $x \notin \Gamma$. We first define a family of weighting functions with unit mass and the first p moments vanishing:

Definition 5. Let $0 < \delta_0 < \varepsilon_0$. A function W is in the weighting function space $\mathbb{W}_{\delta_0, \varepsilon_0}^p$ if it satisfies the following properties:

$$\begin{cases} W(\eta) &= 0, \quad \eta \notin [\delta_0, \varepsilon_0]. \\ \int_{\delta_0}^{\varepsilon_0} W(\eta) d\eta &= 1. \\ \int_{\delta_0}^{\varepsilon_0} \eta^m W(\eta) d\eta &= 0, \quad m = 1 \dots p. \end{cases} \quad (5.9)$$

Now we state the main result:

Theorem 4. (*Generalized Implicit Boundary Integral Formulation*) Let Γ be a \mathcal{C}^2 compact interface in \mathbb{R}^m with principal curvatures denoted κ_i , $W \in \mathbb{W}_{\delta_0, \varepsilon_0}^p$ be a weighting function defined in (5.9), d_Γ be the signed distance function to the interface, then for any function $f : \mathbb{R}^m \times \Gamma \rightarrow \mathbb{C}$, $f \in \mathcal{C}^{p+1}(\mathbb{R}^m \times \Gamma)$ and all $\delta_0, \varepsilon_0, \min_{1 \leq i \leq m-1} |\frac{1}{\kappa_i}| > \varepsilon_0 > \delta_0 > 0$, we have for $x \in \Gamma$

$$\begin{aligned} &\int_{\Gamma} f(x, y(s)) ds \\ &= \int_{\mathbb{R}^n} f\left(x - d_\Gamma(y) \nabla d_\Gamma(x), y - d_\Gamma(y) \nabla d_\Gamma(y)\right) W(d_\Gamma(y)) J(y) dy \\ &\quad + \mathcal{O}\left(\varepsilon_0^{p+1} \sup_{\substack{\zeta \in (x, x + \varepsilon_0 n_x) \\ v \in \Gamma}} \left| \frac{\partial^{(p+1)} f(\zeta, v)}{\partial n_x^{(p+1)}} \right| \right), \end{aligned} \quad (5.10)$$

where $J(y)$ is the Jacobian for parametrizing at a parallel interface $\Gamma_{d(y)}$.

Proof. Let us first define a function $h(\eta) := \int_{\Gamma} f(x + \eta n_x, y(s)) ds$. Our goal is computing $h(0)$. Take a change of variable as in [Kublik *et al.* (2013)], we have

$$\begin{aligned} h(\eta) &= \int_{\Gamma} f(x + \eta n_x, y(s)) ds \\ &= \int_{\Gamma_{\eta}} f(x - \eta \nabla d_{\Gamma}(x), y^*(s_{\eta})) J(y) ds_{\eta}. \end{aligned}$$

With the properties of W , we expand the function h at 0 to degree p :

$$\begin{aligned} &\int_{\delta_0}^{\varepsilon_0} h(\eta) W(\eta) d\eta \\ &= \int_{\delta_0}^{\varepsilon_0} \left(h(0) + \eta h'(0) + \dots + \eta^p \frac{h^{(p)}(0)}{p!} + \eta^{(p+1)} \frac{h^{(p+1)}(\zeta)}{(p+1)!} \right) W(\eta) d\eta \\ &= h(0) + \int_{\delta_0}^{\varepsilon_0} \eta^{(p+1)} \frac{h^{(p+1)}(\zeta)}{(p+1)!} W(\eta) d\eta \\ &= h(0) + \int_{\delta_0}^{\varepsilon_0} \frac{\eta^{(p+1)} W(\eta)}{(p+1)!} \left(\int_{\Gamma} \frac{\partial^{(p+1)} f(\zeta, y(s))}{\partial n_x^{(p+1)}} ds \right) d\eta \\ &= h(0) + \mathcal{O}(\varepsilon_0^{p+1} \sup_{\substack{\zeta \in (x, x + \varepsilon_0 n_x) \\ v \in \Gamma}} \left| \frac{\partial^{(p+1)} f(\zeta, v)}{\partial n_x^{(p+1)}} \right|) \end{aligned} \quad (5.11)$$

The boundary integral with this generalized function f can be put in implicit form:

$$\begin{aligned} &\int_{\delta_0}^{\varepsilon_0} h(\eta) W(\eta) d\eta \\ &= \int_{\delta_0}^{\varepsilon_0} W(\eta) \left(\int_{\Gamma} f(x + \eta n_x, y(s)) ds \right) d\eta \\ &= \int_{\delta_0}^{\varepsilon_0} W(\eta) \left(\int_{\Gamma_{\eta}} f(x - \eta \nabla d_{\Gamma}(x), y(s_{\eta}) - \eta \nabla d_{\Gamma}(y(s_{\eta}))) J(y(s_{\eta})) ds_{\eta} \right) d\eta \\ &= \int_{\delta_0}^{\varepsilon_0} \int_{\Gamma_{\eta}} W(\eta) f(x - \eta \nabla d_{\Gamma}(x), y(s_{\eta}) - \eta \nabla d_{\Gamma}(y(s_{\eta}))) J(y(s_{\eta})) ds_{\eta} d\eta \\ &= \int_{\mathbb{R}^n} f(x - d_{\Gamma}(y) \nabla d_{\Gamma}(x), y - d_{\Gamma}(y) \nabla d_{\Gamma}(y)) W(d_{\Gamma}(y)) J(y) dy. \end{aligned} \quad (5.12)$$

Combining (5.11) with (5.12), we have the generalized implicit boundary integral formulation. □

5.3 Application on Helmholtz Neumann Problem

One difficulty of solving the Helmholtz Neumann Problem is that the kernel $K(x, y) := \frac{\partial^2 \phi}{\partial n_x \partial n_y}(x, y)$ is hypersingular and the integral $\int_{\Gamma} K(x, y(s)) \beta(y(s)) ds$ does not exist in the Riemann sense when $x \in \Gamma$. We cannot define $f(x, y) = K(x, y) \beta(y)$ and apply (5.10) directly. The reason to this peculiarity is that the solution to the Helmholtz equation

$$u(x) = \int_{\Gamma} \frac{\partial \phi}{\partial n_y}(x, y(s)) \beta(y(s)) ds - i\xi \int_{\Gamma} \phi(x, y(s)) \beta(y(s)) ds$$

is $\mathcal{C}^2(\bar{\Omega}^c) \cap \mathcal{C}(\bar{\Omega}^c \cup \Gamma)$ (this actually implies analyticity on $\bar{\Omega}^c$, see [Colton & Kress (2013)]). Therefore, the function is differentiable on only one side of the interface. The conventional normal derivative

$$\frac{\partial u}{\partial n_x}(x) = \frac{\partial}{\partial n_x} \left(\int_{\Gamma} \frac{\partial \phi}{\partial n_y}(x, y(s)) \beta(y(s)) ds - i\xi \int_{\Gamma} \phi(x, y(s)) \beta(y(s)) ds \right)$$

actually refers to the one-sided normal derivative when $x \in \Gamma$. Since the function is analytic for $x' \notin \Gamma$, derivatives are defined and the order of operations can be interchanged freely off interface:

$$\begin{aligned} \frac{\partial u}{\partial n_x^+}(x) &= \frac{\partial}{\partial n_x^+} \left(\int_{\Gamma} \frac{\partial \phi}{\partial n_y}(x, y(s)) \beta(y(s)) ds - i\xi \int_{\Gamma} \phi(x, y(s)) \beta(y(s)) ds \right) \\ &= \lim_{\lambda \rightarrow 0^+} \left(\frac{\partial}{\partial n_x} \left(\int_{\Gamma} \frac{\partial \phi}{\partial n_y}(x + \lambda n_x, y(s)) \beta(y(s)) ds \right. \right. \\ &\quad \left. \left. - i\xi \int_{\Gamma} \phi(x + \lambda n_x, y(s)) \beta(y(s)) ds \right) \right) \\ &= \lim_{\lambda \rightarrow 0^+} \left(\int_{\Gamma} \frac{\partial}{\partial n_x} \frac{\partial \phi}{\partial n_y}(x + \lambda n_x, y(s)) \beta(y(s)) ds \right. \\ &\quad \left. - i\xi \int_{\Gamma} \frac{\partial \phi}{\partial n_x}(x + \lambda n_x, y(s)) \beta(y(s)) ds \right). \end{aligned}$$

For $x \in \Gamma$, let

$$\tilde{h}(\eta) := \begin{cases} \int_{\Gamma} \left(\frac{\partial \phi}{\partial n_y}(x + \eta n_x, y(s)) - i\xi \phi(x + \eta n_x, y(s)) \right) \beta(y(s)) ds, & \eta > 0. \\ u(x), & \eta = 0. \end{cases}$$

Define the p th ($p \geq 1$) derivative of \tilde{h} as

$$\tilde{h}^{(p)}(\eta) := \begin{cases} \frac{d}{d\eta} \int_{\Gamma} \left(\frac{\partial \phi}{\partial n_y}(x + \eta n_x, y(s)) - i\xi \phi(x + \eta n_x, y(s)) \right) \beta(y(s)) ds, & \eta > 0 \\ \lim_{\lambda \rightarrow 0^+} \frac{1}{\lambda} (\tilde{h}^{(p-1)}(\lambda) - \tilde{h}^{(p-1)}(0)), & \eta = 0 \end{cases}$$

By the analyticity of u on either side of the interface [Colton & Kress (2013)], the function \tilde{h} has a Taylor's expansion with the derivative at $\eta = 0$ defined as above. With the well chosen weighting function $W \in \mathbb{W}_{\delta_0, \varepsilon_0}^p$, we apply the proof of Theorem 4 on \tilde{h}' to derive the following error estimate:

$$\begin{aligned} & \int_{\delta_0}^{\varepsilon_0} \tilde{h}'(\eta) W(\eta) d\eta \\ &= \tilde{h}'(0) + \int_{\delta_0}^{\varepsilon_0} \eta^{(p+1)} \frac{\tilde{h}^{(p+2)}(\zeta)}{(p+1)!} W(\eta) d\eta \\ &= \lim_{\lambda \rightarrow 0^+} \frac{1}{\lambda} (\tilde{h}(\lambda) - \tilde{h}(0)) + \int_{\delta_0}^{\varepsilon_0} \eta^{(p+1)} \frac{\tilde{h}^{(p+2)}(\zeta)}{(p+1)!} W(\eta) d\eta \\ &= \lim_{\lambda \rightarrow 0^+} \frac{1}{\lambda} (u(x + \lambda n_x) - u(x)) + \int_{\delta_0}^{\varepsilon_0} \eta^{(p+1)} \frac{\tilde{h}^{(p+2)}(\zeta)}{(p+1)!} W(\eta) d\eta \\ &= \frac{\partial u}{\partial n_x}(x) + \int_{\delta_0}^{\varepsilon_0} \eta^{(p+1)} \frac{\tilde{h}^{(p+2)}(\zeta)}{(p+1)!} W(\eta) d\eta \\ &= \frac{\partial u}{\partial n_x}(x) + \mathcal{O}(\varepsilon_0^{p+1} \sup_{\substack{\zeta \in (x + \delta_0 n_x, x + \varepsilon_0 n_x) \\ v \in \Gamma}} \left| \frac{\partial^{(p+2)} \phi(\zeta, v)}{\partial n_x^{(p+2)}} \right|). \end{aligned} \tag{5.13}$$

The last equality follows from the fact that the integral is off interface ($\delta_0 > 0$) and the higher order derivative has a dominating value over the lower order derivatives.

Once we reduce our task to evaluating $\int_{\delta_0}^{\varepsilon_0} \tilde{h}'(\eta) W(\eta) d\eta$, we apply the technique in (5.12)

to transform the boundary integral into an implicit integral. The interchanging of differentiation and integration is justified as the evaluations are all off interface ($\delta_0 > 0$). We summarize this extrapolatory implicit approach to solve the Helmholtz Neumann Problem:

Combined Layer Formulation for Exterior Neumann Problem using EIBIM:

1. Solve the potential density β for the combination potential

$$g(x) = \int_{T_{[\delta_0, \varepsilon_0]}} \left(\frac{\partial^2 \phi}{\partial n_x \partial n_y}(x + |d(y)|n_{x, y^*}) - i\xi \frac{\partial \phi}{\partial n_x}(x, y^*) \right) \beta(y^*) W(|d(y)|) J(y) dy$$

$$- \frac{1}{2} i\xi \beta(x) \quad x \in \partial\Omega. \quad (5.14)$$

2. Use the density β to evaluate u off interface

$$u(x) = \int_{T_{[\delta_0, \varepsilon_0]}} \left(\frac{\partial \phi}{\partial n_y}(x, y^*) - i\xi \phi(x, y^*) \right) \beta(y^*) W(|d(y)|) J(y) dy \quad x \in \bar{\Omega}^c. \quad (5.15)$$

5.4 Numerical Results in Two Dimensions

The numerical results in this section is divided into three parts. First we compare the formulation of (5.8) and (5.14) on cases where k is not an interior eigenvalue ($k = 1$), and where the wave number k is an interior eigenvalue of the unit disk ($k \approx 2.4048255577$) (The first ten eigenvalues of the unit disk can be found in [Reutskiy (2006)]). Then we compare the solutions of a non-convex kite shape, where the solution is known as in [Kress (1995)]. Finally we illustrate some scattering graphics generated by using the implicit methods. For simplicity, we will denote the numerical results using (5.8) as IBIM and the results using (5.14) as EIBIM.

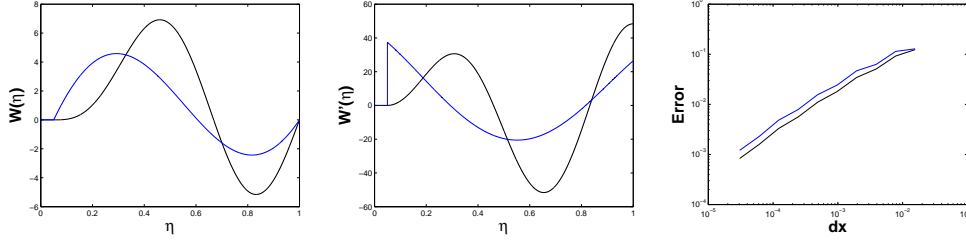


Figure 5.1: Weight function W_{EIBIM} (black) and W (blue). Both functions are in the weighting function space $\mathbb{W}_{0.1,1}^1$ as defined in (5.9). Additionally, W_{EIBIM} has two vanishing derivatives at δ_0 , whereas W is only continuous. The first two plots show the shape of the two weighting functions and their first derivatives. The third plot is the extrapolation error for the function $f(\eta) = \frac{1}{\sqrt{\eta+0.05}}$ on the interval $[0.1dx, \sqrt{dx}]$.

The explicit functions used in (5.8)(5.14) for the numerical results are as follows. The weight function for the IBIM formulation is the symmetric cosine weight:

$$W_{IBIM}(\eta) = \begin{cases} \frac{1}{2\varepsilon} (1 + \cos(\frac{\pi\eta}{\varepsilon})), & |\eta| < \varepsilon. \\ 0, & \text{otherwise.} \end{cases} \quad (5.16)$$

For the EIBIM combination method, the shifted sine function is used:

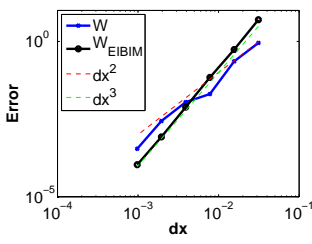
$$\begin{aligned} W_{EIBIM}(\eta) &= \frac{1}{\varepsilon_0} W_S(t = \frac{\eta}{\varepsilon_0}, \tau = \frac{\delta_0}{\varepsilon_0}) \\ &= \begin{cases} \frac{\pi}{\varepsilon_0(\tau-1)^2} (w_0^S(t, \tau) w_1^S(t, \tau)), & \delta_0 < \eta < \varepsilon_0. \\ 0, & \text{otherwise.} \end{cases} \end{aligned} \quad (5.17)$$

$$w_0^S(t, \tau) = \sin(\frac{\pi(t-1)}{2(\tau-1)}) \cos^3(\frac{\pi(t-1)}{2(\tau-1)}).$$

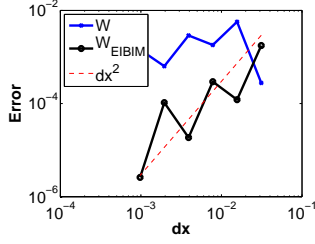
$$w_1^S(t, \tau) = 7 + \tau + 3(5 + 3\tau) \cos(\frac{\pi(\tau-t)}{\tau-1}).$$

One can check that $W_{EIBIM} \in \mathbb{W}_{\delta_0, \varepsilon_0}^1$ and additionally $W'_{EIBIM}(\delta_0) = W''_{EIBIM}(\delta_0) = 0$. From the error analysis (5.13), the analytic error is $\mathcal{O}(\varepsilon_0^2 \sup_{\substack{\zeta \in (x+\delta_0 n_x, x+\varepsilon_0 n_x) \\ v \in \Gamma}} |\frac{\partial^4 \phi(\zeta, v)}{\partial n_x^4}|)$.

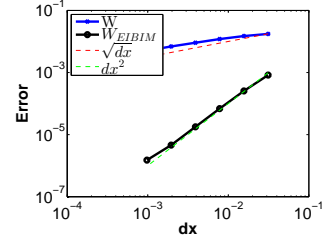
Numerically, regularity of the weighting functions can help tame the more singular values at δ_0 . To show this, we take another weight function $W \in \mathbb{W}_{\delta_0, \varepsilon_0}^1$ where W is only contin-



(a) Constant tubular width.



(b) Tubular width of $\mathcal{O}(\sqrt{H})$.
 $\delta_0 = \mathcal{O}(\sqrt{H})$, $\varepsilon_0 = \mathcal{O}(\sqrt{H})$.



(c) Tubular width of $\mathcal{O}(\sqrt{H})$.
 $\delta_0 = \mathcal{O}(H)$, $\varepsilon_0 = \mathcal{O}(\sqrt{H})$.

Figure 5.2: Error results for integration over hypersingular kernel with W (blue) and W_{EIBIM} (black). Both are in the weighting functions space $\mathbb{W}_{\delta_0, \varepsilon_0}^1$, as defined in (5.9). Additionally, we have $W'_{EIBIM}(\delta_0) = W''_{EIBIM}(\delta_0) = 0$ while W is only continuous at δ_0 .

uous at δ_0 and compare it with W_{EIBIM} (twice differentiable at δ_0). We first extrapolate the integral $f(\eta) = \frac{1}{\sqrt{\eta+0.05}}$ to evaluate $f(0)$. The weighting function that is twice differentiable at δ_0 yields a smaller error. An illustration of this comparison is shown in Figure 5.1. The advantage of using a weight with more regularity at δ_0 for a hypersingular kernel is even more obvious. We show the integral error with a hypersingular kernel using a constant tubular width (Figure 5.2a), a tubular width of $\mathcal{O}(\sqrt{H})$ (Figure 5.2b), and a tubular width of $\mathcal{O}(\sqrt{H})$ but width $\delta_0 = \mathcal{O}(H)$ (Figure 5.2c). The error from W_{EIBIM} has a higher order of convergence than W consistently.

We address that (5.14) must have enough points on the normal direction of the interface to resolve the wave, rather than just having enough points on the tangential direction as the case in the original KTT IBIM. This is because $\mathbf{x} + \eta \mathbf{n}_x$ jumps within the band of the hypersingular integrals in the new formulation (5.14), whereas in the original KTT IBIM integral (5.8), \mathbf{x} is a fixed point on the boundary.

For the combination parameter ξ , we use the formula (D.1)(D.2) as in [Kress & Spassov (1983)]. We leave the discussion of the choice of parameter ξ in Appendix D.

Table 5.1: Condition number of the operators to be inverted in IBIM (5.8) and EIBIM (5.14). $k = 1$ is not an eigenvalue. $k = 2.4048\dots$ is the first eigenvalue of the unit disk. The tube width is a constant.

	$k = 1$		$k = 2.4048255577$	
dx	Cond(\mathcal{M}_{IBIM})	Cond(\mathcal{M}_{EIBIM})	Cond(\mathcal{M}_{IBIM})	Cond(\mathcal{M}_{EIBIM})
$\frac{4}{128}$	2.72E+00	1.16E+02	6.50E+02	1.46E+02
$\frac{4}{256}$	2.70E+00	1.01E+02	9.74E+02	1.22E+02
$\frac{4}{512}$	2.69E+00	1.00E+02	1.88E+03	1.21E+02

5.4.1 Unit Circle

We show the results on a constant bandwidth $\delta_0 = 0.005$, $\varepsilon_0 = 0.15$ (See Figure 5.3), tubular width of $\mathcal{O}(\sqrt{H})$ (See Figure 5.4), and $\mathcal{O}(H)$ (See Figure 5.5). We set $\varepsilon = \frac{\varepsilon_0 - \delta_0}{2}$ so they have roughly same number of points inside the band. We can see that EIBIM is able to solve the exterior Neumann problem at both non-eigenvalues and eigenvalues. Note that for constant tube width, the error will saturate at finer grid because of the truncation error is proportional to ε_0^2 . For width of $\mathcal{O}(H)$, the error will diverge since the same number of points will need to resolve a larger bump as the band gets closer to the interface.

5.4.1.1 Constant Tube Width

The tubular width we test in this section is a constant width $\delta_0 = 0.005$, $\varepsilon_0 = 0.15$, $\varepsilon = \frac{\varepsilon_0 - \delta_0}{2}$. The size of the matrices for IBIM are 948, 3752, and 14908. The size of the matrices for EIBIM are 860, 3456, and 13796. We report the condition number of the matrix (Table 5.1) and test the solution for a non-eigenvalue $k = 1$ (Table 5.2) and an eigenvalue $k = 2.4048\dots$ (Table 5.3). We illustrate the error results with Figure 5.3.

5.4.1.2 Tube Width $\mathcal{O}(\sqrt{H})$

The tubular width in this section is taken to be $\delta_0 = 0.5H$, $\varepsilon_0 = \sqrt{H}$, $\varepsilon = \frac{\varepsilon_0 - \delta_0}{2}$. The size of the matrices for IBIM are 1036, 3000, 8684, and 24840. The size of the matrices for EIBIM

Table 5.2: Solution and relative error to the Neumann Helmholtz Problem using IBIM (5.8) and EIBIM (5.14). Wave number $k = 1$ is not an eigenvalue. u_e denotes the exact solution. The tubular width for EIBIM is $\delta_0 = 0.005$, $\varepsilon_0 = 0.15$. The tubular width for IBIM method is $\varepsilon = \frac{\varepsilon_0 - \delta_0}{2}$.

dx	$Re(u_e)$	$Re(u_{IBIM})$	Err_{IBIM}	$Re(u_{EIBIM})$	Err_{EIBIM}
$\frac{4}{128}$	0.719622	0.711141	1.18E-02	0.740852	2.95E-02
$\frac{4}{256}$		0.720568	1.31E-03	0.717483	2.97E-03
$\frac{4}{512}$		0.720053	5.99E-04	0.718210	1.96E-03
dx	$Im(u_e)$	$Im(u_{IBIM})$	Err_{IBIM}	$Im(u_{EIBIM})$	Err_{EIBIM}
$\frac{4}{128}$	0.162163	0.158838	2.05E-02	0.123289	2.40E-01
$\frac{4}{256}$		0.161680	2.98E-03	0.159302	1.76E-02
$\frac{4}{512}$		0.161891	1.68E-03	0.162697	3.29E-03

Table 5.3: Solution and relative error using IBIM (5.8) and EIBIM (5.14). Wave number $k = 2.4048255577\dots$ is an eigenvalue. The tubular width for EIBIM is $\delta_0 = 0.005$, $\varepsilon_0 = 0.15$. The tubular width for IBIM is $\varepsilon = \frac{\varepsilon_0 - \delta_0}{2}$.

dx	$Re(u_e)$	$Re(u_{IBIM})$	Err_{IBIM}	$Re(u_{EIBIM})$	Err_{EIBIM}
$\frac{4}{128}$	-0.117847	-0.600801	4.10E+00	-0.099827	1.53E-01
$\frac{4}{256}$		-0.324059	2.26E+00	-0.114964	2.45E-02
$\frac{4}{512}$		-0.322838	1.74E+00	-0.116073	1.51E-02
dx	$Im(u_e)$	$Im(u_{IBIM})$	Err_{IBIM}	$Im(u_{EIBIM})$	Err_{EIBIM}
$\frac{4}{128}$	0.472381	-0.173992	1.37E+00	0.451656	4.39E-02
$\frac{4}{256}$		-0.110502	1.23E+00	0.463844	1.81E-02
$\frac{4}{512}$		-0.109982	1.23E+00	0.465060	1.55E-02

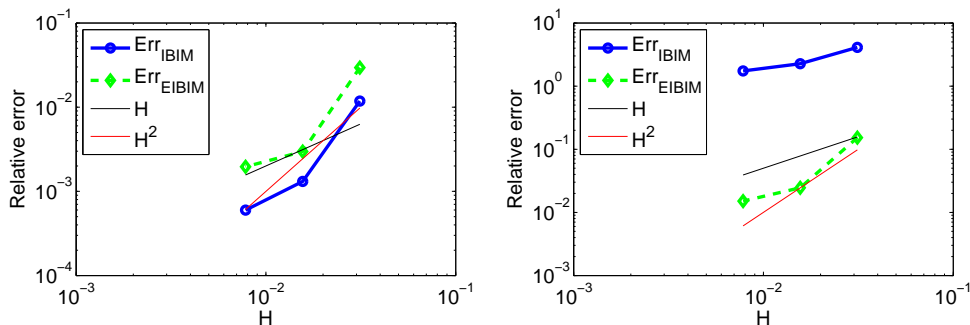


Figure 5.3: Solution error plots for non-eigenvalue $k = 1$ (left) and eigenvalue $k = 2.404825558\dots$ (right) using IBIM and EIBIM. The integration is performed on a constant width tubular region.

Table 5.4: Condition number of the operators to be inverted in IBIM (5.8) and EIBIM (5.14). $k = 1$ is not an eigenvalue. $k = 2.4048\dots$ is the first eigenvalue of the unit disk. The tube width is $\mathcal{O}(\sqrt{H})$.

	$k = 1$		$k = 2.4048255577$	
dx	Cond(\mathcal{M}_{IBIM})	Cond(\mathcal{M}_{EIBIM})	Cond(\mathcal{M}_{IBIM})	Cond(\mathcal{M}_{EIBIM})
$\frac{4}{128}$	2.70E+00	9.50E+01	5.40E+02	1.40E+02
$\frac{4}{256}$	2.69E+00	1.28E+02	9.54E+02	1.51E+02
$\frac{4}{512}$	2.69E+00	1.77E+02	1.87E+03	2.05E+02

Table 5.5: Solution and relative error to the Neumann Helmholtz Problem using IBIM (5.8) and EIBIM (5.14). Wave number $k = 1$ is not an eigenvalue. u_e denotes the exact solution. The tubular width for EIBIM is $\delta_0 = 0.5H$, $\varepsilon_0 = \sqrt{H}$. The tubular width for IBIM is $\varepsilon = \frac{\varepsilon_0 - \delta_0}{2}$.

dx	$Re(u_e)$	$Re(u_{IBIM})$	Err_{IBIM}	$Re(u_{EIBIM})$	Err_{EIBIM}
$\frac{4}{128}$	0.719622	0.718801	1.14E-03	0.713544	8.45E-03
$\frac{4}{256}$		0.720564	1.31E-03	0.723476	5.36E-03
$\frac{4}{512}$		0.720045	5.88E-04	0.718159	2.03E-03
$\frac{4}{1024}$		0.719815	2.68E-04	0.719753	1.81E-04
dx	$Im(u_e)$	$Im(u_{IBIM})$	Err_{IBIM}	$Im(u_{EIBIM})$	Err_{EIBIM}
$\frac{4}{128}$	0.162163	0.160431	1.07E-02	0.152353	6.05E-02
$\frac{4}{256}$		0.161668	3.05E-03	0.163314	7.10E-03
$\frac{4}{512}$		0.161902	1.61E-03	0.161219	5.83E-03
$\frac{4}{1024}$		0.162021	8.78E-04	0.162333	1.05E-03

are 940, 2804, 8356, and 24196. We report the condition number of the matrix (Table 5.4) and test the solution for a non-eigenvalue $k = 1$ (Table 5.5) and an eigenvalue $k = 2.4048\dots$ (Table 5.6). We illustrate the error results with Figure 5.4.

Table 5.6: Solution and relative error to the Neumann Helmholtz Problem using IBIM (5.8) and EIBIM (5.14). Wave number $k = 2.4048255577\dots$ is an eigenvalue. The tubular width for EIBIM is $\delta_0 = 0.5H$, $\varepsilon_0 = \sqrt{H}$. The tubular width for IBIM is $\varepsilon = \frac{\varepsilon_0 - \delta_0}{2}$.

dx	$Re(u_e)$	$Re(u_{IBIM})$	Err_{IBIM}	$Re(u_{EIBIM})$	Err_{EIBIM}
$\frac{4}{128}$	-0.117847	-0.543542	3.61E+00	-0.111288	5.57E-02
$\frac{4}{256}$		-0.327077	1.78E+00	-0.115184	2.26E-02
$\frac{4}{512}$		-0.320489	1.72E+00	-0.117085	6.46E-03
$\frac{4}{1024}$		-0.315194	1.67E+00	-0.117446	3.40E-03
dx	$Im(u_e)$	$Im(u_{IBIM})$	Err_{IBIM}	$Im(u_{EIBIM})$	Err_{EIBIM}
$\frac{4}{128}$	0.472381	-0.171159	1.36E+00	0.456347	3.39E-02
$\frac{4}{256}$		-0.110484	1.23E+00	0.469015	7.13E-03
$\frac{4}{512}$		-0.108450	1.23E+00	0.469175	6.79E-03
$\frac{4}{1024}$		-0.107306	1.23E+00	0.471316	2.26E-03

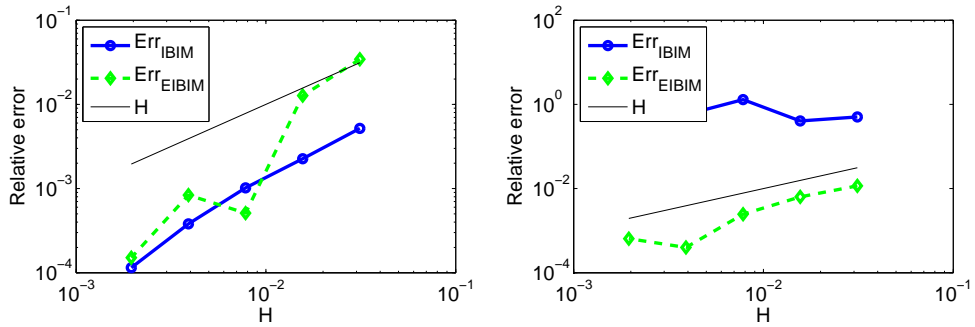


Figure 5.4: Solution error plots for non-eigenvalue $k = 1$ (left) and eigenvalue $k = 2.404825558\dots$ (right) using IBIM and EIBIM. The integration is performed on a tubular region with width of $\mathcal{O}(\sqrt{H})$.

5.4.1.3 Tube Width $\mathcal{O}(H)$

The tubular width $\delta_0 = 0.5H$, $\varepsilon_0 = 6.5H$, $\varepsilon = \frac{\varepsilon_0 - \delta_0}{2}$. The size of the matrices for IBIM are 1236, 2404, 4836, 9688, and 19328. The size of the matrices for EIBIM are 1072, 2240, 4708, 9552, and 19176. We report the condition number of the matrix (Table 5.7) and test the solution for a non-eigenvalue $k = 1$ (Table 5.8) and an eigenvalue $k = 2.4048\dots$ (Table 5.9). We illustrate the error results with Figure 5.5.

Table 5.7: The condition number of the operators to be inverted in IBIM (5.8) and EIBIM (5.14). $k = 1$ is not an eigenvalue. $k = 2.4048\dots$ is the first eigenvalue of the unit disk. The tube width is $\mathcal{O}(H)$

	$k = 1$		$k = 2.4048255577$	
dx	Cond(\mathcal{M}_{IBIM})	Cond(\mathcal{M}_{EIBIM})	Cond(\mathcal{M}_{IBIM})	Cond(\mathcal{M}_{EIBIM})
$\frac{4}{128}$	2.70E+00	9.50E+01	5.77E+02	1.38E+02
$\frac{4}{256}$	2.69E+00	1.61E+02	9.93E+02	1.88E+02
$\frac{4}{512}$	2.69E+00	3.43E+02	1.99E+03	3.81E+02

Table 5.8: The solution and relative error using IBIM (5.8) and EIBIM (5.14). Wave number $k = 1$ is not an eigenvalue. u_e denotes the exact solution. The tubular width for EIBIM is $\delta_0 = 0.5H$, $\varepsilon_0 = 6.5H$. The tubular width for IBIM is $\varepsilon = \frac{\varepsilon_0 - \delta_0}{2}$.

dx	$Re(u_e)$	$Re(u_{IBIM})$	Err_{IBIM}	$Re(u_{EIBIM})$	Err_{EIBIM}
$\frac{4}{128}$	0.719622	0.721610	2.76E-03	0.708438	1.55E-02
$\frac{4}{256}$		0.720625	1.39E-03	0.714493	7.13E-03
$\frac{4}{512}$		0.720096	6.59E-04	0.717871	2.43E-03
$\frac{4}{1024}$		0.719850	3.17E-04	0.722288	3.70E-03
$\frac{4}{2048}$		0.719733	1.55E-04	0.732947	1.85E-02
$\frac{4}{128}$		0.162163	0.161254	5.61E-03	0.152510
$\frac{4}{256}$	0.161691		2.91E-03	0.154170	4.93E-02
$\frac{4}{512}$	0.161921		1.50E-03	0.155298	4.23E-02
$\frac{4}{1024}$	0.162041		7.52E-04	0.153034	5.63E-02
$\frac{4}{2048}$	0.162102		3.79E-04	0.142887	1.19E-01

Table 5.9: The solution and relative error using IBIM (5.8) and EIBIM (5.15). Wave number $k = 2.4048255577 \dots$ is an eigenvalue. The tubular width for EIBIM is $\delta_0 = 0.5H$, $\varepsilon_0 = 6.5H$. The tubular width for IBIM is $\varepsilon = \frac{\varepsilon_0 - \delta_0}{2}$.

dx	$Re(u_e)$	$Re(u_{IBIM})$	Err_{IBIM}	$Re(u_{EIBIM})$	Err_{EIBIM}
$\frac{4}{128}$	-0.117847	-0.441122	2.74E+00	-0.112690	4.38E-02
$\frac{4}{256}$		-0.345925	1.94E+00	-0.114851	2.54E-02
$\frac{4}{512}$		-0.364585	2.09E+00	-0.115330	2.14E-02
$\frac{4}{1024}$		-0.375719	2.19E+00	-0.114242	3.06E-02
$\frac{4}{2048}$		-0.389311	2.30E+00	-0.109846	6.79E-02
$\frac{4}{128}$		0.472381	-0.145206	1.31E+00	0.451668
$\frac{4}{256}$	-0.113864		1.24E+00	0.464946	1.57E-02
$\frac{4}{512}$	-0.120919		1.26E+00	0.468097	9.07E-03
$\frac{4}{1024}$	-0.124683		1.26E+00	0.468355	8.52E-03
$\frac{4}{2048}$	-0.129543		1.27E+00	0.467003	1.14E-02

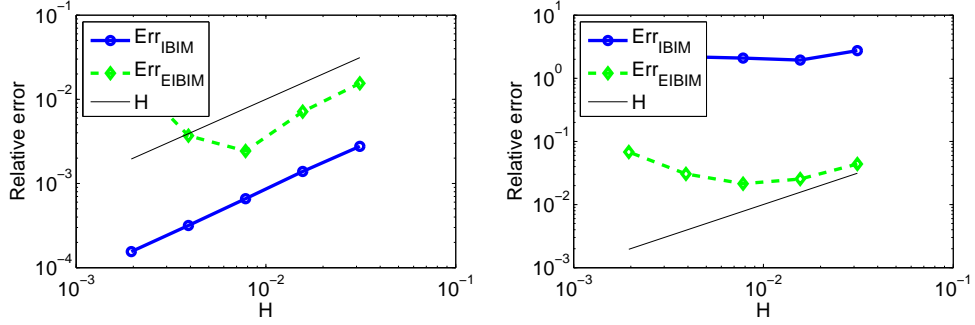


Figure 5.5: Solution error plots for non-eigenvalue $k = 1$ (left) and eigenvalue $k = 2.404825558\dots$ (right) using IBIM and EIBIM. The integration is performed on a tubular region of width $\mathcal{O}(H)$.

5.4.2 Kite Shape (Non-Convex)

We test our solution on the kite shape described by

$$\mathbf{y}(s) = (\cos(s) + 0.65 \cos(2s) - 0.65, 1.5 \sin(s)), \quad 0 \leq s \leq 2\pi, \quad (5.18)$$

and compare our solution with the solutions given in [Kress (1995)] using accurate regularization with explicit parametrization. The shape is illustrated in Figure 5.6. The incidental wave is $u^i = e^{ikd \cdot \mathbf{x}}$, where $d = (1, 0)$. [Kress (1995)] showed the exterior Neumann problem has directional far-field total wave

$$u_\infty(\hat{\mathbf{x}}) = \frac{e^{-\frac{i\pi}{4}}}{\sqrt{8\pi k}} \int_{\Gamma} (k\hat{\mathbf{x}} \cdot \mathbf{n}_y + \xi) e^{-ik\hat{\mathbf{x}} \cdot \mathbf{y}} \beta(\mathbf{y}) dS(\mathbf{y}),$$

where $\hat{\mathbf{x}}$ is the test direction and β is the resolved density using combined double and single layer potential with combination parameter ξ . We compare the error results for $k = 1$ (Table 5.10), $k = 3$ (Table 5.11), and $k = 5$ (Table 5.12).

Table 5.10: Far-field solution error on 2D kite shape described in (5.18). Wave number $k = 1$.

dx	$Re(\lim_{r \rightarrow \infty} u((r, 0)))$	Err	$Im(\lim_{r \rightarrow \infty} u((r, 0)))$	Err
-	0.151537	-	0.191535	-
$\frac{4}{128}$	0.131936	0.019601	0.159917	0.031618
$\frac{4}{256}$	0.133984	0.017553	0.174343	0.017192
$\frac{4}{512}$	0.141053	0.010484	0.181224	0.010311
$\frac{4}{1024}$	0.145569	0.005968	0.186459	0.005076
$\frac{4}{2048}$	0.148291	0.003246	0.188774	0.002761
dx	$Re(\lim_{r \rightarrow \infty} u((-r, 0)))$	Err	$Im(\lim_{r \rightarrow \infty} u((-r, 0)))$	Err
-	-1.102342	-	-0.509187	-
$\frac{4}{128}$	-1.074023	0.028319	-0.507663	0.001524
$\frac{4}{256}$	-1.109982	0.00764	-0.528309	0.019122
$\frac{4}{512}$	-1.1047	0.002358	-0.515955	0.006768
$\frac{4}{1024}$	-1.104736	0.002394	-0.515549	0.006362
$\frac{4}{2048}$	-1.103845	0.001503	-0.512877	0.00369

Table 5.11: Far-field solution error on 2D kite shape described in (5.18). Wave number $k = 3$.

dx	$Re(\lim_{r \rightarrow \infty} u((r, 0)))$	Err	$Im(\lim_{r \rightarrow \infty} u((r, 0)))$	Err
-	-0.036467	-	0.711221	-
$\frac{4}{128}$	-0.041236	0.004769	0.696300	0.014921
$\frac{4}{256}$	-0.057583	0.021116	0.710192	0.001029
$\frac{4}{512}$	-0.050893	0.014426	0.707467	0.003754
$\frac{4}{1024}$	-0.044105	0.007638	0.711591	0.00037
$\frac{4}{2048}$	-0.040943	0.004476	0.711862	0.000641
dx	$Re(\lim_{r \rightarrow \infty} u((-r, 0)))$	Err	$Im(\lim_{r \rightarrow \infty} u((-r, 0)))$	Err
-	-1.636892	-	-0.823357	-
$\frac{4}{128}$	-1.623179	0.013713	-0.806345	0.017012
$\frac{4}{256}$	-1.679449	0.042557	-0.812605	0.010752
$\frac{4}{512}$	-1.654864	0.017972	-0.822264	0.001093
$\frac{4}{1024}$	-1.651741	0.014849	-0.823977	0.00062
$\frac{4}{2048}$	-1.646324	0.009432	-0.823851	0.000494

Table 5.12: Far-field solution error on 2D kite shape described in (5.18). Wave number $k = 5$.

dx	$Re(\lim_{r \rightarrow \infty} u((r, 0)))$	Err	$Im(\lim_{r \rightarrow \infty} u((r, 0)))$	Err
-	-0.280672	-	-0.29818	-
$\frac{4}{128}$	-0.326625	0.045953	-0.220888	0.077292
$\frac{4}{256}$	-0.319861	0.039189	-0.239901	0.058279
$\frac{4}{512}$	-0.300958	0.020286	-0.271519	0.026661
$\frac{4}{1024}$	-0.29066	0.009988	-0.282961	0.015219
$\frac{4}{2048}$	-0.286097	0.005425	-0.290469	0.007711
dx	$Re(\lim_{r \rightarrow \infty} u((-r, 0)))$	Err	$Im(\lim_{r \rightarrow \infty} u((-r, 0)))$	Err
-	-1.947493	-	-1.275907	-
$\frac{4}{128}$	-1.928536	0.018957	-1.038644	0.237263
$\frac{4}{256}$	-1.98456	0.037067	-1.145499	0.130408
$\frac{4}{512}$	-1.960317	0.012824	-1.220294	0.055613
$\frac{4}{1024}$	-1.958113	0.01062	-1.245836	0.030071
$\frac{4}{2048}$	-1.955342	0.007849	-1.259986	0.015921

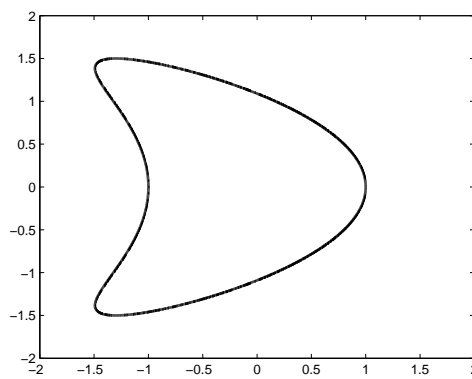


Figure 5.6: Kite shape described by (5.18).

5.4.3 Illustration of Scattering in Two Dimensions

In this section, we illustrate the scattering results by drawing the norm of the total wave. We compare the results using wave number $k = 1$ and $k = 5$ with a flower shape (Figure 5.7) and a moon shape with close and far sources (Figure 5.8).

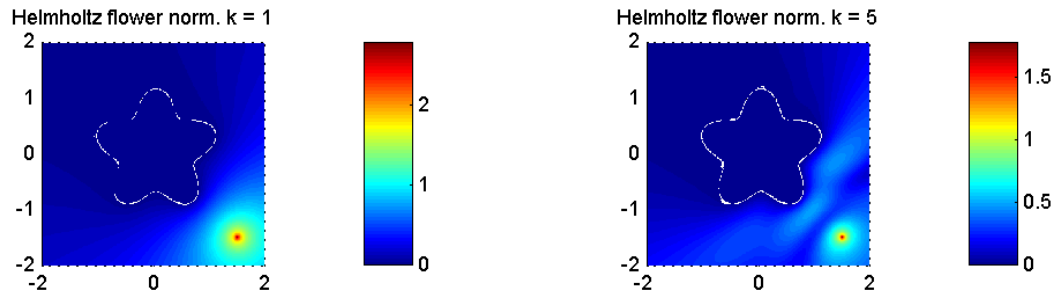


Figure 5.7: Scattering by a flower shape with Dirichlet boundary conditions. $k = 1, 5$.

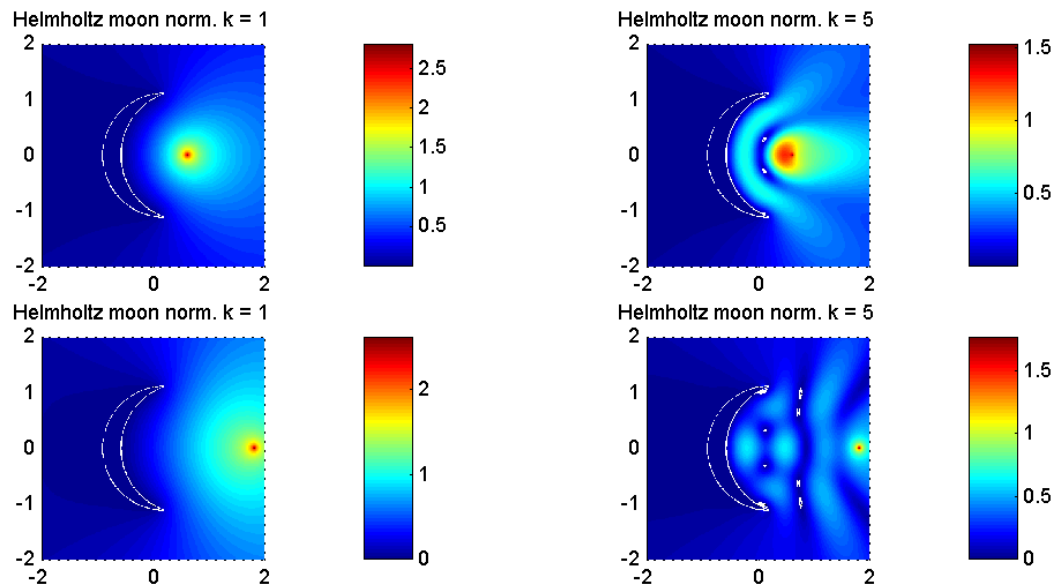


Figure 5.8: Scattering by a moon shape with Dirichlet boundary conditions. $k = 1, 5$. We compare the results where the wave source is near and far.

Table 5.13: Number of points in the computation tubular neighborhood.

H	$\delta_0^A = 0.005, \varepsilon_0^A = 0.3$	$\varepsilon^A = \sqrt{(\varepsilon_0^A)^2 - (\delta_0^A)^2}$	$\delta_0 = 0.1H, \varepsilon_0 = \sqrt{H}$	$\varepsilon = \sqrt{\varepsilon_0^2 - \delta_0^2}$
$\frac{4}{30}$	3220	3268	3924	3900
$\frac{4}{40}$	7512	7674	8078	7952
$\frac{4}{50}$	14972	14948	14000	13940
$\frac{4}{60}$	25744	26086	22052	21602
$\frac{4}{70}$	40740	41220	32440	32320
$\frac{4}{80}$	60980	61302	44796	45414
$\frac{4}{100}$	119020	120322	77629	78426

5.5 Numerical Results in Three Dimensions

As in the previous section, we use the cosine weight (5.16) for IBIM and the shifted sine weight (5.17) for EIBIM. We first test on eigenvalues and non-eigenvalues on a unit sphere for constant tubular width and for tubular width of $\mathcal{O}(\sqrt{H})$. Next we compare the solutions for a non-convex shape. We then illustrate some scattering results in 3D.

5.5.1 Unit Sphere

We show the results on a constant bandwidth $\delta_0 = 0.005, \varepsilon_0 = 0.3$ (See Figure 5.3) and tubular width of $\mathcal{O}(\sqrt{H})$ ($\varepsilon_0 = \sqrt{H}, \delta_0 = 0.1H$, see Figure 5.4). We take $\varepsilon = \sqrt{\varepsilon_0^2 - \delta_0^2}$ so the number of points will be roughly the same. The following tables show the width and the number of points in each scenario. We again see that EIBIM is able to solve the exterior Neumann problem at both non-eigenfrequencies and eigenfrequencies.

5.5.1.1 Constant Tube Width

We compare the solution to the exterior Neumann Helmholtz problem using IBIM on the single layer potential and EIBIM on the combination of single and double layer potentials. using a non-eigenvalue (Table 5.14) and an eigenvalue (Table 5.15) wave number k . The band has constant width $\delta_0 = 0.005, \varepsilon_0 = 0.3$. We illustrate the error results in Figure 5.9.

Table 5.14: The solution and relative error using IBIM with only one potential (5.8) and the EIBIM with both potentials (5.14). Wave number $k = 1$ is not an eigenvalue. u_e denotes the exact solution. The tubular width for EIBIM is $\delta_0 = 0.005$, $\varepsilon_0 = 0.3$. The tubular width for IBIM is $\varepsilon = \sqrt{\varepsilon_0^2 - \delta_0^2}$.

dx	$Re(u_e)$	$Re(u_{IBIM})$	Err_{IBIM}	$Re(u_{EIBIM})$	Err_{EIBIM}
$\frac{4}{30}$	-0.205768	-0.225221	9.45E-02	-0.793837	2.86E+00
$\frac{4}{40}$		-0.218142	6.01E-02	-0.325428	5.82E-01
$\frac{4}{50}$		-0.214985	4.48E-02	-0.283356	3.77E-01
$\frac{4}{60}$		-0.212991	3.51E-02	-0.220804	7.31E-02
$\frac{4}{70}$		-0.211673	2.87E-02	-0.220149	6.99E-02
$\frac{4}{80}$		-0.210776	2.43E-02	-0.204722	5.08E-03
$\frac{4}{90}$		-0.209910	2.01E-02	-0.204391	4.69E-03
$\frac{4}{100}$		-0.209610	1.87E-02	-0.204391	6.69E-03
dx	$Im(u_e)$	$Im(u_{IBIM})$	Err_{IBIM}	$Im(u_{EIBIM})$	Err_{EIBIM}
$\frac{4}{30}$	-0.741199	-0.777313	4.87E-02	-0.441240	4.05E-01
$\frac{4}{40}$		-0.763821	3.05E-02	-0.682795	7.88E-02
$\frac{4}{50}$		-0.757609	2.21E-02	-0.708353	4.43E-02
$\frac{4}{60}$		-0.753851	1.71E-02	-0.740213	1.33E-03
$\frac{4}{70}$		-0.751412	1.38E-02	-0.740388	1.09E-03
$\frac{4}{80}$		-0.749743	1.15E-02	-0.746361	6.97E-03
$\frac{4}{90}$		-0.748609	1.01E-02	-0.746361	6.97E-03
$\frac{4}{100}$		-0.747609	8.65E-03	-0.743564	3.19E-03

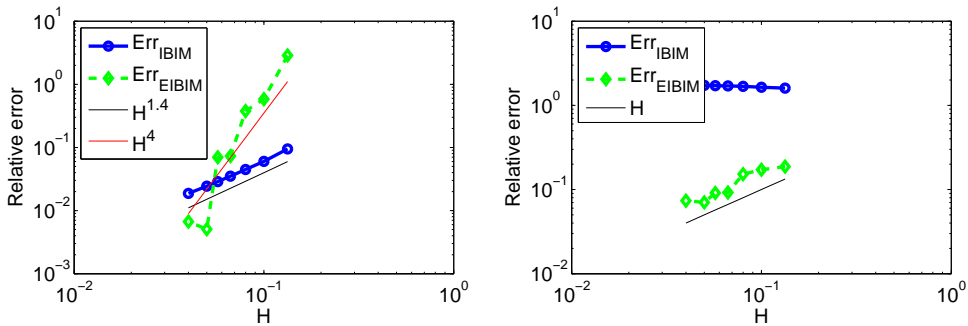


Figure 5.9: Relative Error for Helmholtz Neumann Problem in 3D on constant tubular width.

Table 5.15: The solution and relative error using IBIM with only one potential (5.8) and EIBIM with both potentials (5.14). Wave number $k = \pi$ is an eigenvalue. The tubular width for EIBIM is $\delta_0 = 0.005$, $\varepsilon_0 = 0.3$. The tubular width for IBIM is $\varepsilon = \sqrt{\varepsilon_0^2 - \delta_0^2}$.

dx	$Re(u_e)$	$Re(u_{IBIM})$	Err_{IBIM}	$Re(u_{EIBIM})$	Err_{EIBIM}
$\frac{4}{30}$	0.143921	-0.086553	1.60E+00	0.116937	1.87E-01
$\frac{4}{40}$		-0.091683	1.64E+00	0.119227	1.72E-01
$\frac{4}{50}$		-0.098112	1.68E+00	0.122059	1.52E-01
$\frac{4}{60}$		-0.100048	1.70E+00	0.130660	9.21E-02
$\frac{4}{70}$		-0.102288	1.71E+00	0.130813	9.11E-02
$\frac{4}{80}$		-0.105551	1.73E+00	0.133807	7.03E-02
$\frac{4}{100}$		-0.110590	1.77E+00	0.133334	7.36E-02
dx		$Im(u_e)$	$Im(u_{IBIM})$	Err_{IBIM}	$Im(u_{EIBIM})$
$\frac{4}{30}$	0.198091	0.099299	4.99E-01	0.162764	1.78E-01
$\frac{4}{40}$		0.102752	4.81E-01	0.162858	1.78E-01
$\frac{4}{50}$		0.110064	4.44E-01	0.168832	1.48E-01
$\frac{4}{60}$		0.112123	4.34E-01	0.178870	9.70E-02
$\frac{4}{70}$		0.114573	4.22E-01	0.179502	9.38E-02
$\frac{4}{80}$		0.118064	4.04E-01	0.182520	7.86E-02
$\frac{4}{100}$		0.123588	3.76E-01	0.183025	7.61E-02

5.5.1.2 Tube Width $\mathcal{O}(\sqrt{H})$

We compare the solution to the exterior Neumann Helmholtz problem using IBIM on the single layer potential and EIBIM on the combination of single and double layer potentials using a non-eigenvalue (Table 5.16) and an eigenvalue (Table 5.17) wave number k . The band has width $\delta_0 = 0.1H$, $\varepsilon_0 = \sqrt{H}$. We illustrate the error results in Figure 5.10.

Table 5.16: The solution and relative error using IBIM (5.8) and EIBIM (5.14). Wave number $k = 1$ is not an eigenvalue. u_e denotes the exact solution. The tubular width for EIBIM is $\delta_0 = 0.1H$, $\varepsilon_0 = \sqrt{H}$. The tubular width for IBIM is $\varepsilon = \sqrt{\varepsilon_0^2 - \delta_0^2}$.

dx	$Re(u_e)$	$Re(u_{IBIM})$	Err_{IBIM}	$Re(u_{EIBIM})$	Err_{EIBIM}
$\frac{4}{30}$	-0.205768	-0.224373	9.04E-02	-0.415482	1.02E+00
$\frac{4}{40}$		-0.218022	5.96E-02	-0.285181	3.86E-01
$\frac{4}{50}$		-0.214855	4.42E-02	-0.286292	3.91E-01
$\frac{4}{60}$		-0.212810	3.42E-02	-0.236729	1.50E-01
$\frac{4}{70}$		-0.211444	2.76E-02	-0.254808	2.38E-01
$\frac{4}{80}$		-0.210502	2.30E-02	-0.227409	1.05E-01
$\frac{4}{90}$		-0.209749	1.93E-02	-0.216433	5.18E-02
$\frac{4}{100}$					
dx	$Im(u_e)$	$Im(u_{IBIM})$	Err_{IBIM}	$Im(u_{EIBIM})$	Err_{EIBIM}
$\frac{4}{30}$	-0.741199	-0.776345	4.74E-02	-0.566261	2.36E-01
$\frac{4}{40}$		-0.763564	3.02E-02	-0.700634	5.47E-02
$\frac{4}{50}$		-0.757833	2.24E-02	-0.704991	4.89E-02
$\frac{4}{60}$		-0.754129	1.74E-02	-0.735219	8.07E-03
$\frac{4}{70}$		-0.751366	1.37E-02	-0.726710	1.95E-02
$\frac{4}{80}$		-0.749722	1.15E-02	-0.737676	4.75E-03
$\frac{4}{90}$		-0.748050	9.24E-03	-0.743145	2.63E-03
$\frac{4}{100}$					

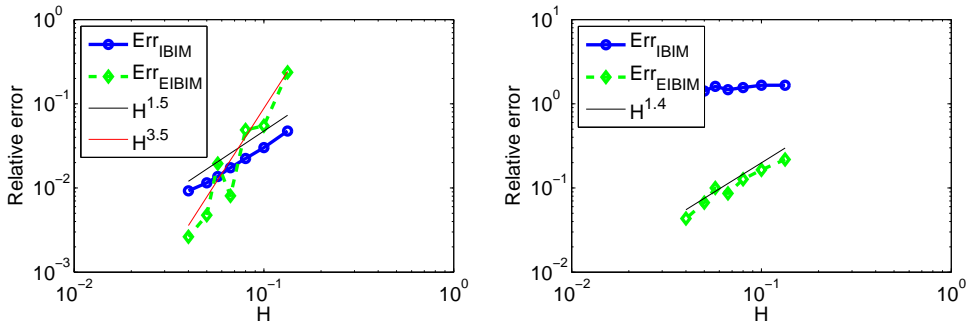


Figure 5.10: Relative Error for Helmholtz Neumann Problem in 3D. Tubular width is $\mathcal{O}(\sqrt{H})$.

Table 5.17: The solution and relative error using IBIM (5.8) and EIBIM (5.14). Wave number $k = \pi$ is an eigenvalue. The tubular width for EIBIM is $\delta_0 = 0.1H$, $\varepsilon_0 = \sqrt{H}$. The tubular width for IBIM is $\varepsilon = \sqrt{\varepsilon_0^2 - \delta_0^2}$.

$\frac{4}{30}$	0.143921	-0.094470	1.66E+00	0.112512	2.18E-01
$\frac{4}{40}$		-0.094490	1.66E+00	0.120267	1.64E-01
$\frac{4}{50}$		-0.079998	1.56E+00	0.125629	1.27E-01
$\frac{4}{60}$		-0.068139	1.47E+00	0.131535	8.61E-02
$\frac{4}{70}$		-0.088125	1.61E+00	0.129501	1.00E-01
$\frac{4}{80}$		-0.060890	1.42E+00	0.134285	6.70E-02
$\frac{4}{90}$		-0.088902	1.62E+00	0.137683	4.33E-02
$\frac{4}{100}$					
$\frac{4}{30}$	0.198091	0.105453	4.68E-01	0.142503	2.81E-01
$\frac{4}{40}$		0.105677	4.67E-01	0.163665	1.74E-01
$\frac{4}{50}$		0.086081	5.65E-01	0.171389	1.35E-01
$\frac{4}{60}$		0.070375	6.45E-01	0.179290	9.49E-02
$\frac{4}{70}$		0.098601	5.02E-01	0.178621	9.83E-02
$\frac{4}{80}$		0.059838	6.98E-01	0.185208	6.50E-02
$\frac{4}{90}$		0.098888	5.01E-01	0.188870	4.66E-02
$\frac{4}{100}$					

5.5.2 Bean Shape (Non-Convex)

We test on a non-convex shape in 3D as shown in Figure 5.11, the bean shape. The incident is taken to be $u_{inc} = e^{ikd \cdot x}$, where $d = (-1, 0, 0)$ and we record the consecutive difference of the solutions (scattered wave) and compare it with the solutions using IBIM (5.8) in Table 5.18. The tubular width is taken to be $\mathcal{O}(\sqrt{H})$, with $\varepsilon_0 = \sqrt{H}$, $\delta_0 = 0.1H$.

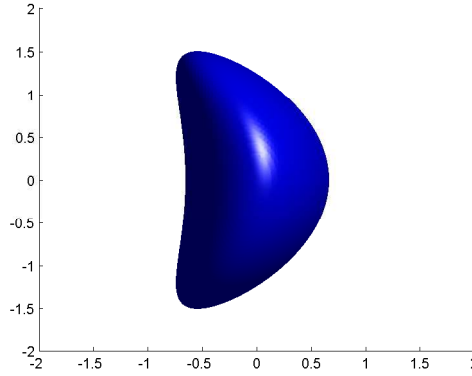


Figure 5.11: The bean shape. The interface is the zero set of $0.9(1.6x + (\frac{y}{1.6})^2)^2 + (\frac{y}{1.5})^2 + (\frac{z}{1.5})^2 = 1$

Table 5.18: Consecutive difference of the scatter wave solution and comparison with IBIM on bean shape. $k = 1$, $\varepsilon_0 = \sqrt{H}$. Evaluated at $(2, 2, 2)$.

dx	#points	$Re(u_{EIBIM})$	Con. Diff.	#points	$Re(u_{IBIM})$	$ Re_{EIBIM} - Re_{IBIM} $
$\frac{4}{30}$	5752	0.944556	-	5896	0.979018	0.034462
$\frac{4}{60}$	32888	0.972148	0.027592	33332	0.974335	0.002187
$\frac{4}{90}$	90964	0.946706	0.025442	91876	0.918696	0.028010
$\frac{4}{120}$	186714	0.930812	0.015894	188364	0.920763	0.010049
dx	#points	$Im(u_{EIBIM})$	Con. Diff.	#points	$Im(u_{IBIM})$	$ Im_{EIBIM} - Im_{IBIM} $
$\frac{4}{30}$	5752	0.043454	-	5896	0.349326	0.305872
$\frac{4}{60}$	32888	0.262999	0.219545	33332	0.349435	0.0864360
$\frac{4}{90}$	90964	0.303281	0.040282	91876	0.334712	0.031431
$\frac{4}{120}$	186714	0.318407	0.015126	188364	0.327899	0.009492

5.5.3 Illustration of Wave Scattering in Three Dimensions

In this section, we illustrate wave scattering in 3D by drawing the norm of the total wave. We show the results for $k = 3, 12$ on a torus in Figure 5.12. Then we illustrate a scattering result

for a bowl shape where the incident wave is not on the coordinate direction in Figure 5.13.

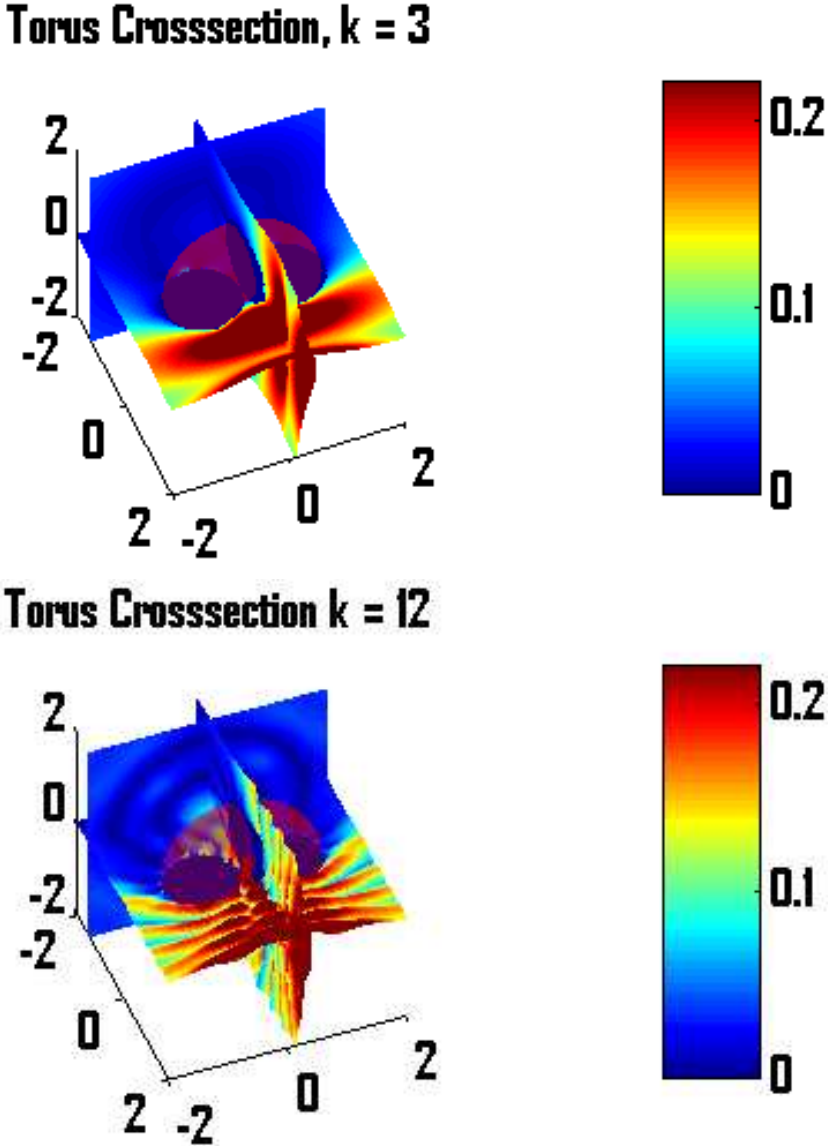


Figure 5.12: 3D scattering by a torus with Dirichlet boundary conditions using $k = 3, 12$.

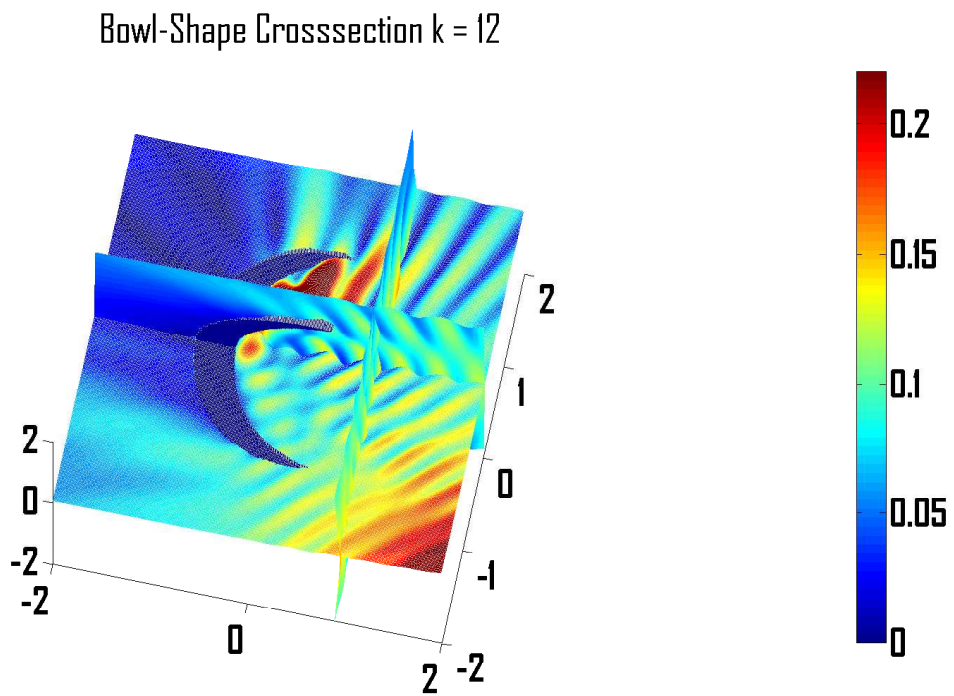
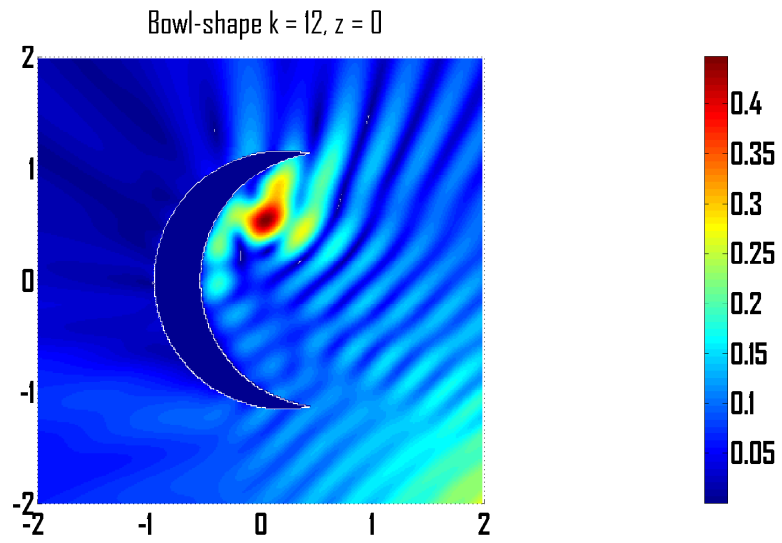


Figure 5.13: 3D scattering by bowl shape with Dirichlet boundary conditions using $k = 12$. The wave is in a slanted direction.

Chapter 6

Conclusion

This thesis solves two PDE problems in which the boundary is represented implicitly by the signed distance function.

The first part targets a nonlocal Stefan-type interface propagation problem, which may involve topological changes in two or three dimensions. We develop an algorithm that combines the advantages of level set methods, which incorporate irregular boundary shapes and their topological changes with ease, and boundary integral methods, which deal with exterior problems naturally. In particular, we simulate the Mullins-Sekerka model, which is a high order, nonlinear, nonlocal front propagation problem that simulates dendritic growth. Numerical experiments demonstrate the effectiveness of this algorithm in both two and three dimensions.

The second part of the thesis develops an extrapolatory implicit boundary integral method (EIBIM) to cope with boundary integral formulations bearing a hypersingular kernel. The particular model problem is the exterior Neumann Helmholtz problem, which typically requires the combination of singular and hypersingular integrals to cover solutions for all wave frequencies. By exploiting the integral embeddings across the parallel interfaces, EIBIM approximates the natural definition of the hypersingular-type boundary integral and avoids the artificial interpretation using Hadamard's finite part. This method carries over to different dimensions and manages irregular shapes with no extra complications. Numerical results il-

illustrate the effectiveness of this method to solve the exterior Neumann Helmholtz problem, regardless of the assigned frequencies and shapes.

Both algorithms work conveniently on Cartesian grids, and are compatible with any tree-structured adaptive grids. Fast Multipole Methods, preconditioning methods, and other established techniques including fast kernel evaluations (for Hankel functions) can be further explored to improve its numerical efficiency. Since the IBIM and EIBIM formulations rely on closest points to a manifold, they have the potential to generalize to applications involving manifolds with boundaries. The papers of [[Kublik *et al.* \(2013\)](#); [Kublik & Tsai \(2015\)](#)] and this thesis provide some of the necessary foundation for such applications. We also envision the work in this thesis can be further developed for a wide class of inverse problems.

Appendix A

Regularization for Helmholtz Kernels

In this appendix chapter, we derive the regularization terms for the normal derivative of the Helmholtz fundamental solution $\frac{\partial \Phi}{\partial n_y}$ for two points get close on the boundary Γ . For convenience, we also use the notation

$$G(x = |\mathbf{x} - \mathbf{y}|) = \Phi(\mathbf{x}, \mathbf{y}) = \begin{cases} -\frac{i}{4} H_0^{(1)}(k|x|), & \text{if } n = 2, \\ -\frac{e^{ik|x|}}{4\pi|x|}, & \text{if } n = 3, \end{cases} \quad (\text{A.1})$$

where $H_0^{(1)}(x)$ is the Hankel function of the first kind.

A.1 Regularization of $\frac{\partial \Phi}{\partial n_y}$ in Two Dimensions

As in the Laplace equation case [[Kublik et al. \(2013\)](#)], let \mathcal{C} be a C^2 curve in \mathbb{R}^2 and let z be a point on \mathcal{C} . We assume that we have a parametrization $(\mathbf{x}(t), \mathbf{y}(t))$ of \mathcal{C} and consider the Frenet frame associated to \mathcal{C} and centered at $z = (\mathbf{x}(t_0), \mathbf{y}(t_0)) \in \mathcal{C}$ for some $t_0 > 0$. In that frame z is the point $(0, 0)$, the x -axis is the tangent and the y -axis is the normal. For simplicity we denote by O the origin of the frame (which is also z). Locally around the origin, the equation of the curve can be written as a function $y = f(x)$. As a result we have

$f(0) = 0, f'(0) = 0$, and $f''(0) = \kappa(0) = \frac{1}{R}$ is the curvature of the curve at O . This curvature is also the curvature of \mathcal{C} at z .

Now consider the osculating circle of the curve \mathcal{C} at O . In the Frenet frame the osculating circle is centered at $(0, R)$. The equation of the circle (bottom portion) can be written as $y = R - \sqrt{R^2 - x^2}$, for $|x| < R$. For $|h| < R$ a small parameter we consider a point M on the osculating circle with coordinates $(h, R - \sqrt{R^2 - h^2})$ and a point P on the curve with coordinates $(h, f(h))$. We compute the difference of their y -coordinates:

$$\begin{aligned} f(h) - (R - \sqrt{R^2 - h^2}) &= f(0) + hf'(0) + \frac{h^2}{2}f''(0) + \frac{h^3}{6}f'''(0) + \mathcal{O}(h^4) \\ &= -R + R\left(1 - \frac{h^2}{2R^2} + \frac{h^4}{8R^4} + \mathcal{O}(h^6)\right) \\ &= \frac{h^2}{2R} + \frac{h^3}{6}f'''(0) - \frac{h^2}{2R} + \mathcal{O}(h^4) \\ &= \mathcal{O}(h^3). \end{aligned}$$

As this result works for all function f , we directly apply this result and estimate the normal derivative of the fundamental solution for the Helmholtz equation.

Let $M = (x, R - \sqrt{R^2 - x^2})$ (for $|x| \ll R$) and $P = (x, f(x))$ be defined as above. We compare the two quantities $\frac{\partial\Phi(M,O)}{\partial n_O}$ and $\frac{\partial\Phi(P,O)}{\partial n_O}$. First we notice that, using the Green's function defined in (A.1), we have

$$\begin{aligned} \frac{\partial\Phi(x,y)}{\partial n_y} &= \frac{\partial G(|x-y|)}{\partial |x-y|} \frac{\partial |x-y|}{\partial y} \cdot n_y \\ &= -G'(|x-y|) \frac{x-y}{|x-y|} \cdot n_y \\ &= -G'(|x-y|)|x-y| \frac{(x-y)}{|x-y|^2} \cdot n_y. \end{aligned}$$

And hence

$$\begin{aligned}
\frac{\partial \Phi(M, O)}{\partial n_O} &= -G'(|M - O|) |M - O| \frac{(M - O) \cdot n_O}{|M - O|^2} \\
&= -G'(|M - O|) |M - O| \frac{\sqrt{R^2 - x^2} - R}{x^2 + (R - \sqrt{R^2 - x^2})^2} \\
&= G'(|M - O|) |M - O| \frac{1}{2R}.
\end{aligned} \tag{A.2}$$

$$\begin{aligned}
\frac{\partial \Phi(P, O)}{\partial n_O} &= -G'(|P - O|) |P - O| \frac{(P - O) \cdot n_O}{|P - O|^2} \\
&= G'(|P - O|) |P - O| \frac{f(x)}{x^2 + f(x)^2} \\
&= G'(|P - O|) |P - O| \left(\frac{1}{2R} + \mathcal{O}(x) \right).
\end{aligned} \tag{A.3}$$

Now we look at $|M - O|$ and $|P - O|$. Since $|M - O| = \sqrt{x^2 + (R - \sqrt{R^2 - x^2})^2}$. Expanding $|M - O|$ around $x = 0$, we get

$$\begin{aligned}
|M - O| &= \sqrt{2R^2 - 2R\sqrt{R^2 - x^2}} \\
&= x + \frac{x^3}{8R^2} + \mathcal{O}(x^5).
\end{aligned}$$

Similarly, since $f(x) = R - \sqrt{R^2 - x^2} + \mathcal{O}(x^3)$,

$$\begin{aligned}
|P - O| &= \sqrt{x^2 + f(x)^2} = \sqrt{2R^2 - 2R\sqrt{R^2 - x^2} + \mathcal{O}(x^3)} \\
&= \sqrt{x^2 + \mathcal{O}(x^4) + \mathcal{O}(x^3)} \\
&= x + \mathcal{O}(x^3) + \mathcal{O}(x^2) \\
&= |M - O| + \mathcal{O}(x^2).
\end{aligned}$$

The higher order is deliberately written out to show the convergence of the Taylor expansion of $\sqrt{2R^2 - 2R\sqrt{R^2 - x^2}}$, which indicates that if the point O is overscutating, we would have

$|P - O| = x + \mathcal{O}(x^3) = |M - O| + \mathcal{O}(x^3)$. Using these results for (A.2) and (A.3), and the expansion of the Bessel function

$$\begin{aligned} G'(x) &= \frac{1}{2\pi|x|} + \frac{k}{2\pi} \left(\sum_{m=1}^{\infty} \frac{(-1)^m}{(m!)^2} \left(\frac{k|x|}{2}\right)^{2m-1} \left(m \log\left(\frac{k|x|}{2}\right) + \frac{1}{2} - m\left(\gamma + 1 + \frac{1}{2} + \dots + \frac{1}{m}\right)\right) \right) \\ &= \frac{1}{2\pi|x|} + \mathcal{O}(x \log(x)), \end{aligned}$$

where γ is the Euler constant. We have

$$\begin{aligned} \frac{\partial \Phi(M, O)}{\partial n_O} &= G'(x + \mathcal{O}(x^3)) |x + \mathcal{O}(x^3)| \frac{1}{2R} \\ &= \left(\frac{1}{2\pi(x + \mathcal{O}(x^3))} + \mathcal{O}(x \log(x)) \right) |x + \mathcal{O}(x^3)| \frac{1}{2R} \\ &= \frac{1}{4\pi R} \left(\frac{1}{x} + \mathcal{O}(x \log(x)) \right) |x + \mathcal{O}(x^3)| \\ &= \frac{1}{4\pi R} + \mathcal{O}(x^2 \log(x)). \end{aligned}$$

$$\begin{aligned} \frac{\partial \Phi(P, O)}{\partial n_O} &= G'(x + \mathcal{O}(x^2)) |x + \mathcal{O}(x^2)| \left(\frac{1}{2R} + \mathcal{O}(x) \right) \\ &= \left(\frac{1}{2\pi x} + \mathcal{O}(1) \right) |x + \mathcal{O}(x^2)| \left(\frac{1}{2R} + \mathcal{O}(x) \right) \\ &= \frac{1}{4\pi R} + \mathcal{O}(x). \end{aligned}$$

If curve is overosculating at the point O , we would have

$$\begin{aligned} \frac{\partial \Phi(P, O)}{\partial n_O} &= G'(x + \mathcal{O}(x^3)) |x + \mathcal{O}(x^3)| \left(\frac{1}{2R} + \mathcal{O}(x) \right) \\ &= \left(\frac{1}{2\pi x} + \mathcal{O}(x \log(x)) \right) |x + \mathcal{O}(x^3)| \left(\frac{1}{2R} + \mathcal{O}(x) \right) \\ &= \frac{1}{4\pi R} + \mathcal{O}(x^2 \log(x)). \end{aligned}$$

Consequently we have in general

$$\frac{\partial \Phi(P, O)}{\partial n_O} = \begin{cases} \frac{\partial \Phi(M, O)}{\partial n_O} + \mathcal{O}(x) = \frac{\partial \Phi(M, O)}{\partial n_O} + \mathcal{O}(|O - P|), & \text{in general.} \\ \frac{\partial \Phi(M, O)}{\partial n_O} + \mathcal{O}(x^2 \log(x)), & \text{when } O \text{ is a vertex.} \end{cases}$$

This concludes our regularization scheme for 2D Helmholtz kernel:

$$\left(\frac{\partial \Phi}{\partial n_y}(\mathbf{x}^*, \mathbf{y}^*) \right)_{reg} = \frac{\kappa(\mathbf{y}^*)}{4\pi}. \quad (\text{A.4})$$

A.2 Regularization of $\frac{\partial \Phi}{\partial n_y}$ in Three Dimensions

Notice the singularity of the Helmholtz Green's function $G(x) = \frac{-e^{ikx}}{4\pi x}$ is the same as the Green's function for Laplace equation $G_L(x) = \frac{-1}{4\pi x}$. With the derivative adds another singular term related to the wave number, we can expect similar regularization terms plus a first order term related to the wave number k .

Let \mathcal{S} be a C^2 surface in \mathbb{R}^3 , and let S, O be points on \mathcal{S} . Our goal is to approximate $\int_{U(\tau, S)} \frac{\partial \Phi(S, O)}{\partial n_O} dS(O)$ when S and O are close. The Green's function in three dimension has a higher degree of singularity, and hence does not have a limit for its normal derivative. However, the integral value still exists and we can approximate the derivative weakly by the integral value on a small surface. This is to say we are looking for a function K so that the following first order (weak) approximation holds:

$$\int_{U(\mathbf{x}; \tau)} K(\mathbf{x}, \mathbf{y}) dS(\mathbf{y}) = \int_{U(\mathbf{x}; \tau)} \frac{\partial \Phi(\mathbf{x}, \mathbf{y})}{\partial n_y^-} dS(\mathbf{y}).$$

With the approximation, we have the first order term equal, and the higher order terms vanish when the points are close. After performing Taylor's expansion on the targeted integral, we

have the two values are equal when passed to limit:

$$\begin{aligned} & \int_{U(\mathbf{x};\tau)} \frac{\partial\Phi(\mathbf{x},\mathbf{y})}{\partial n_{\mathbf{y}}^-} \beta(\mathbf{y}) dS(\mathbf{y}) \\ &= \beta(\mathbf{x}) \int_{U(\mathbf{x};\tau)} \frac{\partial\Phi(\mathbf{x},\mathbf{y})}{\partial n_{\mathbf{y}}^-} dS(\mathbf{y}) + \nabla\beta(\mathbf{x}) \cdot \int_{U(\mathbf{x};\tau)} \frac{\partial\Phi(\mathbf{x},\mathbf{y})}{\partial n_{\mathbf{y}}^-} (\mathbf{y} - \mathbf{x}) dS(\mathbf{y}) + \dots \end{aligned}$$

One candidate of K can be defined as follows:

$$K(\mathbf{x},\mathbf{y}) := \frac{1}{\tilde{U}(\mathbf{x};\tau)} \int_{\tilde{U}(\mathbf{x};\tau)} \frac{\partial\Phi(\mathbf{x},\mathbf{y})}{\partial n_{\mathbf{y}}^-} dS(\mathbf{y}),$$

where $\tilde{U}(\mathbf{x};\tau)$ is an approximating surface in the τ neighborhood of the point x . In this project, the approximating surface is chosen to be the paraboloid tangent to the point x for the subsequent 3D regularization:

Let O be the origin of the local coordinate system. The tangent plane is the xy -plane with principal directions being the x -axis and y -axis. Locally around the origin, the equation of the surface can be written as a function $z = f(x, y)$. As a result, we have $f(0, 0) = 0$, $f_x(0, 0), f_y(0, 0) = 0$, $f_{xx}(0, 0) = \kappa_1$, $f_{yy}(0, 0) = \kappa_2$, and $f_{xy}(0, 0) = 0$. We first use an osculating paraboloid to approximate the surface. We can write the equation of the paraboloid as

$$z(x, y) = \frac{1}{2}(\kappa_1 x^2 + \kappa_2 y^2).$$

Now, for $S = (x, y, f(x, y))$ sufficiently close to O , let $P = (x, y, z)$ be the point with the same xy coordinate on the paraboloid, we have

$$S - P = f(x, y) - \frac{1}{2}(\kappa_1 x^2 + \kappa_2 y^2) = \mathcal{O}(x^3, x^2 y, x y^2, y^3).$$

The osculating paraboloid has contact of order 3 in general. We examine the partial derivatives $\frac{\partial\Phi(S,O)}{\partial n_O}$ and $\frac{\partial\Phi(P,O)}{\partial n_O}$.

Recall from (refeq: 2D regularization) that

$$\frac{\partial \Phi(\mathbf{x}, \mathbf{y})}{\partial n_y} = -\frac{G'(|\mathbf{x} - \mathbf{y}|)}{|\mathbf{x} - \mathbf{y}|} (\mathbf{x} - \mathbf{y}) \cdot n_y.$$

we then have

$$\begin{aligned} \frac{\partial \Phi(S, O)}{\partial n_O} &= \frac{k|S - O| \sin(k|S - O|) + \cos(k|S - O|)}{|S - O|^3} (S - O) \\ &= \frac{1 + \mathcal{O}(|P - O|^2)}{|P - O|^3 (1 + \mathcal{O}(|P - O|^3))} (z + \mathcal{O}(|P - O|^3)). \\ &= \frac{\partial \Phi(P, O)}{\partial n_O} + \mathcal{O}(1). \end{aligned}$$

This means we can use $\frac{\partial \Phi(P, O)}{\partial n_O}$ for $\frac{\partial \Phi(S, O)}{\partial n_O}$ and get an error term of $\mathcal{O}(\tau^2)$. Hence we only need to evaluate $\frac{\partial \Phi(P, O)}{\partial n_O}$, which we are going to replace with the analytic average on the paraboloid.

We need to evaluate $\frac{\int_{\tilde{U}(\tau, O)} \frac{\partial \Phi(P, O)}{\partial n_O} dS(O)}{\int_{\tilde{U}(\tau, O)} 1 dS(O)}$. We can do this in polar coordinate. The denominator (area) is a standard calculation and the first few terms are

$$\int_0^\tau \int_0^{2\pi} r \sqrt{1 + r^2((\kappa_1 \cos(\theta))^2 + (\kappa_2 \sin(\theta))^2)} d\theta dr = \pi \tau^2 + \pi \left(\frac{\kappa_1^2 + \kappa_2^2}{8} \right) \tau^4 + \mathcal{O}(\tau^6).$$

As the numerator, we have

$$\begin{aligned} \frac{\partial \Phi(P, O)}{\partial n_O} &= \frac{G'(|P - O|)}{|P - O|} z \\ &= \frac{k|P - O| \sin(k|P - O|) + \cos(k|P - O|)}{4\pi|P - O|^3} z \\ &= \frac{1 + \frac{1}{2}(k|P - O|)^2 + \mathcal{O}(|P - O|^4)}{4\pi|P - O|^3} z. \end{aligned}$$

The term that differs from Laplace equation and makes an influence for more than $\mathcal{O}(\tau^2)$ is

$\frac{zk^2}{8\pi|P-O|}$. Therefore, we just need to find out

$$\begin{aligned}
& \int_{\bar{U}(\tau, O)} \frac{zk^2}{8\pi|P-O|} dS(O) \\
&= \frac{k^2}{8\pi} \int_0^\tau \int_0^{2\pi} \frac{r^2(\kappa_1 \cos^2 \theta + \kappa_2 \sin^2 \theta) \sqrt{1 + r^2(\kappa_1 \cos^2 \theta + \kappa_2 \sin^2 \theta)}}{4 + r^2(\kappa_1 \cos^2 \theta + \kappa_2 \sin^2 \theta)^2} d\theta dr \\
&= \frac{k^2}{48}(\kappa_1 + \kappa_2)\tau^3 + \mathcal{O}(\tau^5).
\end{aligned}$$

The last formula is a result of Taylor expansion and Matlab simplification. Now adding the term after division with the Laplace regularization, we get

$$\begin{aligned}
& \left(\frac{\partial \Phi(P, O)}{\partial n_O} \right)_{\text{avg}} \\
&= \frac{1}{8\pi\tau}(\kappa_1 + \kappa_2) - \frac{1}{\pi} \left(\frac{5}{512}(\kappa_1^3 + \kappa_2^3) + \frac{25}{1536}\kappa_1\kappa_2(\kappa_1 + \kappa_2) \right) \tau + \frac{k^2}{48\pi}(\kappa_1 + \kappa_2)\tau \\
&+ \mathcal{O}(\tau^3).
\end{aligned}$$

This concludes our 3D Helmholtz regularization scheme:

$$\begin{aligned}
& \left(\frac{\partial \Phi}{\partial n_y}(\mathbf{x}^*, \mathbf{y}^*) \right)_{\text{reg}} \\
&= \frac{1}{4\pi\tau}H(\mathbf{y}^*) - \frac{1}{\pi} \left(\frac{5}{256}H(\mathbf{y}^*)(4H^2(\mathbf{y}^*) - G(\mathbf{y}^*)) + \frac{25}{768}H(\mathbf{y}^*)G(\mathbf{y}^*) \right) \tau \quad (\text{A.5}) \\
&+ \frac{k^2}{24\pi}H(\mathbf{y}^*)\tau,
\end{aligned}$$

where $H(\mathbf{y}^*)$, $G(\mathbf{y}^*)$ denote the mean curvature and Gaussian curvature at the point $\mathbf{y}^* \in \Gamma$ respectively.

Appendix B

Adaptive Redistancing and Integral Quadrature

B.1 Adaptive Redistancing

The distance portfolio is essential for IBIM. Since we are only integrating on the ε neighborhood of the interface, adaptive gridding is a natural choice for efficient computations. In this appendix, we will briefly describe the method in [Min & Gibou (2007)] and illustrate some possible gridding results.

The adaptive gridding in two dimensions require a quadtree data structure (respectively, octtree for 3D). The simulated tree nodes are tile blocks that partitions the frame. For each node, the coordinate values are taken to be the center of the tile. So for example, the root layer (node) has coordinate value at $(0,0)$. When a certain criterion is satisfied in a specific node, we split the tree structure at the node to create a finer grid locally, as illustrated in . The splitting algorithm adopted for our numerical experiments is summarized as follows.

The rationale for the above algorithm is to have finer grid when the curvature is large. However, we want to eliminate points that have large Laplacian but are far from the boundary (e.g. the center of a circle), so we need to first have finer grid near the interface. To test

Algorithm B.1 Algorithm for adaptive grid splitting.

```
Initialize root node. Set up MIN_LAYER, MIDDLE_LAYER, MAX_LAYER
Start with root node and enter the recursive part
IF current layer > MAX_LAYER THEN
    Set children to be NULL and return
END
IF current layer < MIN_LAYER THEN
    SPLIT NODE
ELSE
    IF current layer  $\leq$  MIDDLE_LAYER THEN
        IF node cuts through tube THEN
            SPLIT NODE
        ELSE
            Set children to be NULL and return
        END
    ELSE
        IF node curvature times current grid size > threshold THEN
            SPLIT NODE
        ELSE
            Set children to be NULL and return
        END
    END
END
END
```

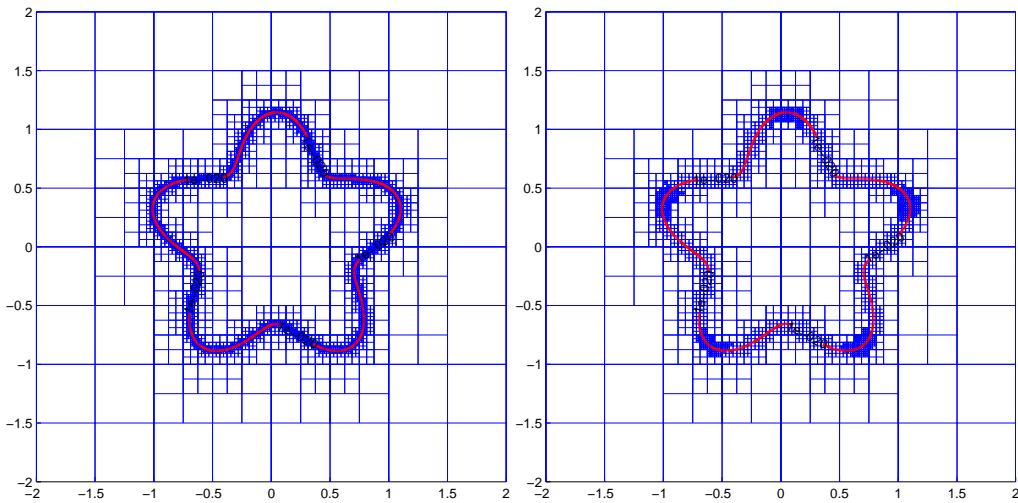


Figure B.1: Tree splitting based on distance (left) and both distance and curvature (right) on a flower shape.

whether a tile block intersects the interface, we adopt the Whitney decomposition

$$\min_{v \in \text{vertices}(C)} |\phi(v)| \leq \text{Lip}(\phi) \cdot \text{diag-size}(C),$$

where $\text{Lip}(\phi) = \max_{x, y \in \text{vertices}(C), x \neq y} \frac{|\phi(x) - \phi(y)|}{|x - y|}$. Of course, we need a minimum splitting level so that the resolution is good enough to correctly detect the interface intersection. Comparison of this splitting criterion and the usual splitting based on distance to boundary is illustrated for a flower shape (Figure B.1) and a star shape (Figure B.2).

The main challenge for computations on adaptive grid is the existence of junction points, or "ghost points" as termed in [Min & Gibou (2007)]. Junction points occur when two adjacent nodes have different refinement levels, which makes it possible to have no corresponding point in the coarser node when calculating finite difference derivatives, illustrated as follows:

Using second order finite difference schemes for the derivatives on adaptive grids as described in [Min & Gibou (2007)] to propagate the eikonal equation, we can have a second order redistancing scheme on adaptive grids.

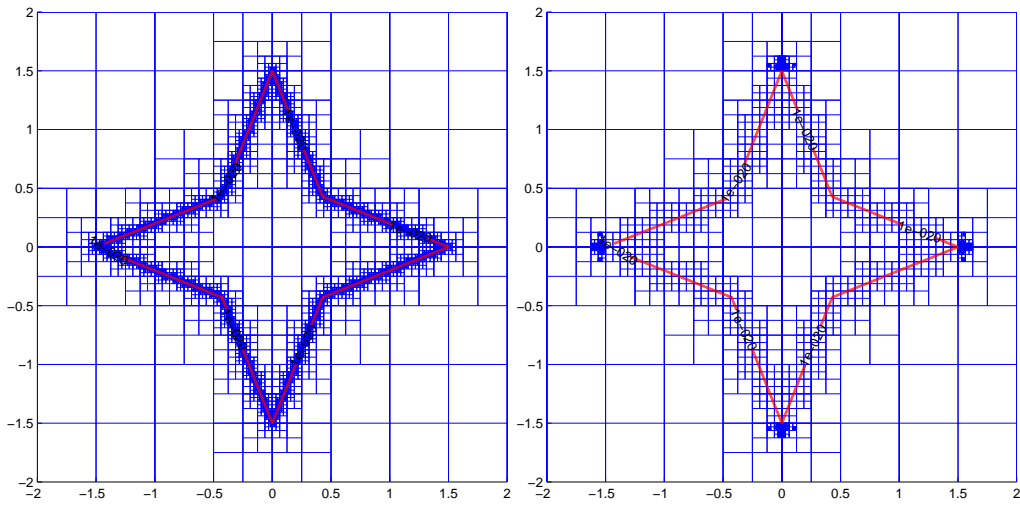


Figure B.2: Tree splitting based on distance (left) and both distance and curvature (right) on a star shape.

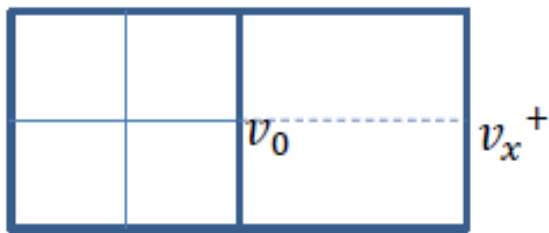


Figure B.3: The cell on the left has finer resolution, and hence the point in the middle has no neighbor on its right in the coarser cell.

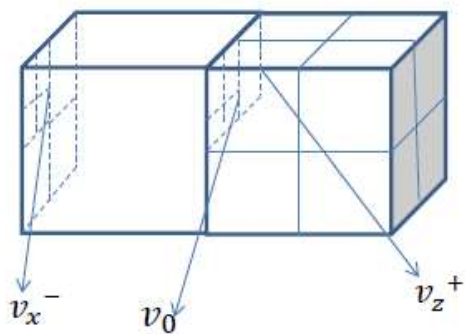


Figure B.4: The closer upper left subcell in the right cell has the finest resolution. The case in 3D is more complicated in that one point may have up to two ghost neighbors. And depending on the situation, the interpolation may be a 2D interpolation.

B.2 Integration on Adaptive Grid

Suppose we are integrating the function f on a rectangular domain D . The analytic integral is expressed as $I = \int_D f(p) dx dy$.

Let S be the side length of the frame, L_j denote the collection of cells having resolution 2^j , which means the sides of the square cells in this resolution have length $\frac{S}{2^j}$ (call it layer j collection). Let N_j be the number of cells in level j , $\{Q_i^j\}$ be the cells in layer j collection. Suppose the finest resolution on the adaptive grid is 2^M , and the adaptive grid is split so that the smallest resolution within the integration domain is level k . Then in 2D the trapezoidal quadrature on the adaptive grid I_k is defined as follows:

$$I_k = \sum_{j=k}^M \sum_{i=1}^{N_j} h_j^2 \frac{(f(p_i^{nw}) + f(p_i^{ne}) + f(p_i^{sw}) + f(p_i^{se}))}{4},$$

where $h_j = \frac{S}{2^j}$ is the side length of the cell in level j , p_i is the center of the cell Q_i^j , and $p_i^{nw}, p_i^{ne}, p_i^{sw}, p_i^{se}$ are the four corners (northwest, northeast, southwest, southeast) of the cell Q_i^j , as illustrated in Figure B.5.

For 3D adaptive grid, the trapezoidal quadrature on the local cell is

$$I_k = \sum_{j=k}^M \sum_{i=1}^{N_j} h_j^2 \frac{(f(p_i^{cnw}) + f(p_i^{cne}) + f(p_i^{csw}) + f(p_i^{cse}) + f(p_i^{fnw}) + f(p_i^{fne}) + f(p_i^{fsw}) + f(p_i^{fse}))}{8},$$

where c stands for close, and f stands for far.

A direct computation verifies that the quadrature is exact for any degree one polynomial.

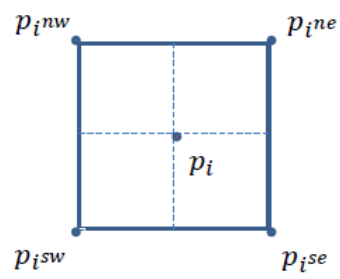


Figure B.5: Local trapezoidal rule illustration in 2D.

Appendix C

Numerical Results of CCL with IBIM on Dirichlet Laplace Problems

With the help of connected component labeling (CCL) algorithm described in [4.3.2](#), we can apply the implicit formulations in [4.3.3](#) and solve Dirichlet Laplace problems in general multiply connected regions. We will demonstrate the effectiveness with numerical results in two and three dimensions.

C.1 Two Dimensions

Since the exact solution is difficult to obtain, we use the constant boundary condition for multi-hole region and multi-piece concentric circles. For multi-layered annulus, we do have an exact solution for non-constant boundary condition. We record the error convergence below.

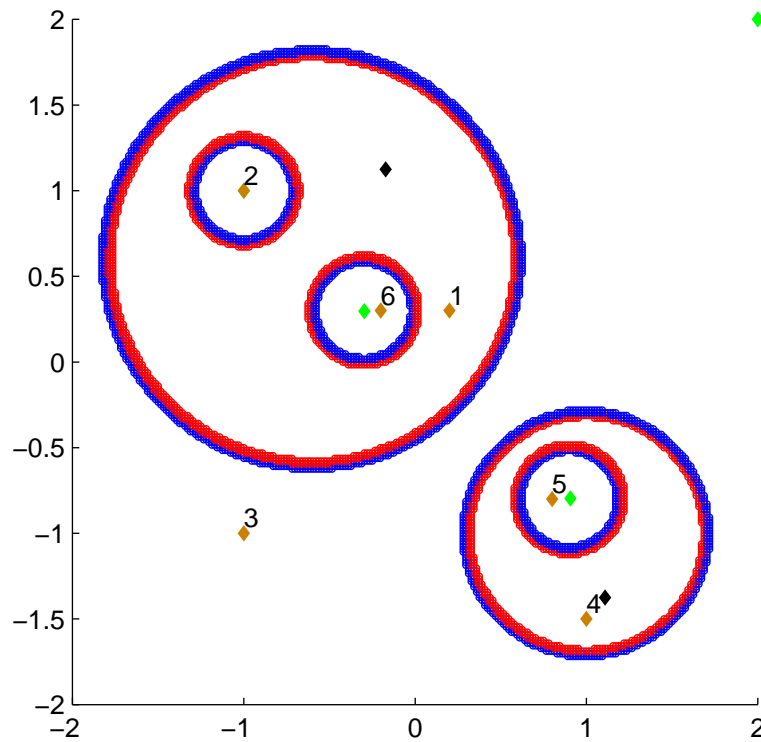


Figure C.1: Illustration of the regions and the test points. The interior regions are surrounded by red boundary and exterior surrounded by blue. The green dots are representative points selected by CCL so that they are furthest from boundary in exterior regions, while black dots are for interior regions. The test points are labeled and colored brown. The boundary condition is taken to be the constant 1.

C.1.1 Multi-Hole Region

C.1.2 Multi-Piece Concentric Circles

C.1.3 Multi-Layered Annulus

For the third case, we test on a multi-layered annulus. We use a boundary condition compatible with the Mullins-Sekerka simulation. In this case, the boundary condition is taken to be the signed curvature of a point x on the boundary with the inmost circle clockwise (negative) orientation.

Table C.1: The convergence of solution to Laplace equation with interface illustrated in Figure C.1 on page 121. The boundary condition is taken to be the constant 1. The error is taken to be the absolute error. The convergence order is approximately approaching one.

N	64	128	256	512	1024	2048
Error P1	1.93E-02	1.01E-02	4.07E-03	1.90E-03	9.77E-04	4.77E-04
Order P1	-	0.93	1.32	1.10	0.96	1.04
Error P2	2.27E-04	1.72E-04	6.55E-05	1.83E-05	1.10E-05	6.09E-06
Order P2	-	0.40	1.39	1.84	0.73	0.86
Error P3	1.12E+00	5.67E-03	2.57E-03	1.23E-03	5.18E-04	2.25E-04
Order P3	-	7.62	1.14	1.06	1.25	1.21
Error P4	7.88E-04	2.45E-05	2.73E-05	2.20E-05	9.53E-06	4.36E-06
Order P4	-	5.01	-0.16	0.31	1.21	1.13
Error P5	2.52E-04	3.77E-04	1.59E-04	5.62E-05	3.08E-05	1.64E-05
Order P5	-	-0.58	1.25	1.50	0.87	0.91
Error P6	2.26E-03	2.83E-04	1.51E-04	7.95E-05	4.00E-05	2.05E-05
Order P6	-	2.99	0.91	0.92	0.99	0.97

Table C.2: The convergence of solution to Laplace equation with interface illustrated in Figure C.2 on page 123. The boundary condition is taken to be the constant 1. The convergence order is approximately approaching one.

N	64	128	256	512	1024	2048
Error P1	1.93E-02	1.01E-02	4.07E-03	1.90E-03	9.77E-04	4.77E-04
Order P1	-	0.93	1.32	1.10	0.96	1.04
Error P2	3.92E-02	9.31E-03	3.81E-03	1.82E-03	9.08E-04	4.71E-04
Order P2	-	2.07	1.29	1.07	1.00	0.95
Error P3	1.69E-01	1.12E+00	9.92E-03	4.08E-03	1.80E-03	7.29E-04
Order P3	-	-2.73	6.82	1.28	1.18	1.30
Error P4	2.03E-01	7.23E-03	2.61E-03	1.05E-03	4.11E-04	1.80E-04
Order P4	-	4.81	1.47	1.32	1.35	1.19
Error P5	1.12E+00	5.67E-03	2.57E-03	1.23E-03	5.18E-04	2.25E-04
Order P5	-	7.62	1.14	1.06	1.25	1.21
Error P6	2.12E-02	1.15E-02	4.35E-03	1.93E-03	8.28E-04	3.25E-04
Order P6	-	0.89	1.40	1.17	1.22	1.35
Error P7	4.12E-01	5.22E-03	2.62E-03	1.32E-03	8.72E-04	3.47E-04
Order P7	-	6.30	0.99	0.99	0.60	1.33
Error P8	6.44E-03	2.55E-03	8.02E-04	3.32E-04	1.97E-04	1.11E-04
Order P8	-	1.33	1.67	1.27	0.76	0.83
Error P9	2.29E-04	1.73E-04	6.56E-05	1.83E-05	1.10E-05	6.13E-06
Order P9	-	0.41	1.40	1.84	0.73	0.85

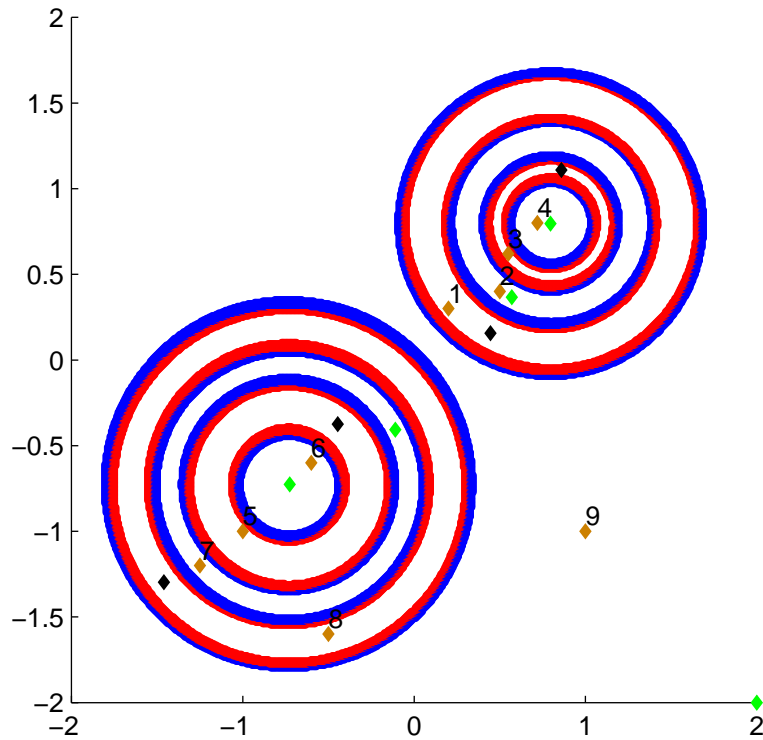


Figure C.2: Illustration of the regions and the test points. As in Figure C.1, the interior regions are surrounded by red boundary and exterior surrounded by blue. The green dots are representative points selected by CCL so that they are furthest from boundary in exterior regions, while black dots are for interior regions. The test points are labeled and colored brown. The boundary condition is taken to be the constant 1.

Let R_1, R_2, \dots, R_M be the radii of the concentric circles, with $0 < R_1 < R_2 < \dots < R_M < \infty$.

The boundary condition is

$$f(x) = (-1)^i \frac{1}{R_i} \text{ for } \|x\| = R_i.$$

The exact solution for $r = \|x\|$ is then

$$u(x) = \begin{cases} \kappa_1, & \|x\| < R_1. \\ \kappa_{i-1} + \frac{\ln r - \ln R_{i-1}}{\ln R_i - \ln R_{i-1}} (\kappa_i - \kappa_{i-1}), & R_{i-1} \leq \|x\| < R_i \text{ (} i = 2 \dots M \text{)}. \\ \kappa_M, & R_M < \|x\|. \end{cases}$$

The test case uses $M = 6$, illustrated in Figure C.3 on page 124. The solution convergence result is presented in Table C.3 on page 125.

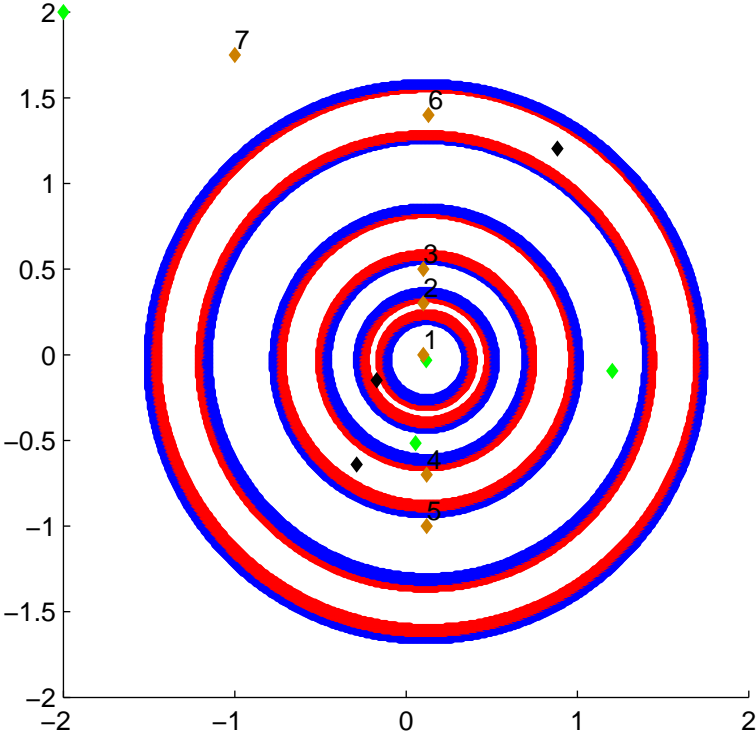


Figure C.3: Illustration of a multi-layered annulus and the test points. The boundary condition is the signed curvature on the interface, as one would encounter for Mullins-Sekerka simulations. The solution is a linear combination of a constant and a logarithm of the norm depending on the region.

Table C.3: The convergence of solution to Laplace equation with interface illustrated in Figure C.3 on page 124. The boundary condition is taken to be the signed curvature of the curve, with the inmost curve having the clockwise (negative) orientation. The absolute error is larger at point 2 and point 3 because the points are closer to the boundary. The convergence order is approximately approaching one.

N	64	128	256	512	1024	2048
Error P1	7.47E-01	3.18E-02	1.38E-02	4.62E-03	1.92E-03	8.04E-04
Order P1	-	4.56	1.20	1.58	1.26	1.26
Error P2	2.37E+00	1.47E-01	1.04E-01	7.13E-02	3.13E-02	1.46E-02
Order P2	-	4.01	0.50	0.54	1.19	1.10
Error P3	3.96E-01	1.12E-01	6.08E-02	2.81E-02	1.52E-02	7.46E-03
Order P3	-	1.83	0.88	1.12	0.88	1.03
Error P4	1.14E+00	1.89E-02	6.43E-02	5.81E-02	3.42E-03	4.23E-03
Order P4	-	5.91	-1.77	0.15	4.09	-0.31
Error P5	7.70E-02	3.59E-02	2.37E-02	1.50E-02	5.60E-03	1.76E-03
Order P5	-	1.10	0.60	0.66	1.42	1.67
Error P6	5.20E-02	3.22E-02	7.16E-03	2.40E-03	1.38E-03	7.18E-04
Order P6	-	0.69	2.17	1.58	0.80	0.94
Error P7	3.45E-04	8.64E-05	4.70E-05	2.59E-05	1.29E-05	6.42E-06
Order P7	-	2.00	0.88	0.86	1.00	1.01

C.2 Three Dimensions

We show the error results for solving Dirichlet Laplace problems in multiply connected regions using the CCL based IBIM. As in two dimensions, we test constant boundary conditions on two multi-layered balls (Table C.4 on page 126) and non-constant boundary condition on one multi-layered ball (Table C.5 on page 127), of which we have analytic solutions below.

For the single multi-layered ball we use a boundary condition compatible with the Mullins-Sekerka simulation. In this case, the values on boundary are taken to be the signed curvature of a point \mathbf{x} on the boundary with the inmost circle clockwise (negative) orientation.

Let R_1, R_2, \dots, R_M be the radii of the concentric circles, with $0 < R_1 < R_2 < \dots < R_M < \infty$. The boundary condition is

$$f(x) = (-1)^i \frac{1}{R_i} \text{ for } \|x\| = R_i.$$

Table C.4: The solution error for two multi-layered balls. The testing boundary condition is the constant 1. The first multi-layered ball is centered at $(-0.5, -0.5, -0.5)$ with radii 0.23, 0.47, 0.72, 0.95. The second multi-layered ball is centered at $(0.8, 0.8, 0.8)$ with radii 0.31, 0.61. The convergence order seems to approach 1.

N	32	64	128	Distance
Error P1	1.54E-01	1.07E-02	7.41E-03	-0.1300
Order P1	-	3.85	0.53	
Error P2	1.61E-01	1.59E-02	7.26E-03	0.1062
Order P2	-	3.34	1.13	
Error P3	7.99E-03	2.15E-02	9.24E-03	-0.1060
Order P3	-	-1.43	1.22	
Error P4	4.42E-02	2.08E-02	9.44E-03	0.0717
Order P4	-	1.08	1.14	
Error P5	2.95E-02	2.69E-03	1.20E-02	-0.1967
Order P5	-	3.46	-2.16	
Error P6	2.52E-02	1.09E-02	4.45E-03	0.1324
Order P6	-	1.21	1.29	
Error P7	0.00E+00	0.00E+00	0.00E+00	-0.9288
Order P7	-	-	-	

The exact solution for $r = \|x\|$ is then

$$u(x) = \begin{cases} \kappa_1, & \|x\| < R_1. \\ \kappa_{i-1} + \frac{\frac{1}{R_{i-1}} - \frac{1}{r}}{\frac{1}{R_{i-1}} - \frac{1}{R_i}} (\kappa_i - \kappa_{i-1}), & R_{i-1} \leq \|x\| < R_i \ (i = 2 \dots M). \\ (-1)^M \frac{1}{R_M}, & R_M < \|x\|. \end{cases}$$

Table C.5: The solution error for one multi-layered ball. The boundary condition is assigned the signed curvature. The multi-layered ball is centered at $(0.1, 0.2, -0.1)$ with radii 0.23, 0.47, 0.72, 0.95.

N	32	64	128	Distance
Error P1	8.84E-01	5.20E-02	6.42E-02	-0.1292
Order P1	-	4.09	-0.30	
Error P2	6.33E-01	2.34E-01	4.33E-02	0.1095
Order P2	-	1.44	2.43	
Error P3	9.96E-01	1.79E-01	1.06E-01	-0.1015
Order P3	-	2.48	0.76	
Error P4	1.26E+00	1.89E-01	1.02E-01	0.0816
Order P4	-	2.74	0.90	
Error P5	4.94E-03	4.87E-03	2.17E-04	-0.8640
Order P5	-	0.02	4.49	

Appendix D

Optimal Linear Combination of Double and Single Layer Potential for Neumann Helmholtz Problem

Define the operators $\mathcal{S}, \mathcal{D}, \mathcal{D}^*, \mathcal{T} : C^\infty(\Gamma) \rightarrow C(\mathbb{R}^2)$ as in (2.3):

$$\begin{aligned}(\mathcal{S}\alpha)(x) &:= \int_{\Gamma} \Phi(x,y) \alpha(y) dy(s). \\(\mathcal{D}\alpha)(x) &:= \int_{\Gamma} \frac{\partial \Phi}{\partial n_y}(x,y) \alpha(y) dy(s). \\(\mathcal{D}^*\alpha)(x) &:= \int_{\Gamma} \frac{\partial \Phi}{\partial n_x}(x,y) \alpha(y) dy(s). \\(\mathcal{T}\alpha)(x) &:= \frac{\partial}{\partial n_x} \int_{\Gamma} \frac{\partial \Phi}{\partial n_y}(x,y) \alpha(y) dy(s).\end{aligned}$$

Recall the boundary integral formulation using both single and double layer potential:

$$u = (\mathcal{D} - i\xi \mathcal{S})\alpha.$$

And the inversion formula for Neumann data on the boundary:

$$g = \frac{\partial u}{\partial n_x} = (\mathcal{S} - i\xi(\mathcal{D}^* - \frac{1}{2}\mathcal{S}))\alpha.$$

The choice of ξ affects the condition number for the inversion matrix. [Kress & Spassov (1983)] has shown that the optimal parameter for 2D is

$$\xi \approx \begin{cases} \left(\pi^2 + 4(\ln \frac{k}{2} + \gamma)^2\right)^{-\frac{1}{2}}, & \text{if } k \text{ is small } (k \leq 8). \\ 0.5k, & \text{if } k \text{ is large } (k > 8). \end{cases} \quad (\text{D.1})$$

where $\gamma \approx 0.5772\dots$ is the Euler's constant. For Helmholtz equation in \mathbb{R}^3 , they showed the optimal choice is

$$\xi \approx \begin{cases} \xi_0 \in [\frac{1}{2}, 1], & \text{if } k \text{ is small } (k \leq 8). \\ 0.5k, & \text{if } k \text{ is large } (k > 8). \end{cases} \quad (\text{D.2})$$

We use the above choices of ξ in the numerical experiments. However, we acknowledge that due to the off-interface regularization of the hypersingular integral, the condition number and its estimates may not be the same as the parametrized case on interface as analyzed in [Kress & Spassov (1983)].

References

- Adalsteinsson, D., & Sethian, J. 1995. A fast level set method for propagating interfaces. *Journal of Computational Physics*, **118**.
- Aimi, A., & Diligenti, M. 2002. Hypersingular kernel integration in 3D Galerkin boundary element method. *Journal of Computational and Applied Mathematics*, **138**.
- Ammari, H., Bossy, E., Jugnon, V., & Kang, H. 2010. Mathematical modeling in photoacoustic imaging of small absorbers. *SIAM Review*, **52**.
- Atkinson, K., & Chandler, G. 1990. Boundary integral equation methods for solving Laplace's equation with nonlinear boundary conditions: The smooth boundary case. *Mathematics of Computation*, **55**.
- Babuska, I. 1970. The finite element method for elliptic equations with discontinuous coefficients. *Computing*, **5**.
- Barles, G., & Da Lio, F. 2004. On the generalized Dirichlet problem for viscous Hamilton-Jacobi equations. *Journal de Mathematiques Pures et Appliquees*, **83**.
- Barnes, J., & Hut, P. 1986. A hierarchical $O(N \log N)$ force-calculation algorithm. *Nature*, **324**.
- Beale, J., & Strain, J. 2008. Locally corrected semi-Lagrangian methods for Stokes flow with moving elastic interfaces. *J. Comput. Phys.*, **227**.

- Bedrossian, J., von Brecht, J., Zhu, S., Sifakis, E., & Teran, J. 2010. A second order virtual node method for elliptic problems with interfaces and irregular domains. *Journal of Computational Physics*, **229**.
- Brakhage, H., & Werner, P. 1965. Über das Dirichletsche Aussenraumproblem für die Helmholtzsche Schwingungsgleichung. *Archiv der Mathematik*, **16**.
- Brundrit, G. 1965. A solution to the problem of scalar scattering from a smooth, bounded obstacle using integral equations. *The Quarterly Journal of Mechanics and Applied Mathematics*, **18**.
- Bruno, O., Elling, T., & Turc, C. 2012. Regularized integral equations and fast high-order solvers for sound-hard acoustic scattering problems. *International Journal for Numerical Methods in Engineering*, **91**.
- Buckmaster, J., & Ludford, G. 2008. *Theory of Laminar Flames*. Cambridge University Press.
- Burridge, R. 1976. *Some mathematical topics in seismology*.
- Burton, A. J., & Miller, G. F. 1971. The application of integral equation methods to the numerical solution of some exterior boundary-value problems. *Proceedings of the Royal Society of London. Series A, Mathematical and Physical Sciences*, **323**.
- Caffarelli, L., & Vázquez, J. 1995. A free-boundary problem for the heat equation arising in flame propagation. *Transactions of the American Mathematical Society*, **347**.
- Cahn, J., & Hilliard, J. 1959. Free energy of a nonuniform system III: Nucleation in a two-component incompressible fluid. *The Journal of Chemical Physics*, **31**.
- Canino, L., Ottusch, J., Stalzer, M., Visher, J., & Wandzura, S. 1998. Numerical solution of the Helmholtz equation in 2D and 3D using a high-order Nystrom discretization. *Journal of Computational Physics*, **146**.

- Chen, S., Merriman, B., Osher, S., & Smereka, P. 1997. A simple level set method for solving Stefan problems. *Journal of Computational Physics*, **135**.
- Chen, Y., Giga, Y., & Goto, S. 1991. Uniqueness and existence of viscosity solutions of generalized mean curvature flow equations. *J. Differential Geom.*, **33**.
- Cheng, L., & Tsai, R. 2008. Redistancing by flow of time dependent Eikonal equation. *Journal of Computational Physics*, **227**.
- Chopp, D. 2001. Some improvements of the fast marching method. *SIAM Journal on Scientific Computing*, **23**.
- Colton, D., & Kress, R. 2013. *Integral Equation Methods in Scattering Theory*. Philadelphia, PA: Society for Industrial and Applied Mathematics.
- Copley, L. 1968. Fundamental results concerning integral representations in acoustic radiation. *The Journal of the Acoustical Society of America*, **44**.
- Crandall, M., Ishii, H., & Lions, P. 1992. *User's Guide to Viscosity Solutions of Second Order Partial Differential Equations*.
- Dervieux, A., & Thomasset, F. 1980. *A finite element method for the simulation of a Rayleigh-Taylor instability*.
- Dervieux, A., & Thomasset, F. 1981. Multifluid incompressible flows by a finite element method. *In: Seventh International Conference on Numerical Methods in Fluid Dynamics*, vol. 141.
- Di Stefano, L., & Bulgarelli, A. 1999. A simple and efficient connected components labeling algorithm. *In: Proceedings of the 10th International Conference on Image Analysis and Processing*.

- Dillencourt, M., Samet, H., & Tamminen, M. 1992. A general approach to connected-component labeling for arbitrary image representations. *J. ACM*, **39**.
- Dolbow, J., & Harari, I. 2009. An efficient finite element method for embedded interface problems. *International journal for numerical methods in engineering*, **78**.
- Ehrenpreis, L. 1960. Solution of some problems of division Part IV. invertible and elliptic operators. *American Journal of Mathematics*, **82**.
- Engquist, B., & Ying, L. 2007. Fast directional multilevel algorithms for oscillatory kernels. *SIAM Journal on Scientific Computing*, **29**.
- Engquist, B., Tornberg, A., & Tsai, R. 2005. Discretization of Dirac delta functions in level set methods. *Journal of Computational Physics*, **207**.
- Escher, J., & Simonett, G. 1998. A center manifold analysis for the Mullins-Sekerka model. *Journal of Differential Equations*, **143**.
- Evans, L. C., & Spruck, J. 1991. Motion of level sets by mean curvature. *J. Differential Geom.*, **33**.
- Flemings, M. 2006. *Solidification Processing*.
- Fornaro, O., Palacio, H., & Biloni, H. 2006. Segregation substructures in dilute Al-Cu alloys directionally solidified. *Materials Science and Engineering: A*, **417**.
- Frangi, A. 1998. Regularization of boundary element formulations by the derivative transfer method. *Singular Integrals in the Boundary Element Method*, V. Sladek and J. Sladek, eds., *Advances in Boundary Elements, Computational Mechanics Publishers*.
- Gibou, F., & Fedkiw, R. 2004. A fourth order accurate discretization for the Laplace and heat equations on arbitrary domains, with applications to the Stefan problem. *J. Comput. Phys*, **202**.

- Golding, I., Kozlovsky, Y., Cohen, I., & Ben-Jacob, E. 1998. *Studies of bacterial branching growth using reaction-diffusion models for colonial development.*
- Gottlieb, S., & Shu, C. 1998. Total variation diminishing Runge-Kutta schemes. *Math. Comp.*, **67**.
- Greenbaum, A., Greengard, L., & McFadden, G. 1993. Laplace's equation and the Dirichlet-Neumann map in multiply connected domains. *Journal of Computational Physics*, **105**.
- Greengard, L., & Rokhlin, V. 1987. A fast algorithm for particle simulations. *J. Comput. Phys.*, **73**.
- Greenleaf, A., Kurylev, Y., Lassas, M., & Uhlmann, G. 2008. *Invisibility and inverse problems.*
- Gurtin, M. 1986. On the two-phase Stefan problem with interfacial energy and entropy. *Archive for Rational Mechanics and Analysis*, **96**.
- Hackbusch, W., & Sauter, S. 1993. On the efficient use of the Galerkin-method to solve Fredholm integral equations. *Applications of Mathematics*, **38**.
- Hansbo, A., & Hansbo, P. 2004. A finite element method for the simulation of strong and weak discontinuities in solid mechanics. *Computer Methods in Applied Mechanics and Engineering*, **193**.
- Harari, I., & Hughes, T. 1991. Finite element methods for the helmholtz equation in an exterior domain: Model problems. *Computer Methods in Applied Mechanics and Engineering*, **87**.
- Helmsen, J., Puckett, E., Colella, P., & Dorr, M. 1996. Two new methods for simulating photolithography development.
- Helsing, J. 2009. Integral equation methods for elliptic problems with boundary conditions of mixed type. *Journal of Computational Physics*, **228**.

- Jiang, G., & Peng, D. 1997. Weighted ENO schemes for Hamilton-Jacobi equations. *SIAM J. Sci. Comput.*, **21**.
- Johansen, H., & Colella, P. 1998. A Cartesian grid embedded boundary method for Poisson's equation on irregular domains. *Journal of Computational Physics*, **147**.
- Karali, G., & Kevrekidis, P. 2009. Bubble interactions for the Mullins-Sekerka problem: some case examples. *Math. Comput. Simul.*, **80**.
- Kleinman, R. E., & Roach, G. F. 1974. Boundary integral equations for the three-dimensional Helmholtz equation. *SIAM Review*, **16**.
- Klockner, A., Barnett, A., Greengard, L., & O'Neil, M. 2013. Quadrature by expansion: A new method for the evaluation of layer potentials. *Journal of Computational Physics*, **252**.
- Kohn, R., Shen, H., Vogelius, M., & Weinstein, M. 2008. Cloaking via change of variables in electric impedance tomography. *Inverse Problems*, **24**.
- Kress, R. 1991. Boundary integral equations in time-harmonic acoustic scattering. *Mathematical and Computer Modelling*, **15**.
- Kress, R. 1995. On the numerical solution of a hypersingular integral equation in scattering theory. *Journal of Computational and Applied Mathematics*, **61**.
- Kress, R. 2012. *Linear Integral Equations*. Applied Mathematical Sciences. Springer London, Limited.
- Kress, R., & Spassov, W.T. 1983. On the condition number of boundary integral operators for the exterior Dirichlet problem for the Helmholtz equation. *Numerische Mathematik*, **42**.
- Kublik, C., & Tsai, R. 2015. Integration over curves and surfaces defined by the closest point mapping. *eprint arXiv:1504.05478*.

- Kublik, C., Tanushev, N., & Tsai, R. 2013. An implicit interface boundary integral method for Poisson's equation on arbitrary domains. *Journal of Computational Physics*, **247**.
- Kuchment, P., & Kunyansky, L. 2008. Mathematics of thermoacoustic tomography. *European Journal Applied Mathematics*.
- Kutt, H. 1975. The numerical evaluation of principal value integrals by finite-part integration. *Numerische Mathematik*, **24**(3), 205–210.
- Langer, J. 1980. Instabilities and pattern formation in crystal growth. *Rev. Mod. Phys.*, **52**.
- Leveque, R., & Li, Z. 1994. The immersed interface method for elliptic equations with discontinuous coefficients and singular sources. *SIAM J. Num. Anal.*
- Li, Z., & Ito, K. 2006. *The immersed interface method: Numerical solutions of PDEs involving interfaces and irregular domains*. Frontiers in Applied Mathematics. Society for Industrial and Applied Mathematics.
- Liu, Y., & Rizzo, F. 1992. A weakly singular form of the hypersingular boundary integral equation applied to 3-D acoustic wave problems. *Computer Methods in Applied Mechanics and Engineering*, **96**.
- Malgrange, B. 1956. Existence et approximation des solutions des equations aux derivees partielles et des equations de convolution. *Annales de l'institut Fourier*, **6**.
- Malladi, R., Sethian, J., & Vemuri, B. 1995. Shape modeling with front propagation: A level set approach. *IEEE Transactions on Pattern Analysis and Machine Intelligence*, **17**.
- Matsushita, M., & Fujikawa, H. 1990. Diffusion-limited growth in bacterial colony formation. *Physica A: Statistical Mechanics and its Applications*, **168**.
- Mayer, U. 1993. One-sided Mullins-Sekerka flow does not preserve convexity. *J. Differential Equations*.

- Mikhlin, S., Sneddon, N., & Ulam, S. 1964. *Integral Equations*. International Series Of Monographs On Pure And Applied Mathematics. Pergamon Press.
- Min, C., & Gibou, F. 2007. A second order accurate level set method on non-graded adaptive cartesian grids. *Journal of Computational Physics*, **225**.
- Mullins, W., & Sekerka, R. 1963. Morphological stability of a particle growing by diffusion or heat flow. *Journal of Applied Physics*, **34**.
- Osher, S., & Fedkiw, R. 2000. *Level set methods and dynamic implicit surfaces*. Springer.
- Osher, S., & Sethian, J. 1988. Fronts propagating with curvature-dependent speed: algorithms based on Hamilton-Jacobi formulations. *Journal of computational physics*, **79**.
- Paget, D. 1981. The numerical evaluation of Hadamard finite-part integrals. *Numerische Mathematik*, **36**.
- Panich, O.I. 1965. On the question of solvability of the exterior boundary-value problems for the wave equation and Maxwell's equations. *Russian Math. Surv.*
- Pego, R. 1989. Front migration in the nonlinear Cahn-Hilliard equation. *Proceedings of the Royal Society of London. Series A, Mathematical and Physical Sciences*, **422**.
- Peng, D., Merriman, B., Osher, S., Zhao, H., & Kang, M. 1999. A PDE-based fast local level set method. *Journal of Computational Physics*, **155**.
- Reutskiy, S. 2006. The method of fundamental solutions for Helmholtz eigenvalue problems in simply and multiply connected domains. *Engineering Analysis with Boundary Elements*, **30**. Non-Traditional Boundary Integral Formulations, Part {II}.
- Rokhlin, V. 1993. Diagonal forms of translation operators for the Helmholtz equation in three dimensions. *Applied and Computational Harmonic Analysis*, **1**.

- Rosenfeld, A., & Pfaltz, J. 1966. Sequential operations in digital picture processing. *J. ACM*, **13**.
- Russo, G., & Smereka, P. 2000. A remark on computing distance functions. *Journal of Computational Physics*, **163**.
- S. Osher, C. Shu. 1991. High-order essentially nonoscillatory schemes for Hamilton-Jacobi equations. *SIAM Journal on Numerical Analysis*, **28**.
- Saad, Y., & Schultz, M. 1986. GMRES: A generalized minimal residual algorithm for solving nonsymmetric linear systems. *SIAM Journal on Scientific and Statistical Computing*, **7**.
- Samet, H., & Tamminen, M. 1988. Efficient component labeling of images of arbitrary dimension represented by linear bintrees. *IEEE Trans. Pattern Anal. Mach. Intell.*, **10**.
- Samid-Merzel, N., Lipson, S., & Tannhauser, D. 1998. Pattern formation in drying water films. *Physica A: Statistical Mechanics and its Applications*, **257**.
- Schneider, S. 2003. *Efficient usage of the boundary element method for solving the time harmonic Helmholtz equation in three dimensions*.
- Sethian, J. 1996. *Fast-marching level-set methods for three-dimensional photolithography development*.
- Shearer, P. 2003. *Introduction to Seismology*. Vol. 7.
- Singer, I., & Turkel, E. 1998. High-order finite difference methods for the Helmholtz equation. *Computer Methods in Applied Mechanics and Engineering*, **163**.
- Smereka, P. 2006. The numerical approximation of a delta function with application to level set methods. *Journal of Computational Physics*, **211**.
- Smirnov, V. 1964. *In: A Course of Higher Mathematics*. International Series of Monographs on Pure and Applied Mathematics, vol. 61.

- Strain, J. 1999. Fast tree-based redistancing for level set computations. *Journal of Computational Physics*, **152**.
- Sussman, M., Smereka, P., & Osher, S. 1994. A level set approach for computing solutions to incompressible two-phase flow. *Journal of Computational Physics*, **114**.
- Tornberg, A., & Engquist, B. 2004. Numerical approximations of singular source terms in differential equations. *Journal of Computational Physics*, **200**.
- Towers, J. 2007. Two methods for discretizing a delta function supported on a level set. *Journal of Computational Physics*, **220**.
- Tsai, R., & Osher, S. 2003. Level set methods and their applications in image science. *Comm. Math Sci*, **1**.
- Tsai, R., & Osher, S. 2005. Total variation and level set methods in image science. *Acta Numerica*, **14**.
- Tsai, R., Cheng, L., Osher, S., & Zhao, H. 2003. Fast sweeping algorithms for a class of Hamilton-Jacobi equations. *SIAM Journal on Numerical Analysis*, **41**.
- Tsitsiklis, J. 1995. Efficient algorithms for globally optimal trajectories. *IEEE Transactions on Automatic Control*, **40**.
- W. Kurz, D. Fisher. 1986. Fundamentals of solidification. *Crystal Research and Technology*, **21**.
- Wagner, P. 2009. A new constructive proof of the Malgrange-Ehrenpreis theorem. *The American Mathematical Monthly*, **116**.
- Ying, L., Biros, G., & Zorin, D. 2004. A kernel-independent adaptive fast multipole algorithm in two and three dimensions. *J. Comput. Phys.*, **196**.

Zahedi, S., & Tornberg, A. 2010. Delta function approximations in level set methods by distance function extension. *Journal of Computational Physics*, **229**.

Zhao, H. 2004. *A fast sweeping method for Eikonal equations*.

Zhao, H., Chan, T., Merriman, B., & Osher, S. 1996. A variational level set approach to multiphase motion. *Journal of Computational Physics*, **127**.

Zhu, J., Chen, X., & Hou, T. 1996. An efficient boundary integral method for the Mullins-Sekerka problem. *Journal of Computational Physics*, **127**.